ABSTRACT

Title of Dissertation: III-V OPTOELECTRONIC DEVICES: ROOM TEMPERATURE CW OPERATION OF INTERBAND CASCADE LASER & HIGH EFFICIENCY P-SIDE DOWN InGaN/GaN SOLAR CELL

Geunmin Ryu,
Doctor of Philosophy, 2011

Dissertation Directed By: Professor Mario Dagenais,
Electrical and Computer Engineering Department

During the past two decades, the field of III-V optoelectronic devices has gained widespread interest as a result of advances in the performance and reliability of epitaxial structures. In principle, III-V materials can provide sources, detectors and optoelectronic components over wavelengths from UV to IR. During my Ph.D study, I have focused on two III-V optoelectronic devices: Mid-IR interband cascade lasers and group III-Nitride solar cells. In the first part of this dissertation, we will discuss development of a room temperature CW operation interband cascade laser and in the second part, we will discuss the concept of high efficiency III-N solar cells.

Part I

Lasers that emit in the mid-IR (3~5um) spectral region can be used in many civilian and military applications such as chemical sensing, free space optical

communication and IR countermeasures. There are three types of lasers that can cover the Mid-IR region. First, conventional type-I quantum well (QW) lasers on GaSb substrates, second, inter-subband quantum cascade lasers (QCLs) on InP substrates and finally interband cascade laser with type-II alignment of the conduction and valence bands on GaSb substrates. Gallium Antimonide based type II interband cascade lasers (ICLs) cover the 3~4 um wavelength range, and it is the most natural match to the mid-IR.

For most applications, it is required that the laser operates in continuous wave (CW) mode either at room temperature or at temperatures accessible to thermoelectric coolers. Recently, we have been able to operate interband cascade lasers in CW mode at room temperature with 62mW of output power, internal loss of 4.8cm^{-1}, 170mW/A slope efficiency, and a threshold current density as low as 300 A/cm^2 which are a significant milestone toward many applications. In the first part of this thesis, we are going to talk about the fundamental principles of operation of the ICLs and their applications. Secondly, we will present the development of a fabrication process. Third, we will discuss the performance characteristics of ICLs. Lasers were characterized by doing series of length dependent pulsed/CW measurements to obtain critical parameters at low temperature and at room temperature; such as wall plug efficiency, threshold current density, internal loss, and thermal impedance. For low temperature CW measurement, a specially designed vacuum chamber was used to prevent water condensation. Finally, we will present ICL optimization processes. For laser optimization, we re-designed the device structure, in particular the lower cladding region, the injection region, and the active region thickness, to achieve a

higher confinement factor and lower loss, thus increasing the operating temperature and the output power.

Part II

Since the 1950s, silicon solar cells have been intensively studied and developed. Solar cell technology has greatly benefited from the maturity of silicon technology developed originally for the IC industry. This has led to the development of high quality single crystal silicon wafers with low dislocation densities. However, because of the poor spectral overlap between the absorption of silicon cells and the spectrum of solar light, silicon solar cells cannot fundamentally produce high efficiency solar cells. In order to achieve high efficiency solar cells, researchers have investigated many alternatives including tandem cells, GaAs, and III-Nitride materials. In the second part of this thesis, we will talk about the development of high efficiency III-Nitride solar cells using novel p-side InGaN/GaN materials, including device background, new solar cell design, fabrication process development, and preliminary device characterizations.

III-V OPTOELECTRONIC DEVICES:

ROOM TEMPERATURE CW OPERATION OF INTERBAND CASCADE LASER & HIGH EFFICIENCY P-SIDE DOWN InGaN/GaN SOLAR CELL

By

Geunmin Ryu

Dissertation submitted to the Faculty of the Graduate School of the
University of Maryland, College Park, in partial fulfillment
of the requirements for the degree of
Doctor of Philosophy
2011

Advisory Committee:
Professor Mario Dagenais, Chair
Professor Christopher Davis
Professor Martin Peckerar
Professor Thomas E. Murphy
Professor Lourdes Salamanca-Riba, Deans Representative
Dr. John Bruno, Maxion Technology

Dedication

To my loving wife, son
and parents

Acknowledgements

First, I would like to thank my advisor, Professor Mario Dagenais for giving me an opportunity to work in the field of photonics. When I graduated from Ohio state university, I had very limited knowledge of photonics. Without his commitment, I was not able to be here today. I also appreciate his patience. Sometimes we had disagreements and arguments of experimental results and he was always calm and tried to explain his opinion. Professor Dagenais was always there for me and I am deeply grateful.

I would also like to thank the other committee members: Professor Davis, Professor Peckerar, Professor Murphy, Professor Salamanca-Riba, and Dr. Bruno. Especially, I like to thank Dr. Bruno from Maxion Technologies for his valuable time and providing us laser materials.

Next, I like to thank my best friend and colleague Dr. Athanasios Chryssis. During my Ph.D study, I had his unlimited support. Without his support, my Ph.D life would have been very different. I am very happy to have him as a friend and colleague.

Also as a member of the laboratory for green nanophotonics, optoelectronis and nanosensing, I would like to recognize my colleagues: Jeyran Amirloo, Tian Li, Sunil Mittal, and other lab mates. I am grateful for their help and support.

Throughout my research, I was very lucky to have many talented individuals to discuss and collaborate on my projects: Kwangsik Choi, Filiz Yesilkoy, and Ehren Hwang. They were always supportive and never hesitated to share their idea. Also I

have had a privilege to work with Fablab staff members: Jim O'Connor, Tom Loughran, Jon Hummel, and John Abrahams. I really appreciate their time and support in the cleanroom.

During 9 years of my study in U.S, my parents have been unconditionally supportive. They always encouraged me to go forward and be there for me. Without their love, I won't be here today.

Finally, I would like to thank my lovely wife Inyeong. We met at the beginning of my Ph.D study and now we are finishing our degrees together plus our newborn son Aiden. These days, I cannot be happier to be a father and husband. She is the most important person in my life and I am very lucky to have her with me….

Sincerely

Geunmin Ryu

Table of Contents

List of Tables

List of Figures

Part 1:Room temperature CW operation of interband cascade laser

Chapter 1: Introduction

Since the 1990s civilian and military applications including chemical sensing, free-space optical communication, IR countermeasures, and IR ladars, have driven the need for compact and affordable mid-IR sources. For the mid-IR wavelength region, three different laser development efforts are under study. First, conventional type-I quantum well (QW) lasers on GaSb substrates [1-5]; second, inter-subband quantum cascade lasers (QCLs) on InP substrates [6-10]; and finally interband cascade laser with type-II alignment of the conduction and valence bands on GaSb substrates are all being investigated [11-15].

Conventional QW lasers are well developed in the 2-3um wavelength region and researchers are working on extending the wavelength range beyond 3um without suffering from non-radiative Auger recombination or the lack of valence band offset [4,5]. Indium Phosphide based intersubband quantum cascade lasers (QCLs) cover the 4~12 um wavelength range and QCLs can generate multiwatt CW output power at room temperature below 5um [6,7] and researchers are working on extending the wavelength range below 3.7um[8] despite the lack of the conduction band offset of the barrier (InAlAs) and the well material (AlInGaAs). Recently, researchers from Northwestern University have achieved 21% wall plug efficiency (WPE) and 5.1W of CW room temperature output power at 4.9um. Gallium Antimonide based type II interband cascade lasers (ICLs) cover the 3~4 um wavelength range, and it is the most natural match to the mid-IR. Type-II ICLs can now emit more than 50mW of CW output power per facet without any coating [16]. Also, recently researchers

achieved 13.5% CW wall plug efficiency at room temperature and ICL can now be operated CW above 100°C. Detailed description of all three different laser types will be discussed in the next sections.

For most applications, it is required that the laser operates in CW mode either at room temperature or at temperatures accessible to thermoelectric coolers. In 2008, interband cascade lasers have been shown to operate continuously at room temperature, which is a significant milestone towards the widespread application of this technology.

Using spectroscopy, the mid -IR lasers can be used for chemical sensing since the mid-IR range permits targeting of strong coupling to the vibrational modes of molecules like CH_4, N_2O, CO_2, CO, H_2O, NH_3, C_2H_4, SO_2, C_2H_5OH and C_2HO. Chemical sensing applications can be used both in the medical field and in industry. By detecting the CO/CO_2 ratio, we can monitor neonatal jaundice, asthma, and lung capacity. Also, NH_3 in someone's breath has been linked to serious kidney diseases [17-19]. Methane (CH_4) is the primary component of natural gas as well as a potent greenhouse gas, and CO/CO_2 ratios can be used as a measure of combustion efficiency of furnaces or reactors [20-22].

Mid-IR lasers can also be used in free space communications. The 3~4 um infrared atmospheric window allows low absorption in mid-IR as shown in Figure 1-1.

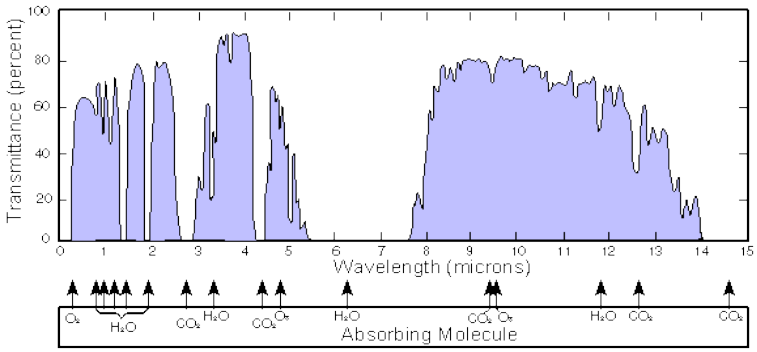

Figure 1-1. Transmittance spectrum of atmosphere vs. wavelength.

Another important applications of these lasers is in IR countermeasures. Since flares are not foolproof and pose risk of fire on the ground, high power mid-IR lasers can jam the guidance systems of heat seeking missiles.

Our goal was to study and improve the IC laser structure and achieve continuous wave operation at room temperature with high power. In order to achieve our goal, we have conducted detailed analysis of the interband cascade laser system.

It all started with improving the device fabrication processes. At the beginning we developed the wet etching processing using phosphoric acid based etchant but now we use the dry etching processing with flash wet etching with phosphoric acid based etchant. The dry etching processing improves device performance consistency and thermal behavior. After the process development, we spent most of our time on improving device performances. This includes thermal analysis, optimizing the lower and the upper cladding thickness to reduce loss, introducing SCH region to achieve higher confinement factor, reducing the number of cascades, adjusting doping concentration in the active region, and reducing the injection region thickness. We also have developed high reflectivity and anti-reflectivity coatings. From these developments and improvements, we have achieved better understanding of what is

required for operating an IC laser at room temperature and now we have interband cascade lasers that can be operated in continuous wave mode at room temperature with 62mW output power with low internal loss of 4.8 cm^{-1}. We are now in the process of improving the output power.

In Chapter 2, we present growth and operation principles of the ICLs as well as competing technologies, QCLs and QW lasers. Also the fundamental device theory is discussed. In Chapter 3, we present the experimental procedures including mask design, device fabrication, and laser test set-up. In Chapter 4, we discuss thermal analysis including thermal simulation of epi-down/epi-up mount and thermal impedance measurement. High reflectivity and anti-reflectivity coating design and experimental result are presented in Chapter 5. In Chapter 6, interband cascade laser performance improvements and high power room temperature CW operation are presented. In Chapter 7, we conclude with summarizing our work and proposing future work. Detailed interband cascade laser fabrication steps, thermal simulation code, and a list of our publication are presented in the Appendix.

Chapter 2: Interband Cascade Lasers

2.1 Laser

The word “laser” is an acronym for Light Amplification by Stimulated Emission of Radiation. A device needs to have both stimulated emission and positive optical feedback for optical amplification in order to be called a laser. The first working laser was demonstrated in 1960 by Maiman using a ruby crystal optically pumped by a flash-light. Since 1960, many researchers have studied and developed many different types of lasers. We can categorize the types of lasers by the active medium such as solid, gas, or liquid.

Solid lasers can be subdivided into two categories, solid-state and semiconductor lasers. Solid-state lasers rely on optical transitions between atomic states introduced by intentionally doping the solid-state material and most of time they are optically pumped since they are made of insulating material. Examples of solid-state lasers are ruby, Nd:YAG, and Ti:Sapphire lasers. Semiconductor lasers rely on optical transitions between energy bands such as the conduction or valence band. A semiconductor laser can be pumped either optically or electrically. The most common semiconductor laser structure is a simple p-n junction diode laser that can generate photons by an optical transition between the conduction band and the valence band. A natural evolution of the p-n juction is the double hetrostructure (DH). To form a DH structure, a narrow bandgap material is sandwiched between two wide bandgap materials as shown in Figure 2-1. The active region where the optical

transitions occur is in the narrow bandgap region. The wide bandgap region works as the cladding region where the index of refraction is lower than the active region. Under bias, electrons and holes are injected correspondingly from the n and p side into the active region and trapped in the active region due to the band offset. Then carriers recombine with each other emitting certain a wavelength of light that corresponds to the bandgap of the active region. In order to have flexibility of wavelength tailoring, a quantum well structure is introduced as shown in Figure 2-1. The quantized energy levels, which are determined by the quantum well thickness, allow us to tailor the emission wavelength. To improve the mode confinement, separate confinement heterostructures (SCH) are also introduced on both sides of the quantum well. To increase the gain of the quantum well lasers, the multiple quantum wells are created as shown in Figure 2-1. Liquid lasers are also called dye lasers since they are typically based on organic dyes dissolved in a solvent. Examples of liquid lasers are Rhodamine 6G, and Tetrazene. Gas lasers rely on the energy of the gas mixtures that are excited by electrical discharges. Examples of gas lasers are HeNe, Excimer (KrF), and CO_2 lasers.

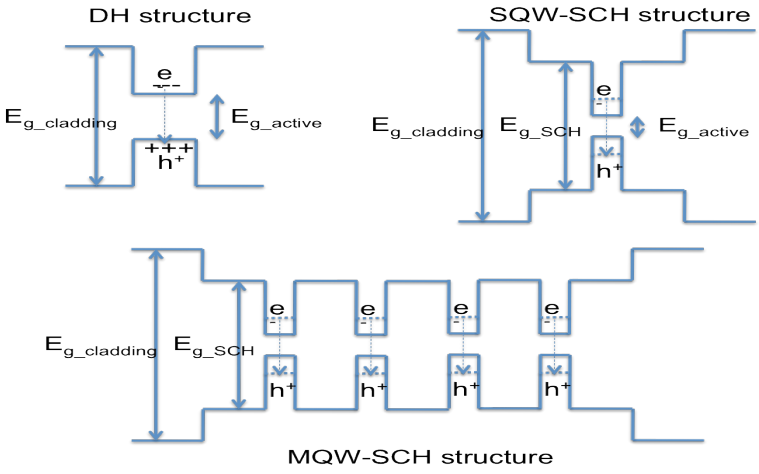

Figure 2-1 Laser structures

2.2 Competing Technologies

2.2.1 Quantum Cascade Lasers

Quantum cascade lasers (QCLs) are based on intersubband transitions. QCLs were first proposed by Kasarinov and Suris [23]. The term cascade laser signifies that the output of one stage serves as the input to the next stage. Typically, QCLs have about 30~50 stages and QCLs operate within the 4~12um range. It is very important to design the electron flow through minibands to achieve a buildup of electrons in the upper laser subband and fast extraction from lower laser subbands. The QCLs are unipolar devices, meaning that all electronic processes only occur in the conduction band. Since QCLs are unipolar devices, unlike ICLs, they do not suffer from a variety of non-radiative recombination process such as interband Auger recombination. The overall QCL structure has a lot of similarities to the ICL structure. It has the injection region and the active region within a stage. Like ICLs, the injection region is a chirped resonant tunneling structure. The QCL injection region is composed of InAlAs and InGaAs which are lattice matched to the InP substrate.

The active region is composed of multiple quantum wells, usually four quantum wells. The first quantum well, neighboring the injection region is very narrow. That enhances the injection efficiency into the upper lasing level by increasing locally the magnitude of the upper state wavefunction overlap with the wavefunctions of the injected modes. Electrons tunneling from the injection region have a lifetime of 4.3ps before they can non-radiatively relax to the lower energy states through fast phonon scattering [24]. In order to have population inversion,

transitions need to be faster than the injected electron lifetime, therefore researchers introduced a double phonon resonance [25]. The three remaining quantum wells of the active region are designed so that the energy states are separated by one longitudinal optical phonon energy. For three quantum wells, we have the double phonon resonance as shown in Figure 2-2.

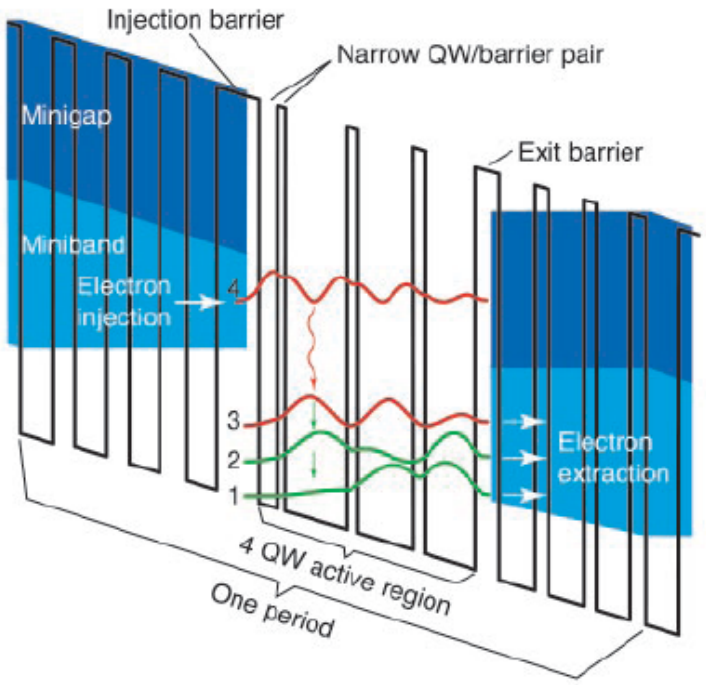

Figure 2-2 Illustration of two emitter stages of the quantum cascade laser [26]

Due to the fast phonon scattering process leading to high-dissipated power, QCLs are inherently very inefficient. However, there has been tremendous investment and progress in QCL development and recently, researchers from Northwestern University have achieved 5.1W of CW output power and 27% wall plug efficiency with 4.8um wavelength quantum cascade laser. Today, QCLs can operate in continuous mode at room temperature down to 3.6um.

2.2.2 Diode Lasers

Conventional type-I diode lasers also can emit in the mid-IR spectral region. Up to a wavelength of 3um, InGaAsSb layers are used for the quantum well (QW) region and AlGaAsSb layers are used for the barrier/cladding region. Using these structures, type-I diode lasers can emit watt class continuous wave output power at room temperature between 2.3um to 2.8um and near 3um they can produce about 200mW CW output power [27-33]. However, in spite of large difference between the band gaps of AlGaAsSb and InGaAsSb alloys in type-I QW lasers, the holes are poorly confined due to the lack of the valence band offset while the electrons are confined well within the QW region. In order to increase the emitting wavelength beyond 3um, researchers have developed heavily compressive strained QWs using low arsenic contents. [1,34,35]. By introducing the compressive strain in active QWs, they could improve the laser differential gain through the reduction of the hole density of states [35]. The other approach was to use quinary AlGaInAsSb alloys as a barrier and waveguide core material. Recently, researchers from University of New York at Stony Brook have demonstrated a continuous wave, room temperature operation of type-I quantum well diode laser at 3.44um [5].

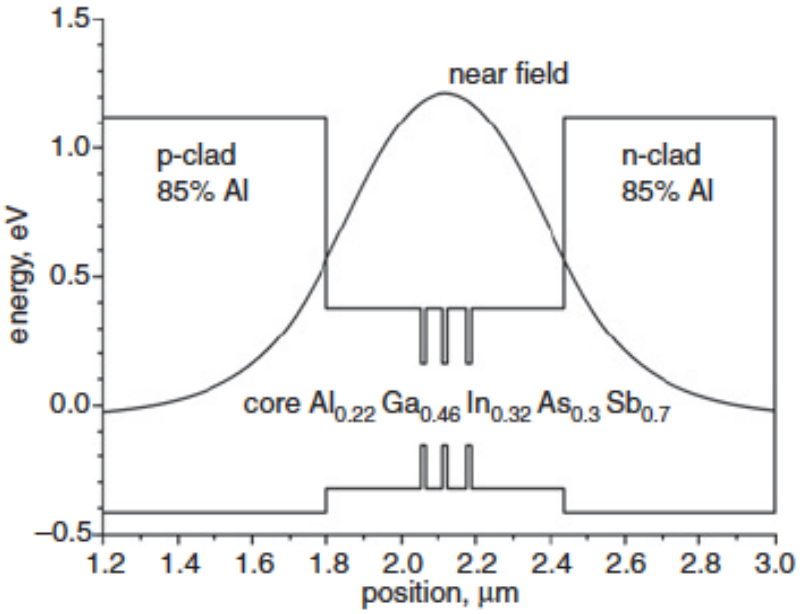

Figure 2-3 Band diagram of quinary barrier structure diode laser with near field distribution [5].

Figure 2-3 shows the band diagram of a quinary barrier structure laser with near field distribution. This multimode laser generates 29mW of output power at 17˚C [5]. For pulsed mode operation, GaSb based type-I lasers with quinary barriers can operate up to 3.6um at room temperature [36]. Despite the recent improvements, it can only generate low CW output power above 3.2um due to non-radiative Auger recombination and free carrier absorption. Also, it is very hard to grow structures with five different materials.

For wavelengths between 3~4um, the best way to overcome problems for quantum cascade & conventional diode laser is to use the InAs/GaSb based interband cascade lasers. Also, ICLs require less cooling and power than QCLs since ICLs have a lower threshold current density and turn on voltage.

2.3 ICL Fundamentals

The concept of interband cascade lasers was introduced by Yang in 1995. Since 3~5um is a very important spectral region for many applications, many groups are working on the development of ICL.

In this section, we will talk about the fundamentals of interband cascade lasers, the material selection of the active region, details of the interband laser structure, laser growth, strain and operation procedures of the ICLs.

2.3.1 Interband cascade laser material

When we design a laser, there are three main parameters that we have to consider: wavelength, lattice matching, and band offset. Wavelength can be calculated easily by the following simple equation $\lambda = \frac{hc}{E} = \frac{1.24}{E}$ where E is the energy band gap. Here wavelength has units of um, and energy has units of eV. In order to achieve a wavelength within 3~4um, the electron transition energy needs to be between two energy levels separated by 0.41~0.31eV. A interband cascade laser is composed of hundreds of epitaxial layers. These layers can create stress on the film resulting in an increase of the dislocation density that can increase the non-radiative recombination rate. The maximum stress without creating a large number of dislocations is about 5%. One way to reduce the stress is to match the lattice constant to the GaSb substrate.

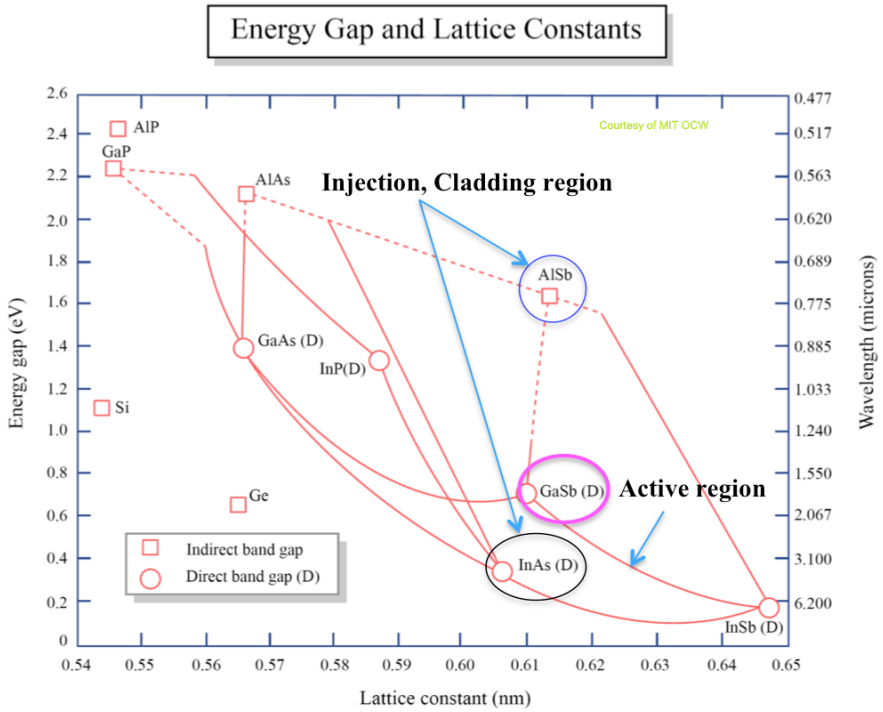

Figure 2-4 Lattice constant and band gap of semiconductor materials [37]

For ICL, AlSb and InAs are used in the cladding region and injection regions. As we can see from Figure 2-4, AlSb has a slightly larger and InAs has a slightly smaller lattice constant than a GaSb substrate material. By alternating AlSb and InAs, we can achieve a lattice mismatching compensation and make the averaged lattice good match to the GaSb substrate. For the active region, InAs and GaInSb are used so there will be compressive stress in the active region. The effect of compressive stress on the electron transition will be discussed in a later section.

Another reason why AlSb and InAs are used in the injection region is the band offset. Band offset can be either the valence band or the conduction band offset. Figure 2-5 shows the conduction and valence band offset.

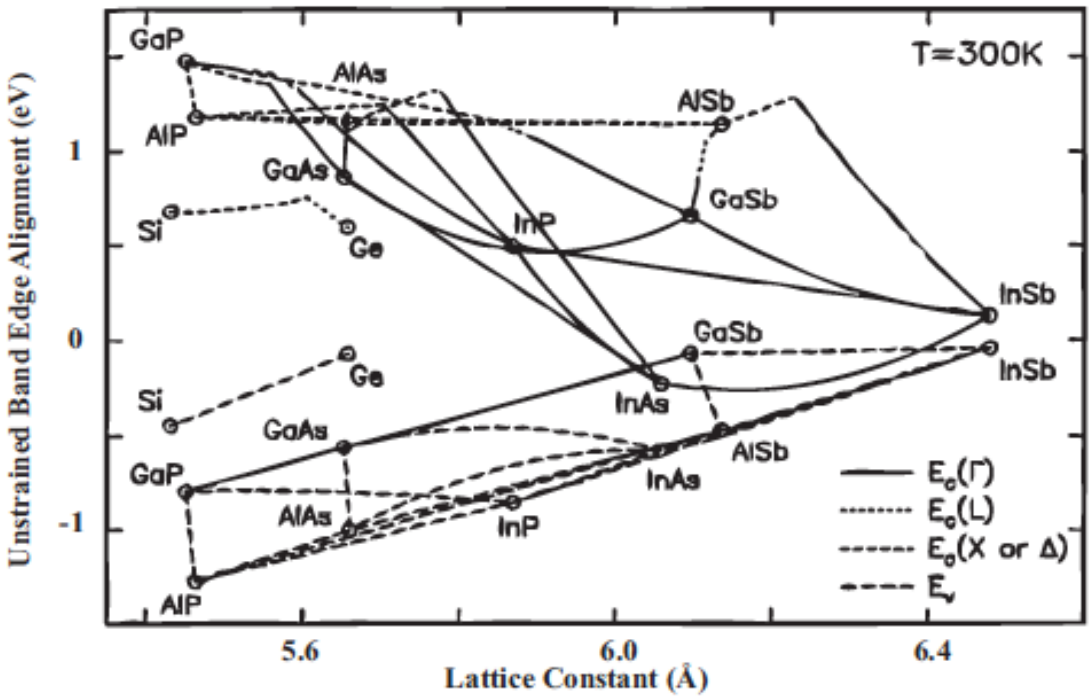

Figure 2-5 Conduction and valence band offset, alignment to gold [38]

The important facts are that the InAs conduction band edge is below the GaSb valence band edge and that AlSb has a very large conduction band offset compared to InAs. These two properties allow the feasibility of type II alignment. Also, the negative InAs alignment to Au allows the formation of an Ohmic contact instead of a Schottky barrier. This makes InAs a great material for the cap layer. The large conduction band offset of the Antimonide alloys are also the reason why short wavelength QCLs are Sb based.

2.3.2 Interband cascade laser structure and growth

A single stage of a biased, double quantum well type II interband cascade laser is shown in Figure 2-6. The entire ICL structure is composed of many such alternating active/injection stages that are sandwiched between two separate

confinement hetrostructures and optical cladding layers. The active region is separated by the injection region which serves both as a carrier collector for the preceding active region and an emitter for the next active region. Under forward bias, electrons are injected from the previous emitter into the E_e electron level. Since the electrons at E_e level are blocked from directly tunneling out through the GaInSb, AlSb, and GaSb layers, they tend to make a spatially diagonal transition to the E_h hole state in the valence band quantum wells (type II) resulting in the emission of photons. Electrons in the E_h state cross the thin InAs and AlSb layers into the neighboring GaInSb and GaSb layers. They then tunnel and scatter into the conduction band of the next injection region. The strong spatial interband coupling in type II quantum wells facilitates this tunneling.

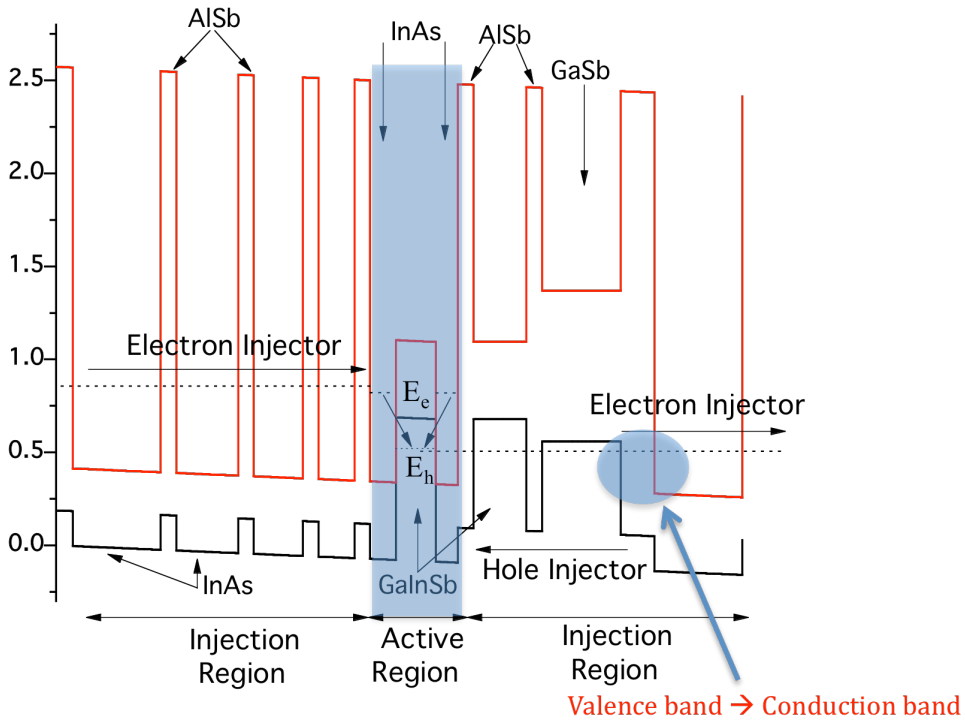

Figure 2-6 Type II interband cascade laser structure (shown a single stage)

The injection structure is designed so that, at the operating electric field, the QW states in adjacent InAs QWs are strongly coupled, forming a conduction miniband throughout the entire injection region. The design is intended to promote smooth transport of the electrons from each active region to the following active region where the electrons make their interband transition. This cascading leads to sequential photon emission with quantum efficiency exceeding the conventional limit of unity [39-41].

The lasing wavelength is determined by the energy separation between E_e and E_h, which can be tailored over a wide spectral range by adjusting the InAs and GaInSb layer thicknesses. Each layer thickness in the ICL laser is determined by the requirement of the electronic structure and at the same time, the entire ICL structure has to be grown while keeping minimum excess strain. Each layer is in either biaxial compression (AlSb and GaInSb) or biaxial tension (InAs). By choosing the right thickness, ideally, the averaged lattice constant of the ICL can be matched to the GaSb substrate and the excess strain can be compensated. Stress in interband cascade lasers will be discussed in the next section.

2.3.3 Stress in interband cascade lasers

The band structure for III-V semiconductors consists of the conduction band and three valence bands. These three valence bands are heavy-hole (HH), light-hole (LH), and split-off hole (SO) bands. The conduction band can be considered as a remainder of the s atomic orbital and three valence bands can be viewed as the remainder of the three p atomic orbital (p_x, p_y, p_z) [42]. When the bulk material is under no strain, the HH and LH bands are degenerate at the valence band edge and

the SO band is formed at a lower energy level due to spin-orbit coupling. As a result, the electron can relax from the conduction band to the HH and LH bands.

HH states have a stronger transition strength for an electric field polarized perpendicular to the state $\boldsymbol{k}$-vector while LH states have a stronger transition strength for an electric field polarized parallel to the $\boldsymbol{k}$-vector [43]. In the bulk material, the conduction band to HH and conduction band to LH transition strengths are the same since the transition strength is spatially averaged. However, in the quantum well, the distribution of the k-vector is not spatially uniform. Therefore, a quantum well transition from the conduction band to the HH valence band is formed for light polarized parallel to the plane-TE polarization and a transition from the conduction band to the LH valence band formed for light polarized perpendicular to the plane-TM polarization.

As we mentioned in the earlier section, when we grow the IC laser structure using MBE, we create a lattice mismatch in the active region due to the GaInSb material. This lattice mismatch puts the active region under compressive strain. Compressive stress in the quantum well can cause two effects. First, the conduction band is moved up and the valence bands are moved down, thus increasing the band gap energy. Second, under compressive strain, the HH and LH bands separate from each other. The HH band is shifted up and the LH band is shifted down. For tensile stress, first, the conduction band is moved down and the valence bands are moved up, decreasing the band gap energy. Second the HH band is shifted down and LH band is shifted up relative to each other. Both cases are shown in Figure 2-7.

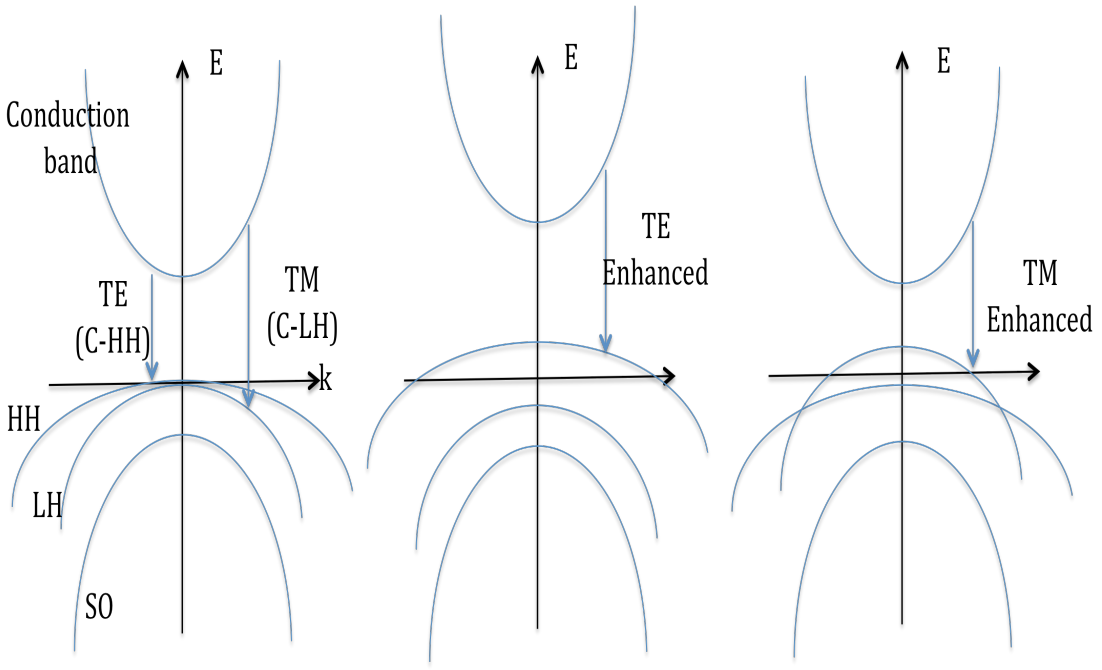

(a) No Strain (b) Compressive Strain (c) Tensile Strain

Figure 2-7 Interband cascade laser band structure and effect of strain on the polarization dependence of optical transition

Figure 2-8 shows the actual band shifting with compressive stress in IC lasers. Under compressive strain, the HH band H_1 quantum state is shifted up closer to the upper energy state than the LH band L_1 quantum state. This band splitting affects the Auger recombination and helps to reduce the intervalence band absorption, through the transitions between the HH, LH, and SO. The symmetric (E_{1S}) and the anti-symmetric (E_{1A}) energy doublets are also shown in Figure 2-8. The anti-symmetric energy level is higher than the symmetric energy level because the symmetric wave function has less integrated change in slope multiplied by the value of the wave function than the anti-symmetric wave function. These energy doublets are created due the double InAs quantum well in the active region. The symmetric energy state

has a much longer decay length into the hole region so that it increase the electron-hole wavefunction overlap. As a result, most of the radiative transition for our IC laser should be between the symmetric energy state and the H_1 energy state.

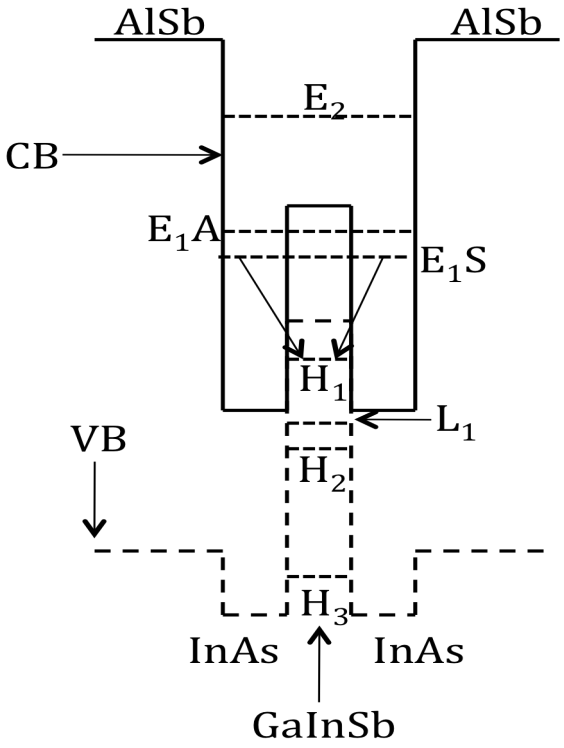

Figure 2-8 Effects of stress in the quantum well energy states of the interband cascade lasers [44]

For IC lasers, the GaInSb active region structure favors the transition between the conduction band to HH band which generates TE polarized light output. For QC lasers, the optical selection rules demand the electric field to be parallel to the epi growth direction, so it generates TM polarized light output. As a result, although we can make both IC and QC edge emitting lasers, it is difficult to make a vertical cavity QC laser since for light to come out vertically, the electric field needs to be parallel to the growth plane.

2.4 Laser Diode Characterization

In this section, we are going to focus on explaining the laser diode characterizations including carrier generation and recombination, photon generation and loss, extraction of internal parameters such as internal quantum efficiency and loss coefficient, and temperature dependence of the threshold current.

2.4.1 Carrier Generation and Recombination

To calculate the electron density N in the active region, we have to know the generation and various radiative and non-radiative recombination processes. We can write the carrier density rate equation as

$$\frac{dN}{dt} = G_{gen} - R_{rec} \tag{2-1}$$

where G_{gen} is the rate of injected electron and R_{rec} is the rate of recombined electron per unit volume in the active region. The generation rate can easily be found since we are pumping $\eta_i I/q$ electrons into the device, where η_i is the internal quantum efficiency, which comes from the injection efficiency of carriers to the active region. Only a certain percentage of injected electrons are being injected into the active region,

$$G_{gen} = \frac{\eta_i I}{qV} \tag{2-2}$$

where V is the volume of the active region.

Understanding the recombination process is not as simple as understanding the generation process since there are several recombination processes. There is a

spontaneous recombination rate R_{sp}, a stimulated recombination rate R_{st}, a non-radiative recombination rate R_{nr}, and a carrier leakage rate R_l.

$$R_{rec} = R_{sp} + R_{st} + R_{nr} + R_l \tag{2-3}$$

R_{sp}, R_{nr}, and R_l indicate the unstimulated carrier decay processes and R_{st} requires the presence of photons, and is proportional to the photon density. Also, R_{st} is proportional to the material gain which is approximately represented as $g \approx a(N - N_{tr})$ where, a is the differential gain, $\partial g / \partial N$, and N_{tr} is a transparency carrier density which represents the carrier concentration when the material has no gain. When there is no carrier generation, the carrier rate Equation (2-1) becomes $\frac{dN}{dt} = \frac{N}{\tau}$ where, τ is a carrier lifetime and $\frac{N}{\tau} \equiv R_{sp} + R_{nr} + R_l$.

The non-radiative recombination rate R_{nr} includes Auger recombination and Shockley-Read-Hall (SRH) recombination such as surface recombination and recombination at defect sites. The spontaneous recombination rate R_{sp} is proportional to the densities of electron and hole carriers and it can be written as $R_{sp} \sim BN^2$ where the coefficient B is called the bimolecular recombination coefficient.

Now, we can rewrite Equation (2-1) using the detailed expressions of generation and recombination rates

$$\frac{dN}{dt} = \frac{\eta_i I}{qV} - \frac{N}{\tau} - R_{st} \tag{2-4}$$

Under the steady state condition dN/dt=0 and assuming the blow threshold operation, we can ignore R_{st} and at threshold we can rewrite the carrier rate equation as

$$\frac{\eta_i I_{th}}{qV} = (R_{sp} + R_{nr} + R_l)_{th} = \frac{N_{th}}{\tau} \tag{2-5}$$

2.4.2 Photon generation and loss

The below threshold gain is insufficient to compensate for cavity losses and generated photons do not receive net amplification. However, when we increase the injection current, gain will overcome the cavity losses which include modal loss a_i and mirror loss a_m. Modal loss a_i represents optical losses such as waveguide light scattering and free carrier absorption. Mirror loss a_m refers to the Fresnel reflection of the cleaved facets of the laser. When light is traveling in the laser cavity, the photon density increases proportionally to the gain coefficient g and an incoming photon density N_p.

$$dN_p = gN_p\Delta z \Rightarrow N_p + \Delta N_p = N_p e^{g\Delta z} \tag{2-6}$$

Figure 2-9 shows the growth of the photon density from the incoming photon density N_p to the exciting photon density $N_p + \Delta N_p$ as the light travel through the gain medium.

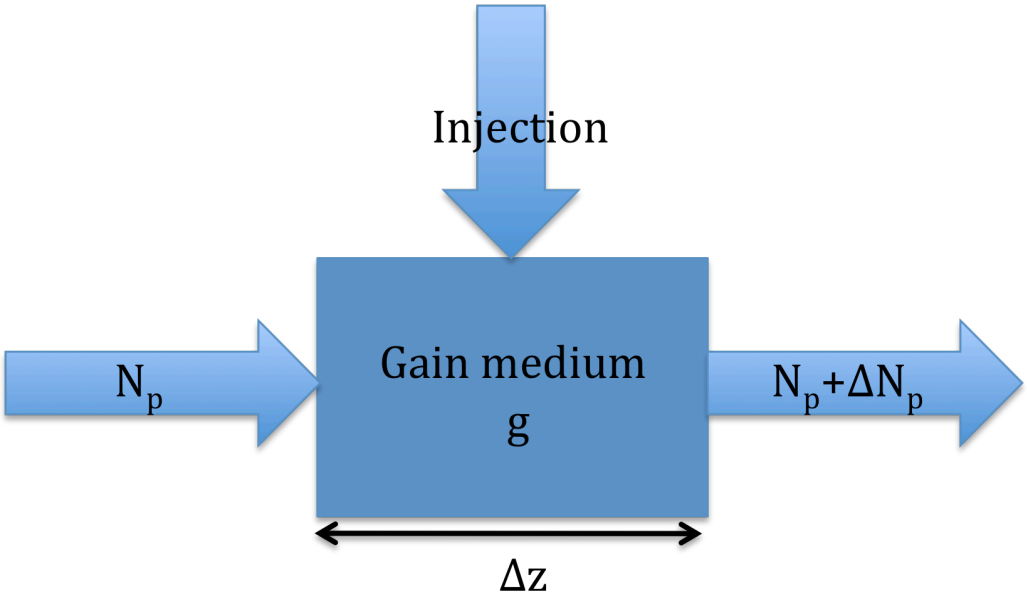

Figure 2-9 Photon density growth as the light travel through the gain medium

Figure 2-10 illustrates the laser cavity of our ICL semiconductor laser. r_1 and r_2 represent the electric field reflection coefficients at each facet, a_i represents the internal modal loss and β represents the propagation constant at threshold. We get

$$r_1 r_2 e^{(\Gamma\frac{g_{th}}{2}-\frac{a_i}{2})2L} e^{-i\beta 2L} = 1 \tag{2-7}$$

where Γ is the confinement factor and g_{th} is the gain at threshold.

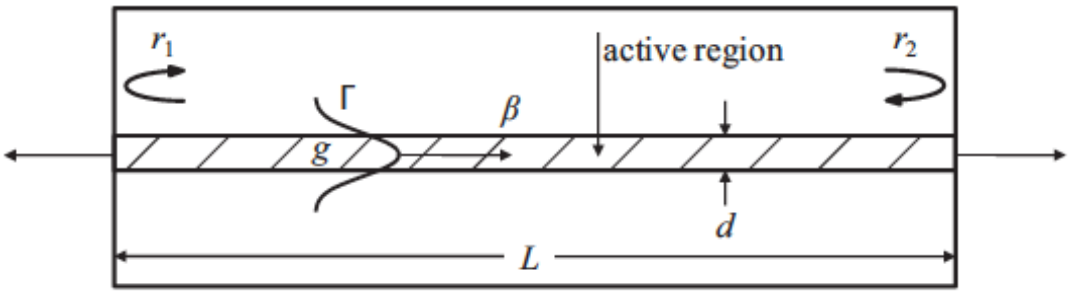

Figure 2-10 the laser cavity of ICL semiconductor laser

Equation 2-7 shows that the electric field needs to remain the same after one full round trip of 2L. As result of this, at threshold gain, is equal to loss. Note that g_{th} and a_i are defined for the field intensity and Equation 2-7 shows the electric field. This is why we used $g_{th}/2$ and $a_i/2$.

From the real part of Equation (2-7) we can get

$$\Gamma g_{th} = a_i + \frac{1}{2L}\ln\left(\frac{1}{R}\right) \tag{2-8}$$

where $R=r_1r_2$ and $r_1=r_2$ if there is no coating on the facets. The mirror loss is defined as $a_m = \frac{1}{2L}\ln\left(\frac{1}{R}\right)$ and we can rewrite Equation (2-8)

$$\Gamma g_{th} = a_i + a_m = \frac{1}{v_g \tau_p} \tag{2-9}$$

where τ_p is the photon decay rate and v_g is the group velocity of the light in the waveguide.

From Equation (2-9), we can derive an expression for R_{st} in Equation (2-4).

$$dN_p = gN_p \Delta z \Rightarrow \frac{dN_p}{dz} = gN_p \Rightarrow \frac{dz}{dt}\frac{dN_p}{dz} = v_p gN_p \Rightarrow \frac{dN_p}{dt} = R_{st} = v_p gN_p \tag{2-10}$$

Above threshold the carrier density gets clamped at its threshold value. When the injected current is increased to a value above threshold, the carrier density and gain increase. The stimulated recombination R_{st} also increases and this reduces the carrier density and gain until steady state is reached. When we combine Equations (2-4), (2-5), and (2-10) we can get

$$\frac{dN}{dt} = \eta_i \frac{(I - I_{th})}{qV} - v_p gN_p \tag{2-11}$$

At the steady state condition we can get

$$N_p = \frac{\eta_i (I - I_{th})}{q v_p g_{th} V} \tag{2-12}$$

We can also get the optical output power since it is proportional to the photon density N_p. E_o is the optical power in the cavity. By multiplying by the photon density, the photon energy, the cavity volume and the energy loss rate through the mirrors, we can write

$$P_o = v_p a_m N_p h\nu V_p \tag{2-13}$$

where V_p is the cavity volume. V is different than V_p since it refers to the volume of the active region where we have the optical gain. Substituting from Equation (2-12) and (2-9) using the confinement factor $\Gamma = V/V_p$ in Equation (2-13), we can write

$$P_o = \eta_i \left(\frac{a_m}{a_i + a_m} \right) \frac{h\nu}{q} (I - I_{th}) \tag{2-14}$$

By defining differential quantum efficiency as

$$\eta_d = \frac{\eta_i a_m}{a_i + a_m} \tag{2-15}$$

we can simplify Equation (2-14) as

$$P_o = \eta_d \frac{h\nu}{q} (I - I_{th}) \tag{2-16}$$

This equation only represents the total power from both facets. If we have un-coated facets then half of output power will be emitted from each laser facet. The differential quantum efficiency can be found by measuring the slope of the output power vs. current ($\Delta P/\Delta I$) and multiplying this by the inverse of the photon energy.

$$\eta_d = \frac{q}{h\nu} \frac{dP_o}{dI} \tag{2-17}$$

2.4.3 Parameters Extraction

By performing the current, voltage, and light (IVL) measurements, we can extract important parameters such as the threshold current I_{th}, the turn on voltage, the differential resistance R_d, the slope efficiency dP_o/dI, the wall plug efficiency (WPE), the maximum power P_{max}, etc. Also by measuring different length devices, we can extract the internal quantum efficiency η_i and the internal loss coefficient a_i.

There are two possible methods to extract the internal loss coefficient and the internal quantum efficiency. The first method is the length dependence of the threshold current density, J_{th}. From Equations (2-5) and (2-8) we can get

$$J_{th} = \frac{q}{\eta_i \tau}(n_{tr} + \frac{a_i}{\Gamma dg/dn} - \frac{\ln R}{L_{cav}\Gamma dg/dn}) \tag{2-18}$$

In these expressions, n_t describes the transparency current density, a_i is the internal loss coefficient, $\Gamma\frac{dg}{dn}$ is the modal differential gain, η_i is the total internal efficiency and is equal to the number of cascades N multiplied by the internal quantum efficiency per cascade. Equation (2-18) shows the linear dependence of the threshold current density vs. 1/cavity length. It turns out that n_{tr} is small compared to the second and third terms. If this is the case, we can extract the internal loss coefficient from the linear dependency J_{th} vs. $1/L_{cav}$ plot.

The second method is to use the slope efficiency. Using Equation (2-14) and the mirror loss equation, we can write

$$\frac{1}{\eta_d} = \frac{h\upsilon}{2q}\frac{1}{S} = \frac{1}{\eta_i} + \frac{1}{\eta_i \ln\frac{1}{R}} a_i L_{cav} \tag{2-19}$$

where η_d is the differential quantum efficiency, S is the slope efficiency, h is the Planck constant, τ is the carrier lifetime, and υ is the emission frequency.

Equation (2-19) states that there is a linear relationship between 1/S and the cavity length and from the 1/S vs. cavity length plot, we can also extract the internal quantum efficiency and internal loss coefficient, assuming that R is known. In Equations (2-18) and (2-19), η_i is assumed to be the same in both expressions,

although strictly speaking η_i in Equation (2-19) is a differential quantity measured above threshold and η_i in Equation (2-18) is a below threshold quantity [45].

2.4.4 Temperature Dependence of Threshold Current

N_{tr} and g_0 show a significant temperature dependence. The transparency carrier density increases with temperature while the gain parameter is reduced because pumped carriers spread over a wider range in energy with higher temperatures. Also Auger recombination and carrier leakage both act as additional temperature dependence sources. We typically assume an experimental dependence for I_{th} as temperature

$$I_{th} = I_0 e^{T/T_0} \tag{2-20}$$

where T_0 is the characteristic temperature of the laser and is a parameter used to express the temperature sensitivity of the laser. The higher the T_0 value, the better the thermal performance of the device. The measured interband cascade laser T_0 value is approximately 45K, which is a low value compared to competing technologies that were mentioned in earlier sections. We will talk about the characteristic temperature in detail in later chapters.

Chapter 3: Experimental Procedures

3.1 Introduction

In this chapter, we are going to discuss the experimental procedures including the mask design and the wet/dry etching process for laser device fabrication. The layer stack for our interband cascade lasers were grown by Maxion Technologies and the lasers were processed and fabricated in our cleanroom facility. They were then mounted and tested in our laboratory. We have established and optimized both the wet etching and dry etching with flash wet etching processes. Dry etching of the ridge waveguide with flash wet etching allows us to achieve a vertical sidewall with minimum sidewall roughness. Dry etched waveguides also give better thermal performance. This will be discussed in the next chapter. Using the dry etching method along with other laser improvements allowed us to operate our laser CW at room temperature. For current-voltage-light measurements below 15°C, a custom made vacuum chamber was used.

3.2 Mask Design

We have designed two masks, one for a straight waveguide only and the other for an angled waveguide. For the angled waveguide mask, we designed several different ridge widths, from 12um to 24um with an increment of 3 um, as well as various facet angle of, 0°, 7°, 7.5°, 8°, 8.5°, 9°, and 9.5°. Using this mask we can

cleave devices at lengths of 1, 2, 3, and 4 mm long. A detailed mask layout and design is shown in Figures 3-1 and 3-2.

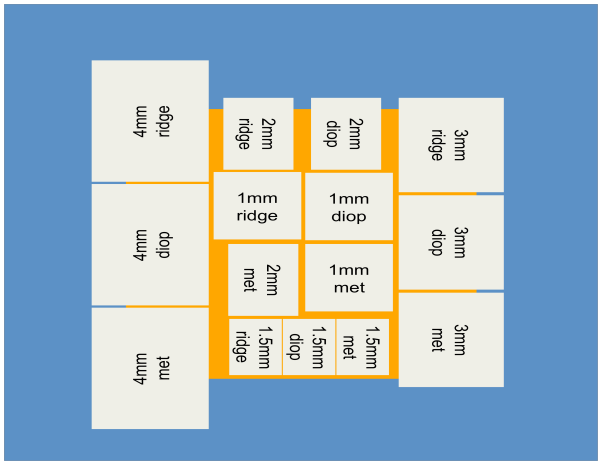

Figure 3-1. IC laser mask layout

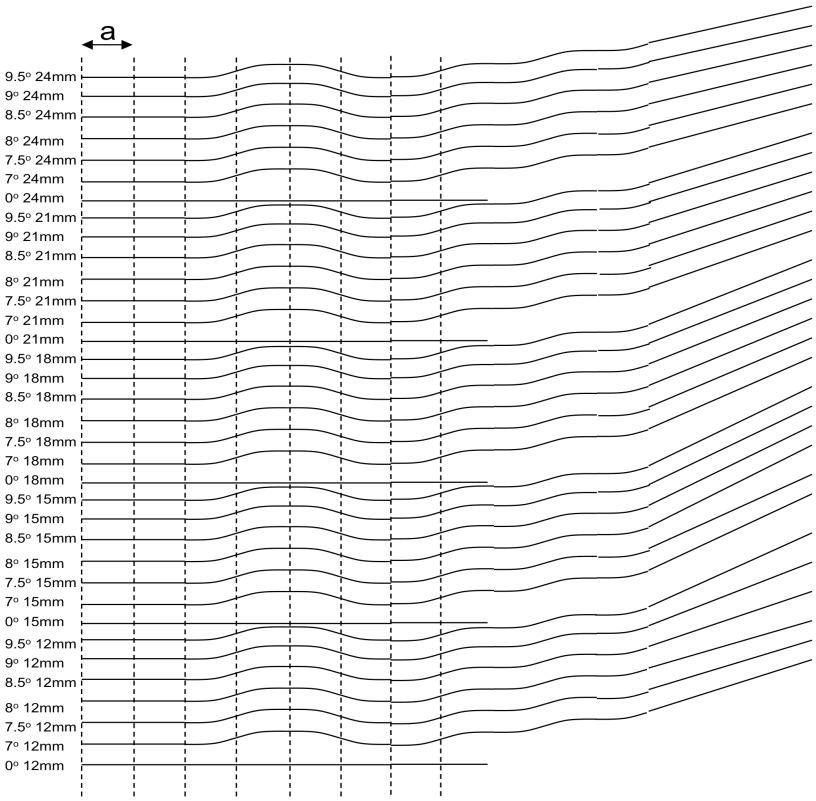

Figure 3-2 IC laser mask design schematic

For a straight waveguide mask, we also designed several ridge widths from 10 um to 16 um ridge in increment of 3 um. Also we can cleave up to 5mm long devices with an increment of 1 mm in cavity length.

3.3 Device Fabrication

The fabrication process starts by cutting in smaller pieces a quarter wafer of ICL material. After cutting the wafer to the appropriate size, we perform a standard solvent cleaning process, which includes a 30 s rinse with acetone, methanol, and isopropanol. Then we bake the samples at 120 °C for 10 mins in an oven to remove all humidity that might affect the photoresist processing. The cleaning procedure ends with a reactive ion etching (RIE) oxygen cleaning. We use very low RF power to avoid any plasma damage on the InAs cap layer. We have found that RIE cleaning step is necessary to have a good sidewall profile.

We will now discuss the wet etching process steps and we will explain the dry etching fabrication steps afterward. Oxygen plasma cleaned samples are spin coated with a hexamethyldisilazane (HMDS) adhesion promoter to ensure adhesion between the samples and the photoresist. Usually, HMDS promoter is used for dielectric films but we have found that the use of HMDS also helps to get smooth sidewalls and better adhesion. Then AZ5214E photoresist is spun on the samples at 4000 rpm and this creates about a 1.4um thick photoresist film on the samples. Since we etch through the active region, the thickness of the photoresist at the edge of the trench is very thin. Normally we use single layer AZ5214E but sometimes AZ5214E photoresist cannot even be used due to the thin side wall coverage. In order to have a thick photoresist at the edge of the sidewall, we tried various photoresist coating

techniques, which include AZ5214E double coating at 4000 rpm and 2000 rpm, AZP4620 coating at 4000 rpm, and SPR 220-7 coating at 6000 rpm. We have found that AZ 5214E double coatings at 2500 rpm or SPR 220-7 are the best choice for deep etching processing and that the AZP4620 was too thick to do dielectric opening alignment. SEM pictures of various photoresist coating techniques are shown in Figure 3-3.

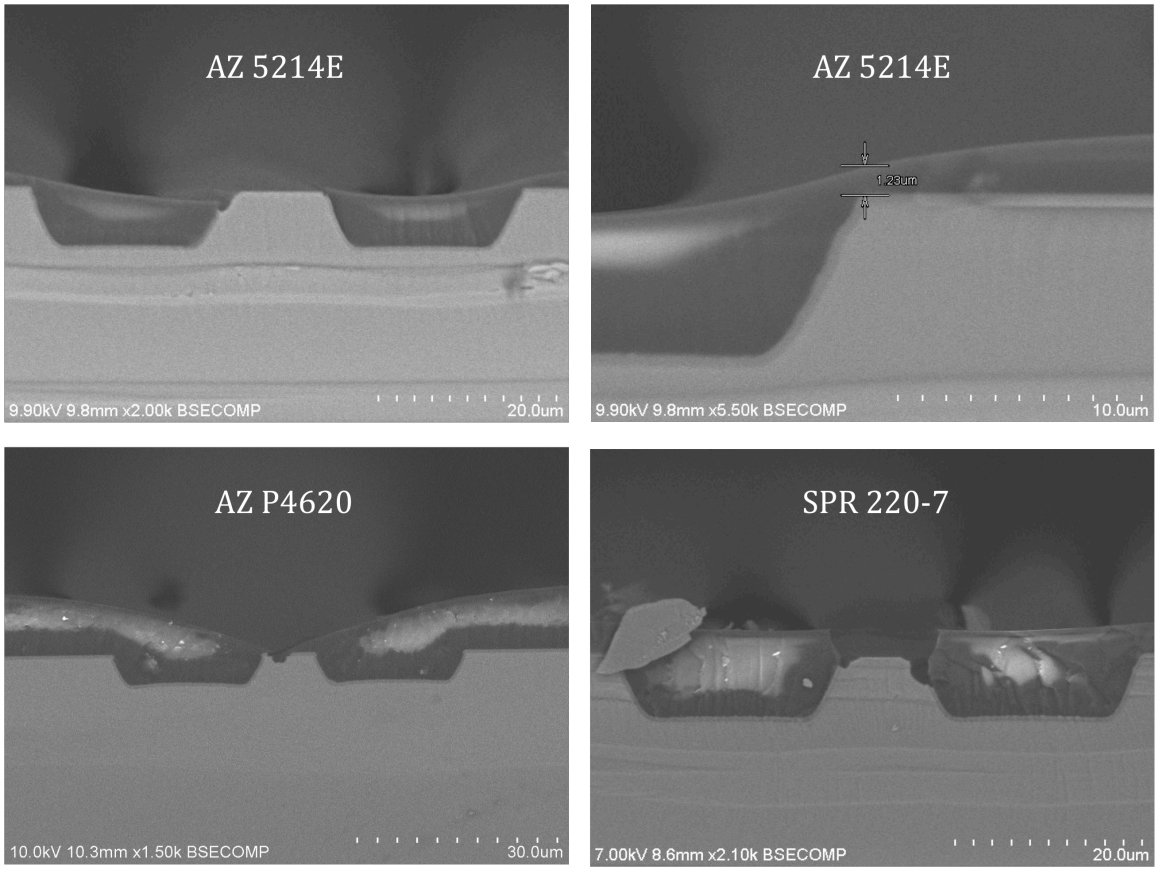

Figure 3-3. SEM pictures of various photoresits etching tests

After the photoresist coating, samples are exposed with UV light for 8s and developed with a mixture of AZ400K and deionized water at a ratio 20 ml: 80 ml (1:4). The first photolithography step is for defining the ridge area. After the ridge

pattern development, we etch the sample either using a chemical wet process or a dry etching process. For the wet based process, we use a solution of tartaric acid ($HOOC(CH_2O)_2COOH$), phosphoric acid, hydrogen peroxide and deionized (DI) water at a ratio 5 g : 30 ml : 30 ml : 90 ml and etch for 5min. For 5min wet etching, we get about 3.5um etching depth. During the wet etching process, the ambient temperature is very critical and has to be monitored. If the ambient temperature is not stable then the etch rate can be changed dramatically. The ICL wet etching process is an isotropic etching process. Different materials have different etching rate. So it creates some undercut along the sidewall as shown in Figure 3-4. This undercut will degrade the IC laser thermal performance since metal contact cannot reach the undercut area and this creates an air gap between the active region and the metal contact. This is the main reason why we are using a dry etching method with flash wet etching.

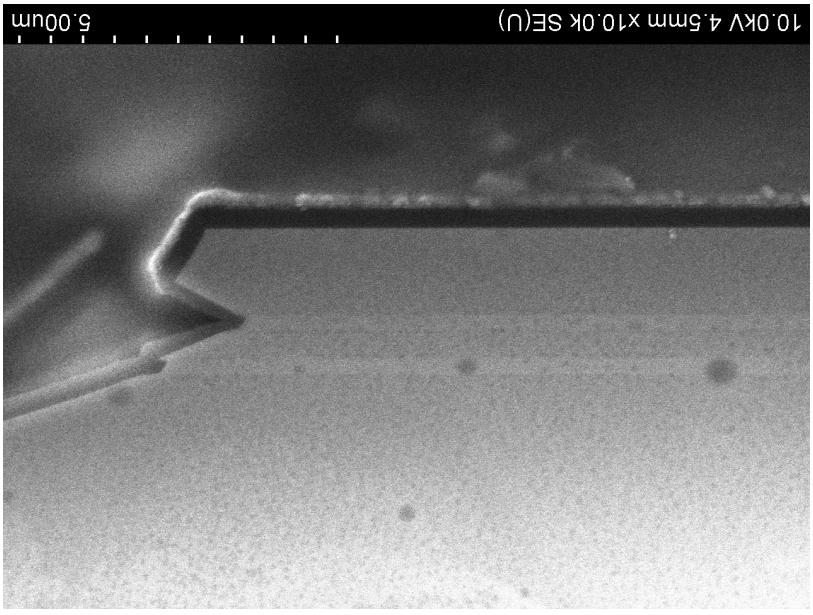

Figure 3-4. SEM picture of wet etched undercut along the sidewall

After the first photolithography step and etching process, 3000 Å of silicon nitride (Si_3N_4) is deposited by plasma enhanced chemical vapor deposition (PECVD). PECVD will grow high quality conformal silicon nitride at the rate of 160 Å/min at 200 °C which helps to prevent shorting of the device. After the PECVD deposition, we perform the second photolithography step for the dielectric opening. Dielectric opening will allow carriers to flow through the active region of the ridge. After patterning, we use the SF_6 based RIE process (pressure 150 mTorr, RF 100 W, SF_6 40 sccm, and O_2 1 sccm) to etch the silicon nitride on the ridge. The etch rate is about 180 Å/sec. We design the dielectric opening to be about 2~3 um narrower than the ridge width. This allows us to have some alignment tolerance. After the dielectic opening etching, we remove the photoresist by immersing the sample in acetone.

The third photolithography step is for defining the first epi-side metal contact. This step is different from the other two lithography steps since we use the technique called “image reversal”. Image reversal is used to create an undercut of the photoresist, which facilitates the metal lift-off process. The photoresist that we use is called AZ5214E and it can be used both as a positive or a negative (image reversal) photoresist. Figure 3-5 shows both the standard and image reversal processes.

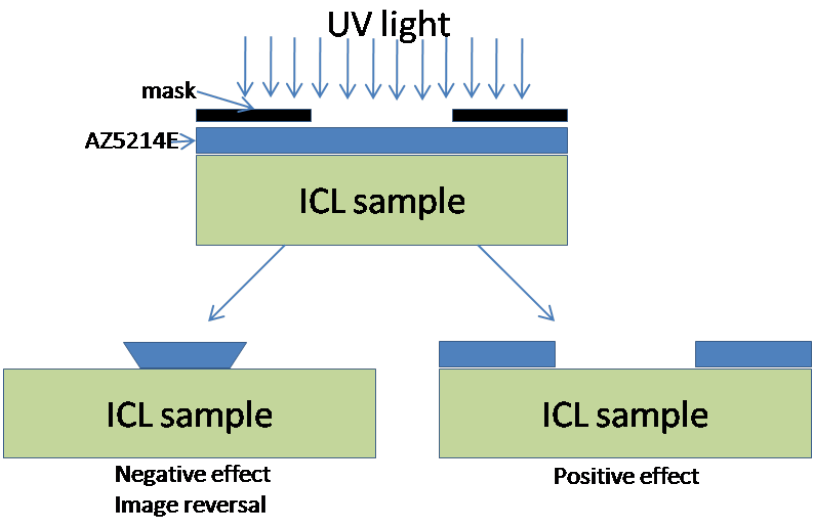

Figure 3-5 Positive and Negative effect of AZ5214E photoresist

Right before the metalization, we immerse the samples in 10 % HCl for 30 seconds to remove the native oxide that might have grown during the fabrication process. This step enhances the adhesion of the metal contact. For epi-side metalization, we evaporate Ti/Pt/Au, 300 Å/1500 Å /1000 Å. Titanium is used for enhancing the adhesion and platinum is used as a blocking layer to prevent diffusion of gold. We sometimes use Ar+ ion bombardment for 50 seconds before evaporation. Ion bombardment has improved metal adhesion. However, it also has made it harder to lift-off, since ions also affect the edge of the overhang. After the first metallization, we immerse the sample in acetone to remove the photoresist. When the photoresist is being removed, deposited metals are also removed completing the image reversal process. The second epi-side metallization is for gold electroplating. We electroplate thick gold on top of the evaporated gold to improve the thermal dissipation of the heat that is created in the active region. We use a Transene Inc. TSG-250 plating solution which is electrolytic, so we must connect all the waveguides. For connecting the

waveguides, we usually use a thermal evaporator and evaporate either titanium or gold. This metal connection is shown in Figure 3-6. After the metal connection we prepare the electroplating solution.

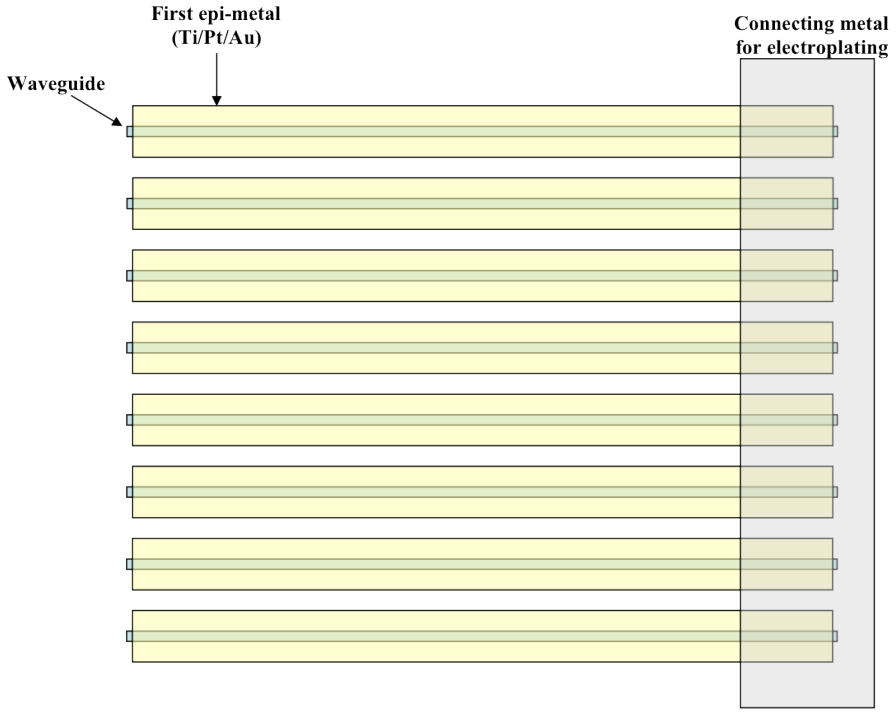

Figure 3-6 Schematic of connecting metal for electroplating

In order to coat a uniform gold film, we have to heat the solution to 60 °C and agitate it for at least 30 min before electroplating. Before the electroplating, we do fourth photolithography step. This photolithography step creates the cleaving lane between the electroplating metal. Without the cleaving lane, we cannot cleave the sample since the electroplated gold is too thick to scribe. This step is shown in Figure 3-7.

For a $1cm^2$ sample, we flow a current of about 2.7 mA for 30 min to electroplate 5um of gold. After electroplating 5um of gold, we evaporate Pt/Au once

again, in order to improve the layer smoothness and create a diffusion barrier in the electroplated gold for the case of Au/Sn epi-down mounting.

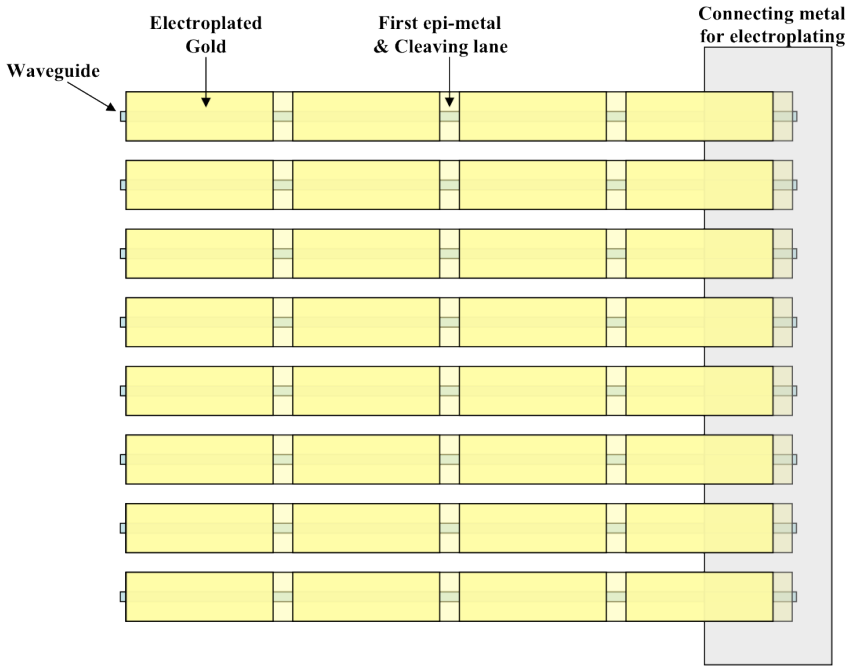

Figure 3-7 Schematic of waveguide after electroplating

After the electroplating process is completed, we remove the photoresist by immersing the sample in acetone. Then we mount the sample on a microscope glass slide using wax for polishing. The melting temperature of wax is about 130°C~150°C. Polishing the samples allows us to cleave our sample in order to create the mirror like facets for the Fabry Perot cavity. We usually polish the samples down to 120 um including 20 um of wax. Then we do back side metal evaporation. As it was mentioned earlier, before the metallization, the samples are immersed in a 10 % HCl solution for 30 seconds. For backside metallization we use the same metals as for the epi-side, Ti/Pt/Au.

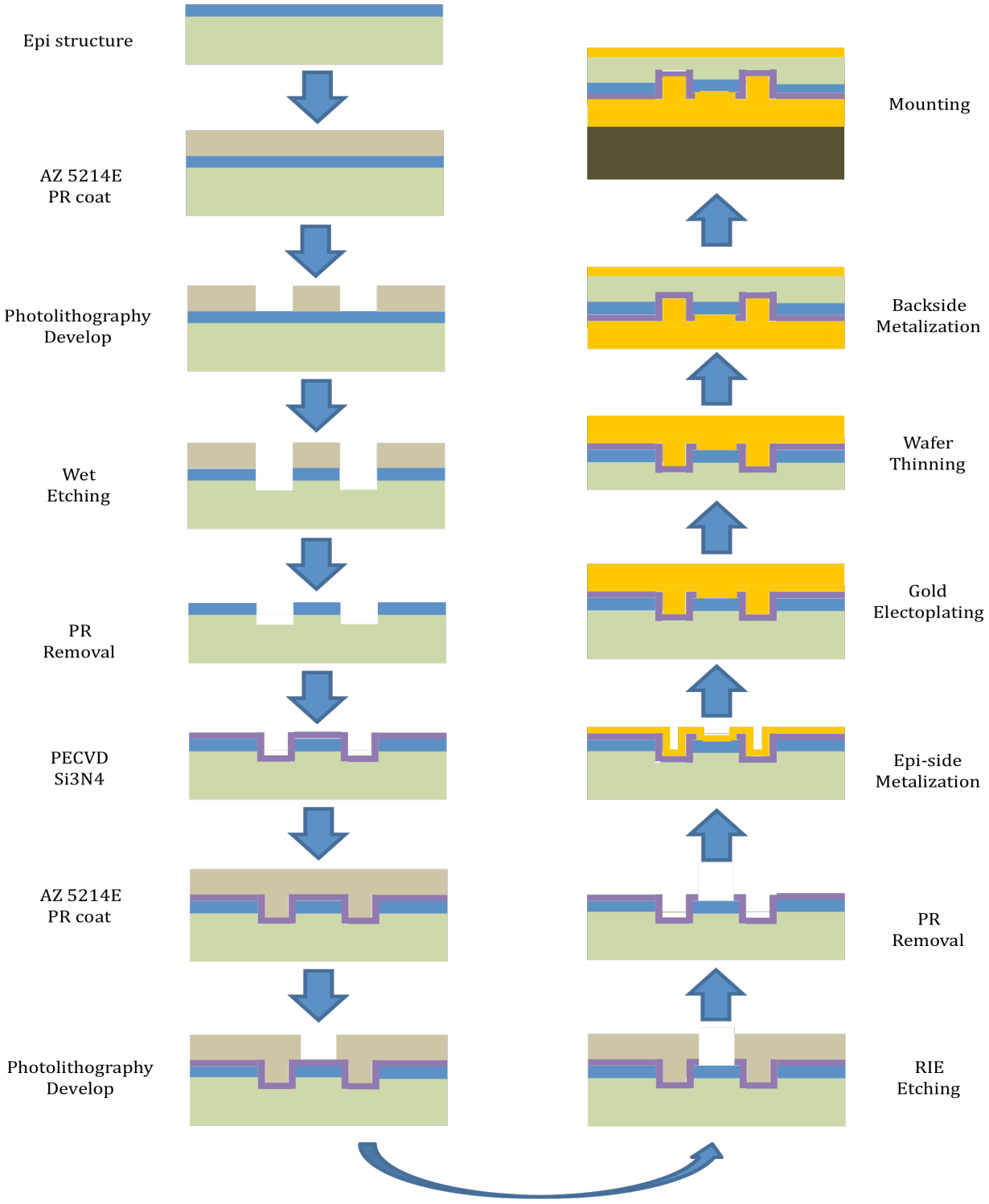

Figure 3-8. Wet etching based IC laser fabrication steps

The final fabrication step is cleaving. Once we finish with the evaporation of the backside metal, we remove the samples from the glass slide and we cleave the samples to obtain different length laser bars and then we dice each individual device for mounting either epi-up or epi-down. Details on the wet etching based ICL fabrication steps are shown in Figure 3-8.

The dry etching based ICL fabrication process is very similar to the wet process except in its first few steps. Since the AZ5214E photoresist cannot be used as an etching mask, we start the ICL process by depositing silicon nitride. For the dry etching method, we have extra photolithography steps for etching the silicone nitride film. After we do our first photolithography step, we etch the silicon nitride film using ICP-RIE and then we etch the ICL material by inductively coupled plasma-reactive ion etching (ICP-RIE). For dry the etching, we use a BCl_3 based ICP-RIE process (pressure 2.5 mTorr, RF 100 W, ICP 400 W, Ar 2.4 sccm, and BCl_3 12.5 sccm). We also use the helium backing for cooling the sample holder. For 5mins of etching time, we get about a 3.5um deep trench.

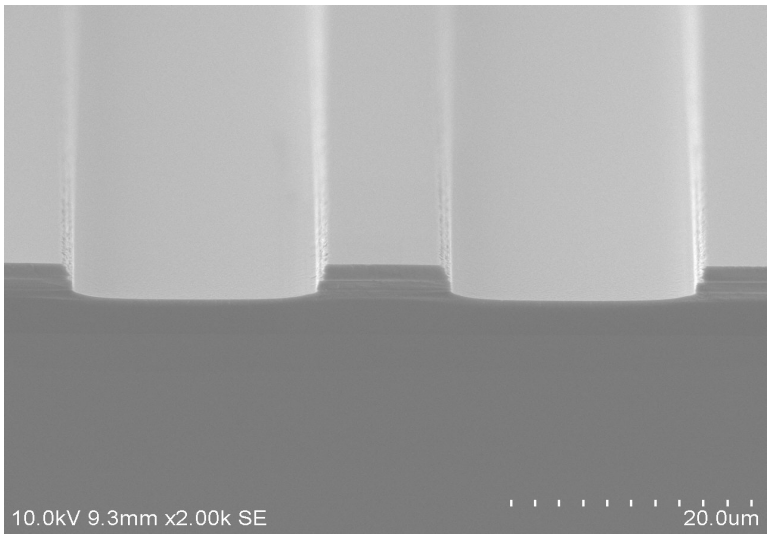

Figure 3-9 Dry etched IC laser waveguide

As we mentioned earlier, the dry etching process gives us a couple of advantages over wet etching. First, dry etching allows us to control the etching depth precisely as well as to achieve vertical sidewall profile. Second, since it is an anisotropic etching, we can improve the thermal performance. A SEM picture of a dry etched waveguide picture is shown in Figure 3-9. After dry etching using ICP-RIE, we do flash wet etching for 15~30s using the wet etchant (a solution of tartaric acid, phosphoric acid, hydrogen peroxide and DI water) for side wall smoothness. As we can see from Figure 3-10, the dry etched device performed very similar to the wet etched device. The rest of the dry etching fabrication steps are the same as for the wet etching approach.

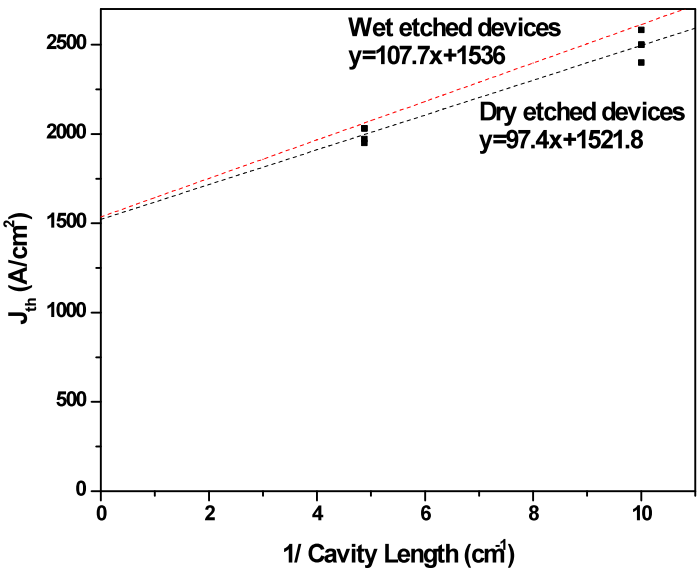

Figure 3-10. Wet and dry etched device performance comparison

3.4 IC Laser Test Set-Up

The device fabrication steps end with the dicing of the individual devices. Now these devices need to be characterized. For device testing, we used an Avenex voltage pulse generator, a Stanford Research boxcar, and a lead selenide detector from Judson Technology. We have fabricated a vacuum mount that can be used for both room temperature and low temperature (such as -20°C) operation. This vacuum mount has a vacuum feed through for all the electrical connections and it includes a thermal electric cooler. It also has a water inlet/outlet for effective cooling. The schematic and the actual mount pictures are shown in Figure 3-11.

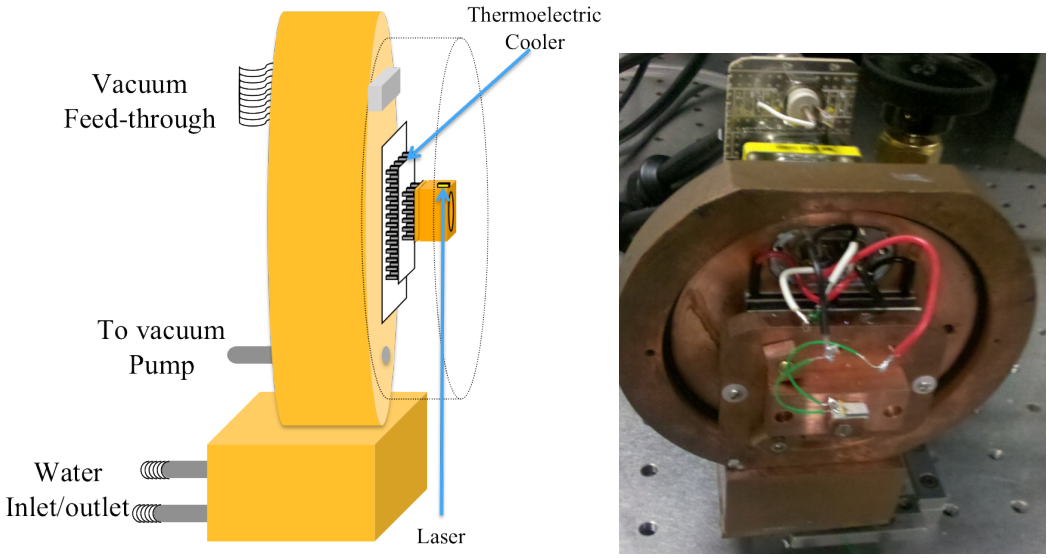

Figure 3-11 Low temperature mount schematic and picture

Chapter 4: Thermal Analysis

4.1 Introduction

As we mentioned in the previous chapter, until a few years ago, interband cascade lasers (ICLs) could not operate CW at room temperatures. One aspect of ICLs that has slowed progress towards high temperature CW performance relates to the low thermal conductivities of their constituent materials. ICLs use semiconductor heterostructures, primarily superlattices formed from thin InAs and AlSb layers. These superlattices are known to have low thermal conductivities due to both the inherently low thermal conductivities of their constituent materials and due to the large numbers of interfaces they contain [46]. Recent studies show that the thermal conductivity of SL along the growth axis is almost 1/10 the value of bulk materials due to phonon group velocity reduction and phonon wave scattering at the interfaces in SL cladding layers. Recent work has shown that the InAs/AlSb superlattice material [46] has demonstrated a cross-plane thermal conductivity much lower than obtained from predictions based on the Fourier heat conduction theory that uses bulk material properties. Also, the experimental data show that superlattices grown at higher temperatures have smaller thermal conductivity and that post-growth annealing also reduces the thermal conductivity compared to unannealed samples. These results suggest that the nature of the interfaces between the InAs and the AlSb layers may play an important role in the heat conduction process.

Epi-Up and Down Model			
Region	**Material**	**k (W/m-K)**	**Thickness (um)**
Top Metal	**Au**	**297**	**5.3**
Insulator	**Si_3N_4**	**2**	**0.3**
Upper Cladding	**InAs/AlSb SL**	**2**	**1.4**
Upper SCR	**GaSb**	**32**	**0.2**
Active	**InAs/GaInSb**	**4**	**0.4422**
Lower SCR	**GaSb**	**32**	**0.2**
Lower Cladding	**InAs/AlSb SL**	**2**	**4**
Substrate	**GaSb**	**32**	**80**
Bonding	**In**	**82**	**2**
Submount	**AlN**	**285**	**1000**

Table 4-1 Thickness and thermal conductivity coefficients for each ICL layer

Since ICLs have a low T_0 parameter, they are particularly sensitive to the effects of increasing the active region temperature. A thermal simulation of such a laser can pinpoint the bottlenecks in the heat flow and indicate which regions are most detrimental to the high temperature performance of these lasers. In this chapter, we will discuss the thermal simulation and thermal impedance measurements.

4.2 Thermal simulation

In order to understand the laser's thermal behavior, we have made a thermal simulation of our ICLs using a finite element solver for solving the heat partial differential equation given in Equation (4-1),

$$\nabla \bullet (-k(x)\nabla T(x)) + S(x) = 0 \qquad (4\text{-}1)$$

where, k(x) is the material thermal conductivity, S(x) is the input power density, and T(x) is the resulting temperature distribution.

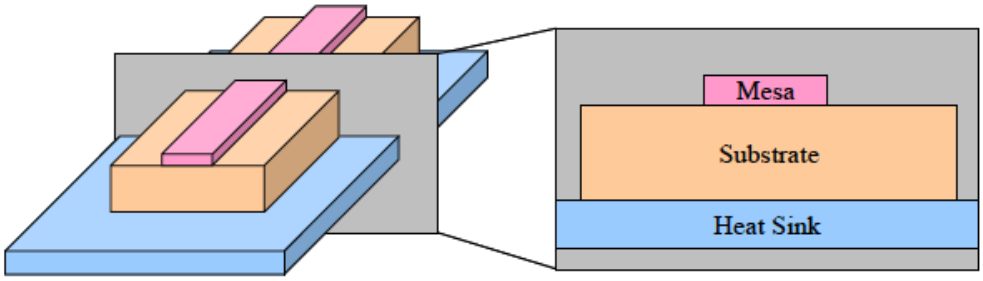

Figure 4-1 Translational invariance along the length of an interband cascade ridge laser

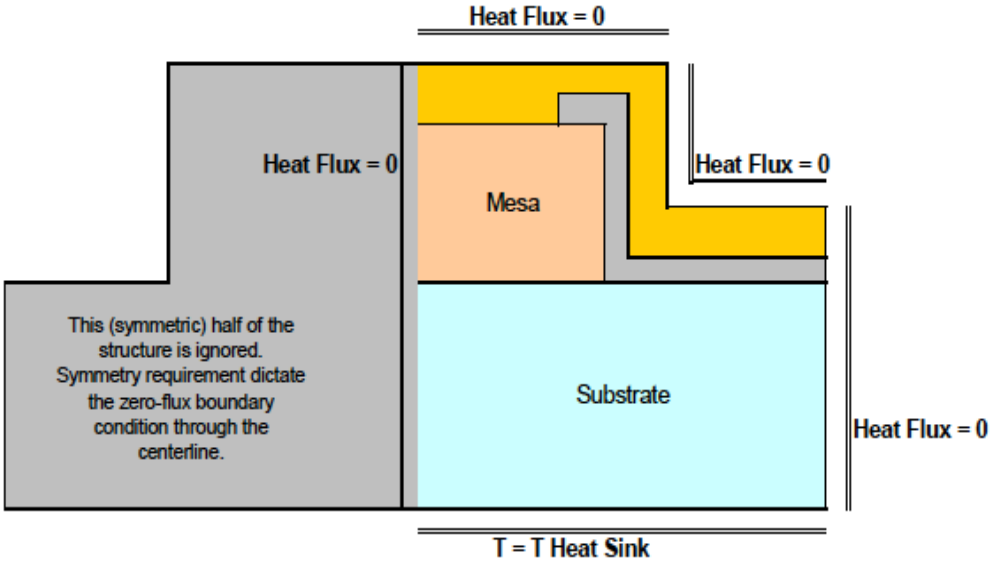

Figure 4-2 Boundary condition used in the IC laser steady state heat flow analysis

We can simplify the 3-D problem by taking advantage of the translational invariance along the length of the laser so we only consider a 2-D cross section similar to that shown in Figure 4-1. This is permissible for ridge laser devices that are very long compared to their widths and thickness. To uniquely determine a solution, boundary conditions on T(**x**) must also be specified. For our problem, they include the continuity of T and the normal derivative of the heat current at interfaces between different materials, setting the heat sink interface equal to a fixed temperature, and requiring zero heat current across the other external boundaries. This latter requirement derives from the assumption that the thermal conductivity of the ambient atmosphere is negligible, and that the structure is symmetric (device structures are nominally symmetric about the centerline of the laser mesa). These boundary conditions are illustrated in Figure 4-2.

Table 4-1 shows the thickness and thermal conductivity coefficient for each IC laser layer. As we can see from the table, both the upper and the lower cladding layer have very low thermal conductivity coefficients, resulting in low heat extraction efficiency from the active region where most heat is generated.

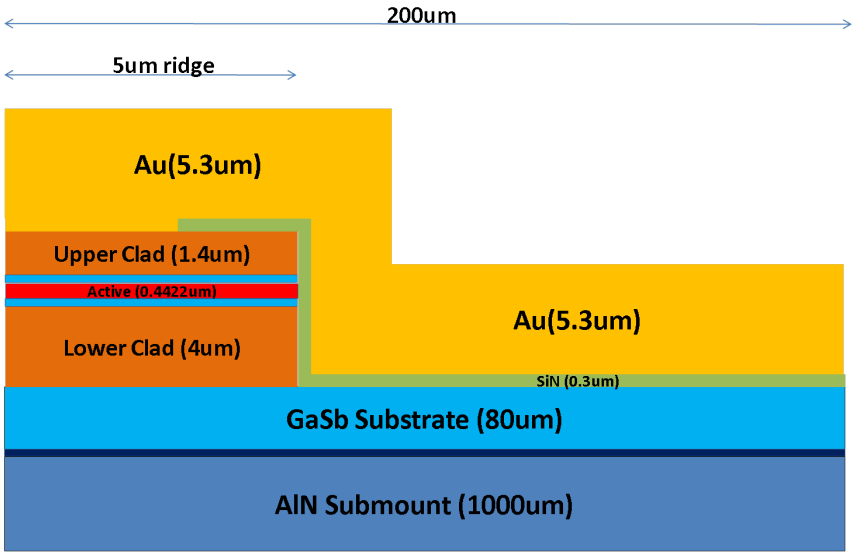

(a)

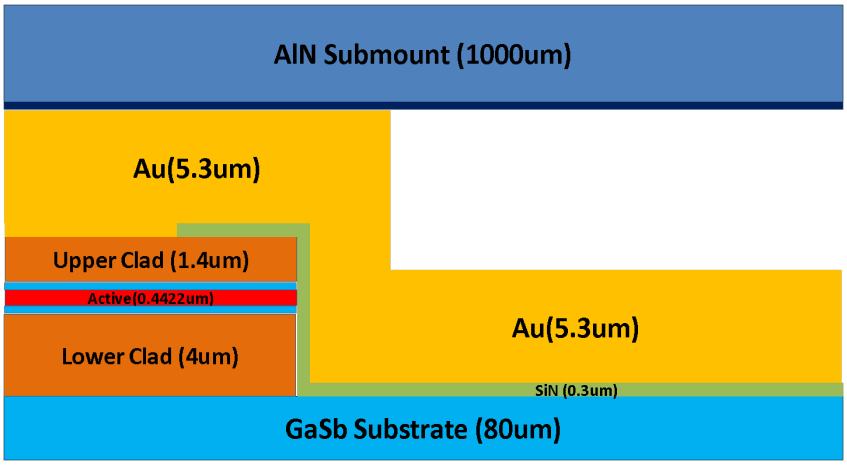

(b)

Figure 4-3 10um ridge ICL Epi-up and Epi-down mount simulation structure

We have simulated the heat flow based on a standard 10 um wide epi-up and epi-down mounted ridge laser, as shown in Figure 4-3. The current is fixed at 100 mA. First we have assumed that each layer is isotropic and that k is a scalar. We have simulated various epi-up and epi-down conditions, including the case of a 5 um electroplated gold layer on top of the laser, a 0.3 um thin evaporated gold layer, an etch through the active region and an etch only up to the separate confinement region

(SCR). For every simulation, the thermal resistance was extracted. The thermal resistance is defined as

$$R_{th} = \frac{T_{Active} - T_{HeatSink}}{I \times V} \tag{4-2}$$

where T_{active} is the temperature of the active region, $T_{HeatSink}$ is the temperature at the heat sink (25 °C), and IxV is the power dissipated in the device.

Detailed simulation results are shown in Figure 4-4 and Figure 4-5. As we can see from Figure 4-4 (a), epi-down mounting using evaporated indium should improve R_{th} by 20 % compared to epi-up mounting of the IC laser. The simulation results clearly show that we must do electroplating in order to improve the thermal behavior of the laser. For epi-up mounting, electroplating 5 um of Au does improve the thermal resistance by 37 % as compared to a thin 0.3 um evaporated Au layer. Figures 4-4 (c), (d) show that comparison between lasers that are etched through the active region and lasers that are etched only up to the separate confinement region (SCR). It is found that the etching depth plays a small role as long as the laser is etched through the active region.

The results are shown in Figure 4-5 which indicates a strong lateral outflux of heat from the active region, for both epi-up and epi-down devices, due to the poor thermal conductivity of the cladding layers. This is the main reason why narrow ridge devices can operate CW at room temperature but a broad area laser cannot be operated CW at room temperature yet.

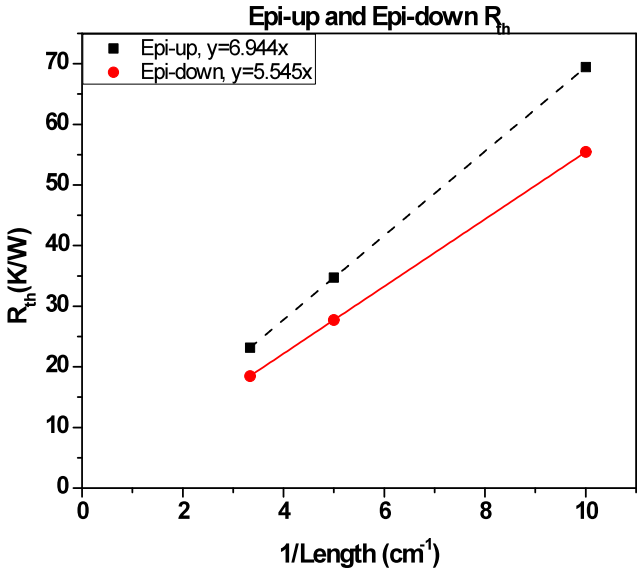
Epi-up and Epi-down R_{th}
Epi-up, y=6.944x
Epi-down, y=5.545x
R_{th}(K/W)
1/Length (cm^{-1})
0
10
20
30
40
50
60
70
0
2
4
6
8
10

(a)

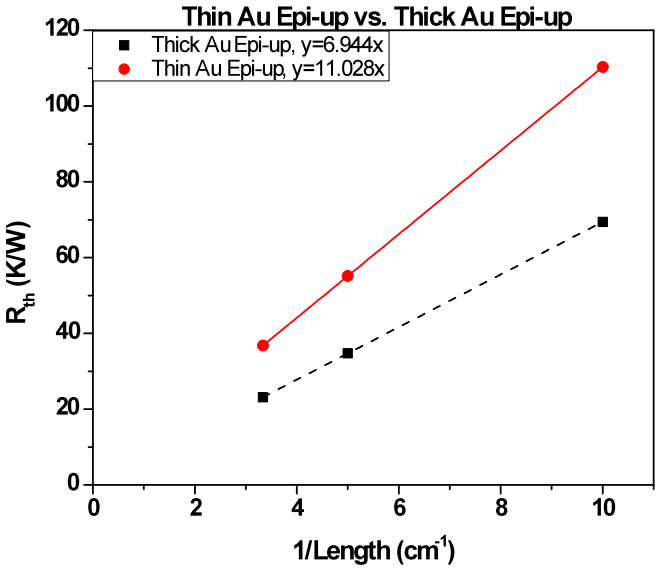
Thin Au Epi-up vs. Thick Au Epi-up
Thick Au Epi-up, y=6.944x
Thin Au Epi-up, y=11.028x
R_{th} (K/W)
1/Length (cm^{-1})
0
20
40
60
80
100
120
0
2
4
6
8
10

(b)

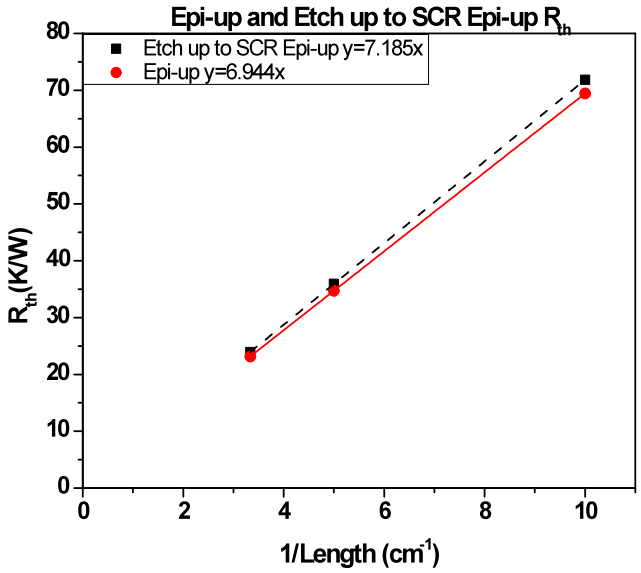

(c)

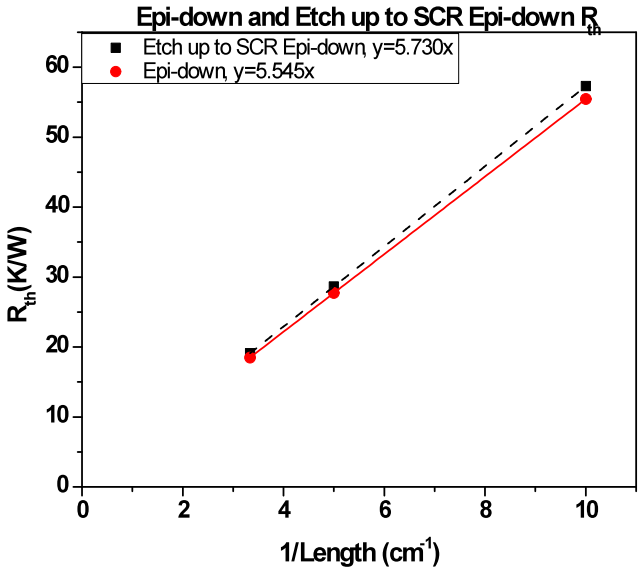

(d)

Figure 4-4. Thermal simulation results (a) epi-up vs. epi-down, (b) Thin evaporated Au epi-up vs. electroplated Au epi-up, (c) Etch through the active region vs. etch up to SCR epi-up, (d) Etch through the active region vs. etch up to SCR epi-down

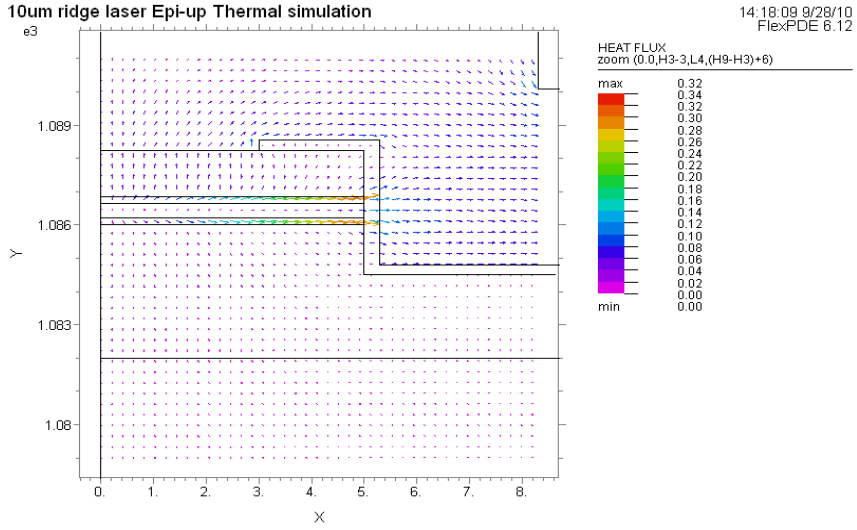

(a)

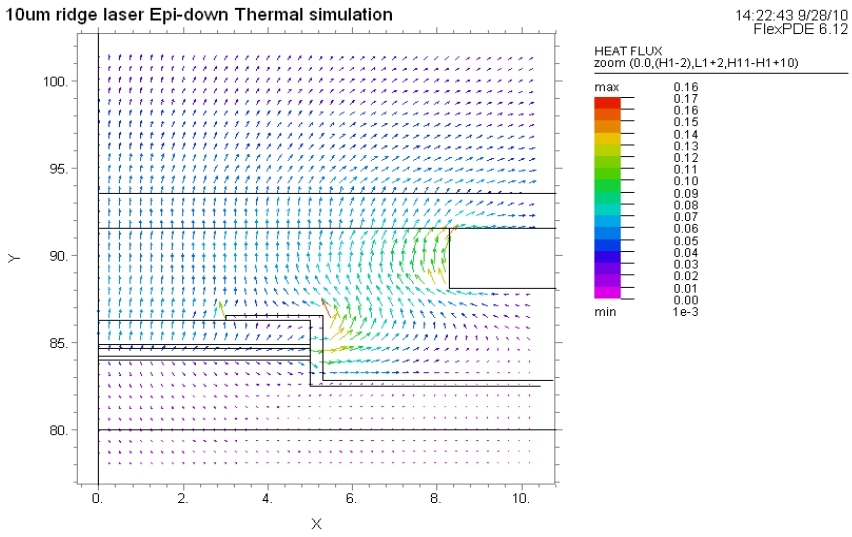

(b)

Figure 4-5. Heat Flux profile for Epi-up and Epi-down mount

At the beginning of the IC laser project, as we mentioned in the previous chapter, we etched our laser with a wet-etchant and it created unwanted voids right next to the active region since the metal deposition was completely directional. We

have tried to fill these voids with angle metal deposition but it made it hard to lift off the photoreisst. Figure 4-6 (b) shows the thermal simulation results of a wet etched device. We designed a structure similar to the SEM picture of a wet etched device and performed thermal resistance simulation. As we expected, there was very small lateral outflux of heat from the active region since the air-gap prevented the heat flow from the active region. As we can clearly see from Figure 4-6 (c), the thermal performance of a vertical sidewall or a dry etched device can be substantially improved. This is the main reason that we developed the dry etching fabrication steps mentioned in chapter 3.

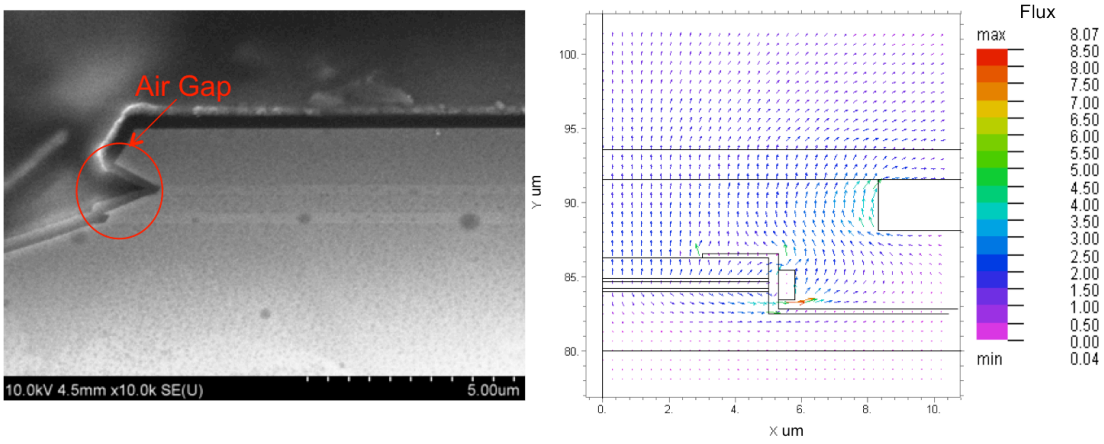

(a) (b)

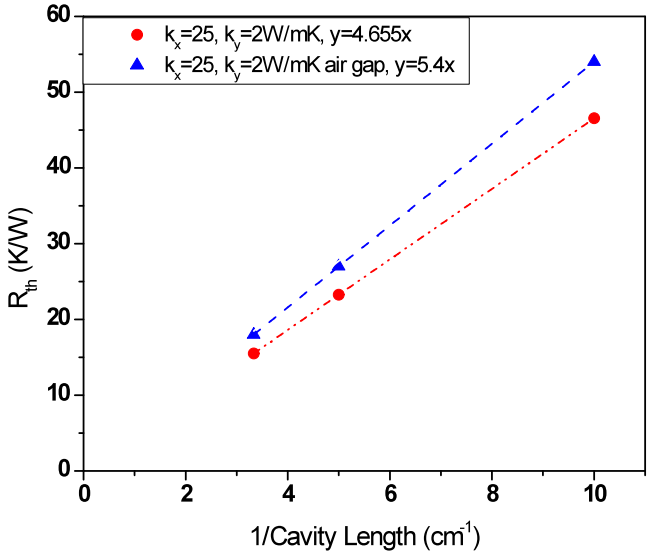

(c)

Figure 4-6 (a) SEM picture of wet etched device, (b) Heat flux with air gap right next to the active region, (c) Thermal resistance simulation results with/without air-gap

4.3 Thermal impedance measurement

The theoretical simulation results of R_{th} were compared with actual experimental R_{th} measurements. As we can see from Figure 4-7, there is a good agreement between the experimental and the theoretical results. We have verified experimentally that performing epi-down mounting improves the thermal resistance by about 22 %.

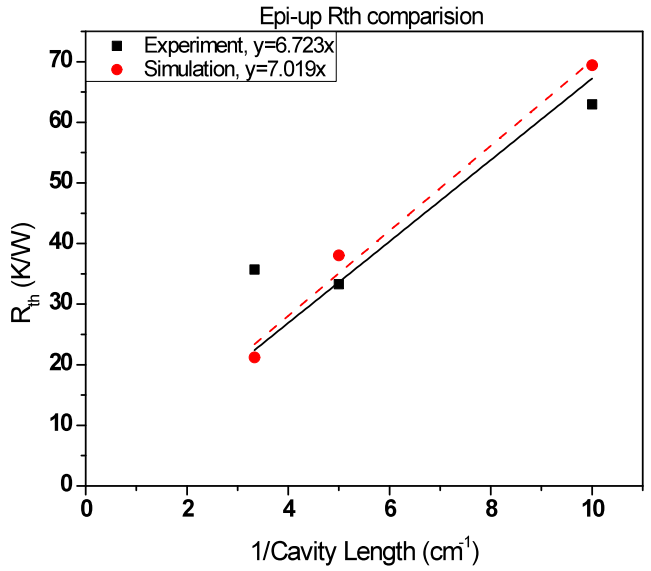

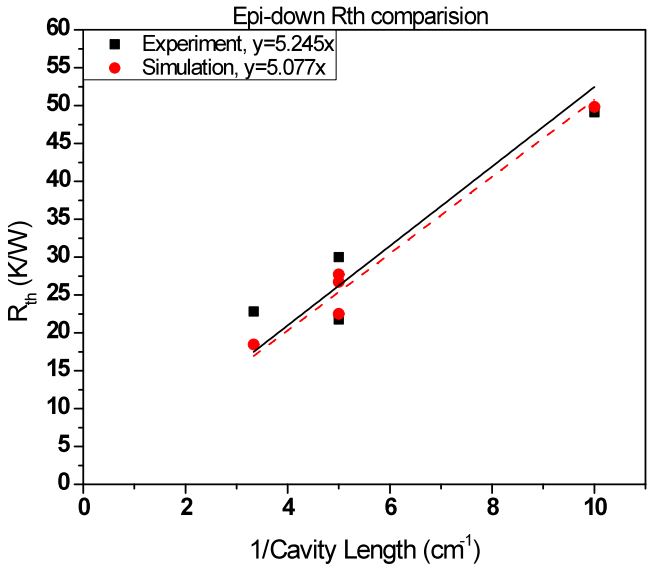

Figure 4-7 Epi-up and down R_{th} comparison Experiment vs. Simulation

Experimental R_{th} was measured by operating the same laser in pulsed and CW mode at different heat sink temperatures. The selected temperatures are such that both

operating modes have the same threshold current. This indicates that at a certain threshold current, we have the same active region temperature for both the pulsed and CW operation modes. For pulsed operation, we used 200 ns wide pulses and 1 kHz repetition rate pulses since previous results have shown that pulses wider than 200 ns and slower than 1 kHz can lead to heating of the active region. Also, our laser has the thermal relaxation time of 1us so with 200 ns pulse width with 1 kHz repetition rate we can assume that there is no heating in the active region. In CW mode, the way we estimate the active region temperature difference with the heat sink is by comparing the pulsed and CW active region temperatures that give the same threshold current. Figure 4-8 illustrates the experimental method.

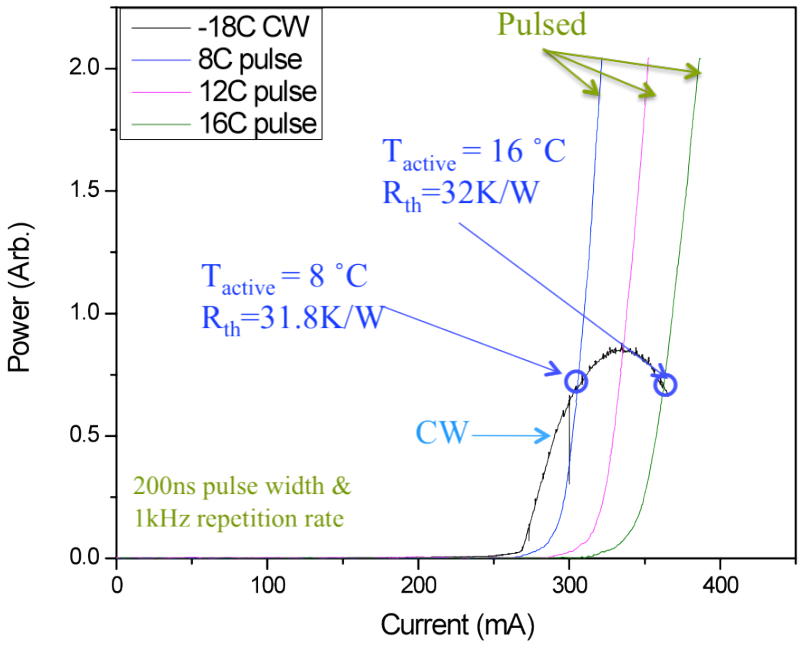

Figure 4-8 R_{th} experimental measurement method

Chapter 5: High Reflection and Anti-Reflection Coatings

In this chapter, we will discuss both high reflectivity (HR) and antireflection (AR) coatings. By coating IC lasers with high reflectivity coatings, we were able to decrease the threshold current density and increase the slope efficiency. In addition, antireflection coatings also helps us to improve the slope efficiency even more. In this section, we are going to describe the physics behind anti-reflection coatings by studying transmission and reflection of single and multi-layers [47]. Then we will look at how we can design single and double layer AR coating for IC lasers

For HR coating, we use $Ta_2O_5/SiO_2/Al/Ta_2O_5/SiO_2$ films and for AR coating we use ZnS/SiO_2 films.

5.1 High Reflection Coating

In order to achieve higher output power from IC lasers, we have concentrated our efforts on developing IC lasers with high reflectivity (HR) coatings. Figure 5-1 shows the uncoated and HR coated IC laser cavity. When there is no coating on the facets, light will be emitted from both facets. However, when we deposit HR coating on one facet, light will only come out from the uncoated facet.

For HR coating we first deposit a dielectric layer Ta_2O_5 for electrical isolation. This layer prevents any shorting path between top and bottom metal. Second, we deposit a reflective metal, aluminum or gold. Both gold and aluminum

have very high reflection coefficient in the mid-infrared region but aluminum has a much higher refractive index at mid-infrared. Finally, we deposit another dielectric layer of Ta_2O_5. The last dielectric layer prevents the wetting of metal when we mount IC laser epi-side down with soft indium solder.

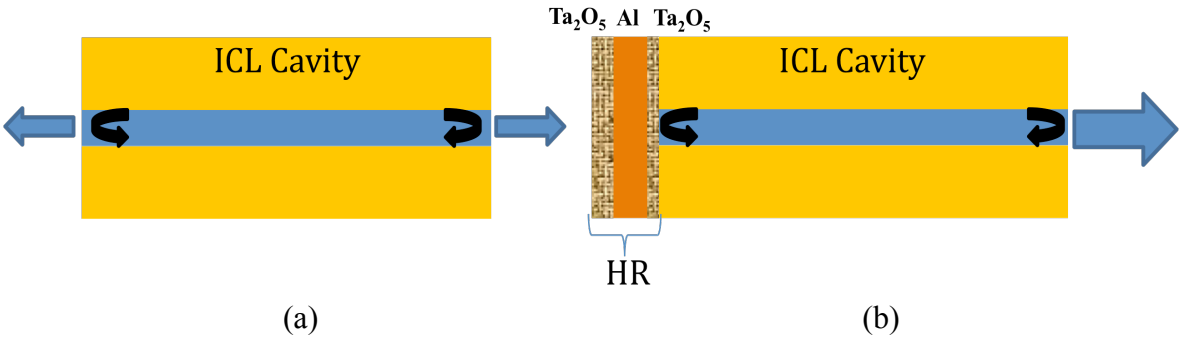

Figure 5-1. (a) uncoated IC laser cavity, (b) HR coated IC laser cavity

There are two main advantages of depositing a high reflectivity coating. One is reducing the threshold current density so that we can operate the laser at higher temperatures and the other is increasing the slope efficiency so that we can get higher output power. Higher slope efficiency can be easily realized as can be seen from Equations (5-1) to (5-3).

$$\eta_{s,uncoated} = \frac{1}{2}\eta_i\left(\frac{a_m}{a_i + a_m}\right) \Rightarrow \eta_{s,coated} = \frac{1}{(1+1/\beta)}\eta_i\left(\frac{a_m}{a_i + a_m}\right) \tag{5-1}$$

$$\beta = \frac{1 - R_{front}}{1 - R_{rear}}\sqrt{\frac{R_{rear}}{R_{front}}} \tag{5-2}$$

$$a_m = \frac{1}{2L}\ln\left(\frac{1}{R_{rear}R_{front}}\right) \tag{5-3}$$

where, β takes into account the unequal power distribution from asymmetry in facet reflectance, a_i is the internal loss of the laser waveguide determined

experimentally, a_m is the overall mirror loss, L is the length of the cavity and η_i is the internal efficiency, and R_{rear} and R_{front} are the reflectances of the rear and front facet, respectively.

Also, the mirror loss change leads to a change in threshold current density J_{th} which can be seen from Equation 2-18.

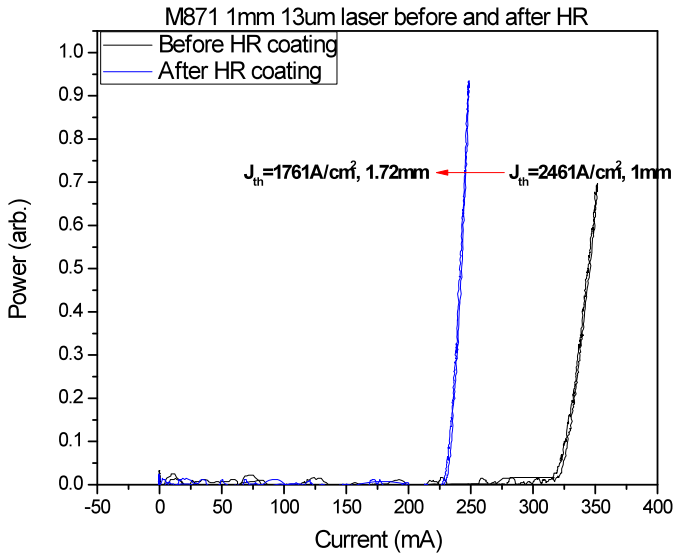

Figure 5-2. M871 IC laser before and after HR

Figure 5-2 shows an example of our HR coating performance. Before HR coating the threshold current density was 2461A/cm^2 and after HR coating, the threshold current density became 1761A/cm^2, this represents a 30% reduction. Also, after HR coating, the slope efficiency was increased by 150%. We believe that we might improve the slope efficiency further by depositing metal directly on the facet since light directly re-couples back into the waveguide after the reflected from metal. Figure 5-3 shows the schematic of the silicon mount that we made for direct metal

deposition. Using deep reactive ion etching (DRIE), we have etched about 50um of the silicon sample to create a covered area. The IC laser is then placed against the etched area. It allows us to block only the lower part of the laser that prevents any shorting path between the top and bottom metal contacts.

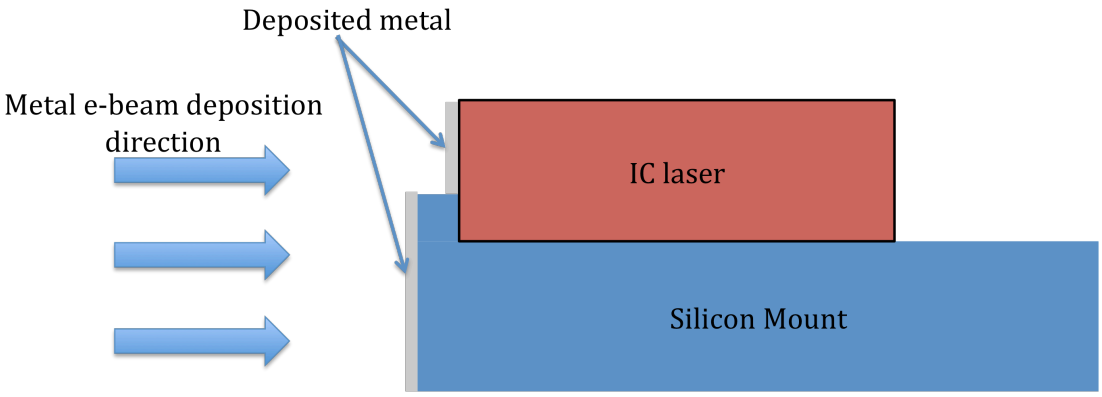

Figure 5-3 Directed HR coating schematic

5.2 Anti-Reflection Coating

5.2.1 Plane wave reflection

The plane wave reflection of an optical beam incident on a smooth interface is what we all learned in an undergraduate electromagnetic class. When we consider a plane wave incident from medium 0 onto the smooth medium 1 with an incident angle θ_0 and refraction angle θ_1 as shown in Figure 6-4, the reflection coefficient is given by the Fresnel's formulas

$$r_{TE} = \frac{n_0 \cos\theta_0 - n_1 \cos\theta_1}{n_0 \cos\theta_0 + n_1 \cos\theta_1}, \text{ TE polarization} \qquad (5\text{-}5)$$

$$r_{TM} = \frac{n_1 \cos\theta_0 - n_0 \cos\theta_1}{n_1 \cos\theta_0 + n_0 \cos\theta_1}, \text{ TM polarization} \qquad (5\text{-}6)$$

where n_0 and n_1 are the refractive indices of medium 0 and 1, respectively.

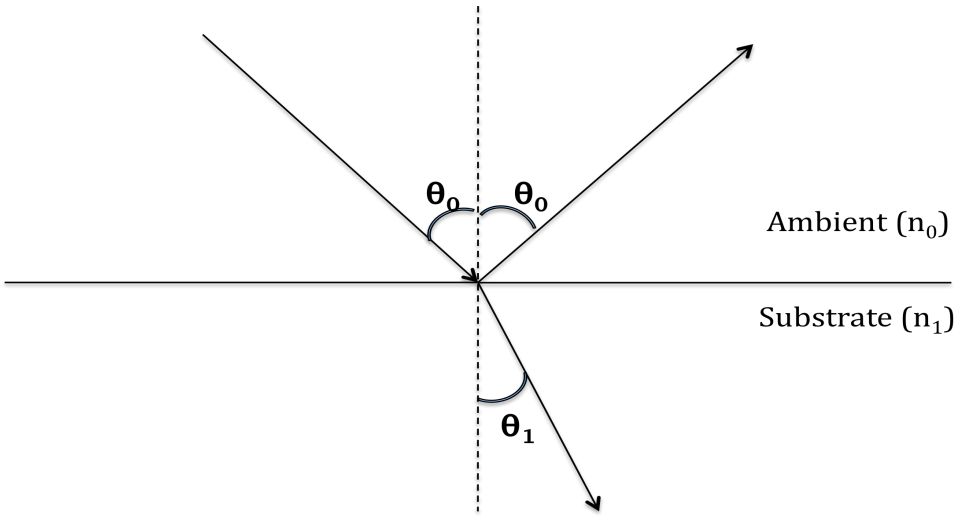

Figure 5-4 Reflection of a plane wave at the interface of two media

TE polarization is when the electric field is perpendicular to the plane of incidence and TM polarization is realized when the electric field is parallel to the plane of incidence. Also from Snell's law we can write

$$n_0 \sin\theta_0 = n_1 \sin\theta_1 \qquad (5\text{-}7)$$

If we have a dielectric film on the surface of a substrate, there are multiple reflections. One comes from the interface between the ambient and the film and the other comes from the interface between the film and the substrate. This is shown in Figure 5-5. Since there are multiple reflections from the two interfaces, the total reflected wave is the sum of the waves that are reflected at the interface between medium 0 and medium 1 and the reflections from the surface between the medium 1

and medium 2. The total reflection coefficient can be calculated by summing up all reflected waves,

$$r_X = \frac{r_{01X} + r_{12X} e^{(-j2\phi_1)}}{1 + r_{01X} r_{12X} e^{(-j2\phi_1)}}, X = TE, TM \tag{5-8}$$

where r is the Fresnel's reflection coefficient of the TE and TM polarized waves, ϕ_1 is the phase difference between the two reflections and it is given by

$$\phi_1 = 2\pi n_1 d_1 \cos\theta_1 / \lambda_0 \quad , \tag{5-9}$$

where λ_0 is the wavelength in the vacuum, n_1 is the index of refraction, d_1 is the thickness, and θ_1 is the refraction angle.

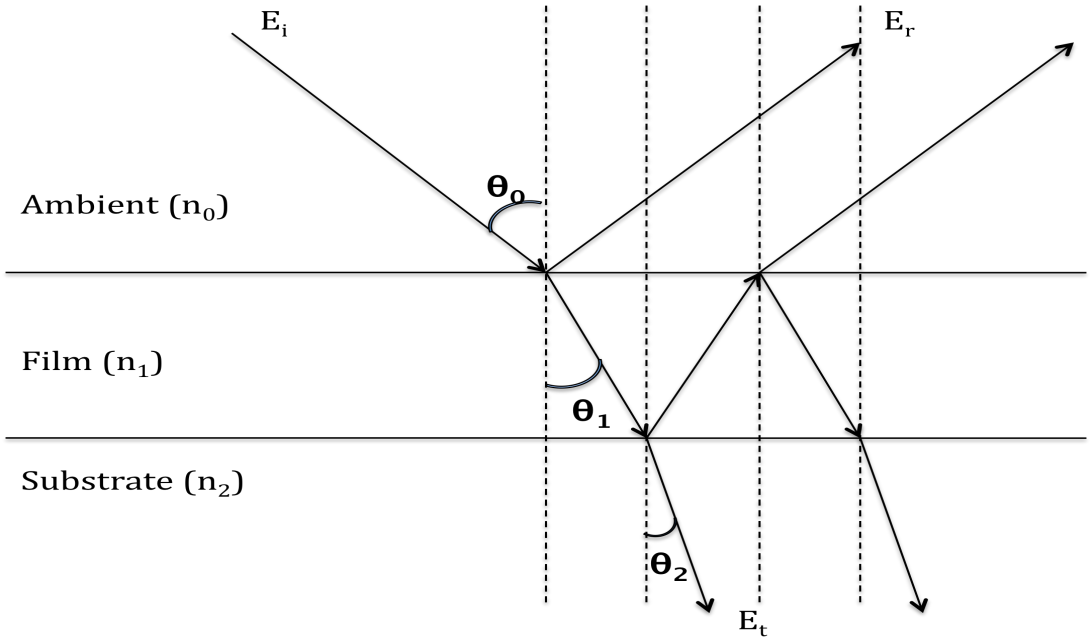

Figure 5-5 Multiple reflections of a plane wave at a single layer film interface

For multi-layer films, we can derive the reflection coefficient from Equation 5-8. Let us say that we have N-layers of thin films on the substrate. We can subdivide the films by considering the film 1 as material 1 and the rest of the films as material

2. When r_{1NX} is the overall reflection coefficient of TE/TM wave for material 2 observed in film 1, we can rewrite the Equation 5-8 as

$$r_X = \frac{r_{01X} + r_{1NX} e^{(-j2\phi_1)}}{1 + r_{01X} r_{1NX} e^{(-j2\phi_1)}}, X = TE, TM \tag{5-10}$$

Equation 5-9 is a general equation for the reflection coefficient so we can calculate the reflection coefficient in medium 0 from a single layer to multi-layer.

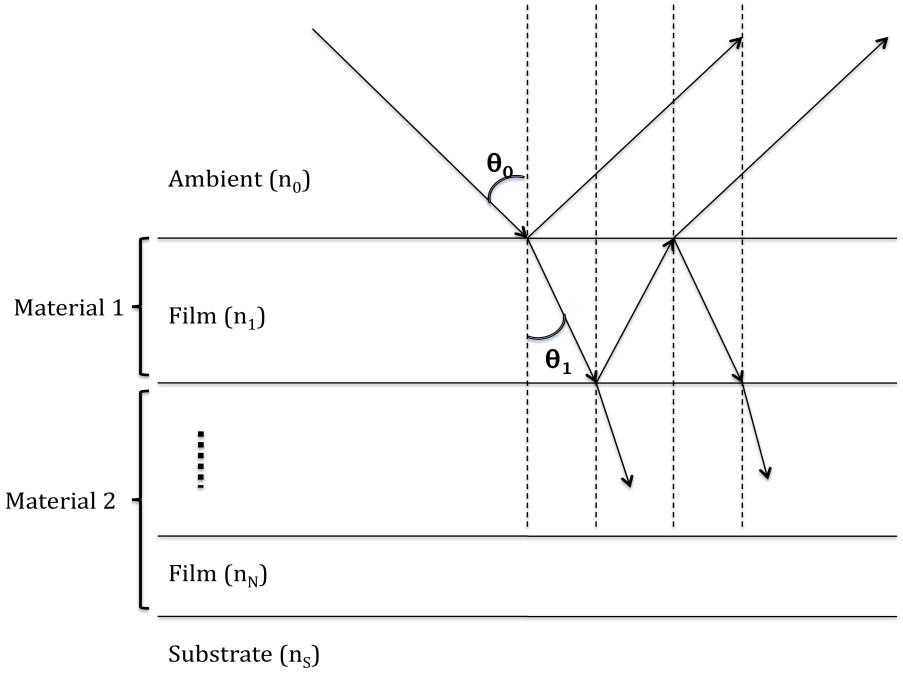

Figure 5-6 Multiple reflections of a plane wave at a multi-layer film interface

5.2.2 Plane electromagnetic wave at a dielectric medium interface

Let us write the magnitude of the electric field of incident, reflected, and transmitted waves at the interface between medium 0 and medium 1 as shown in Figure 5-7.

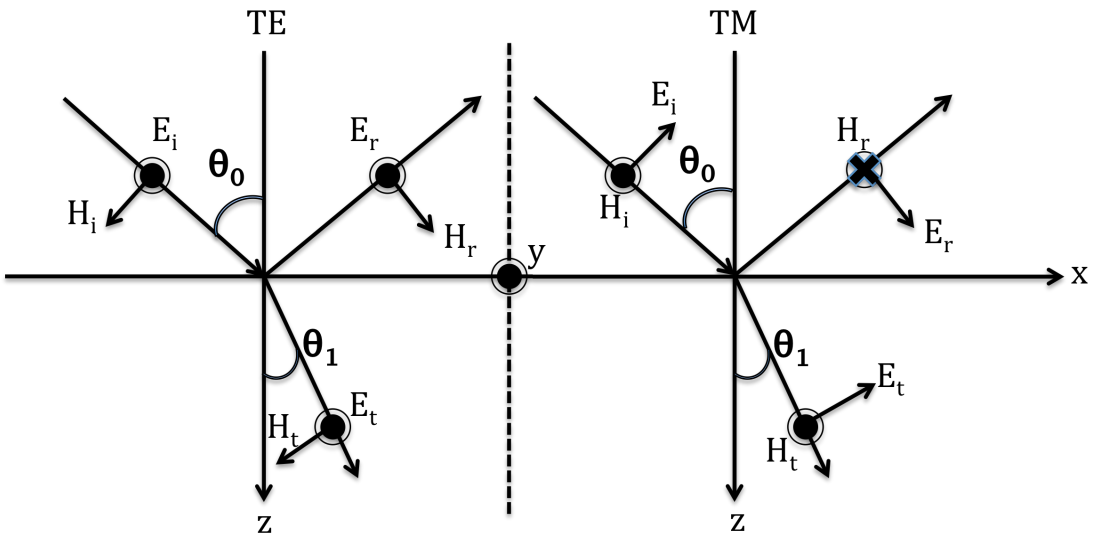

Figure 5-7 Incident, reflection and transmission (TE & TM) at the surface

$$\begin{aligned} &E_t e^{-i\vec{k}_i\vec{r}+iwt} \\ &E_r e^{-i\vec{k}_r\vec{r}+iwt} \\ &E_t e^{-i\vec{k}_t\vec{r}+iwt} \end{aligned} \tag{5-11}$$

From Equation 5-11, we can define the reflection and transmission coefficients as

$$\begin{aligned} r &= \frac{E_r}{E_i} \\ t &= \frac{E_t}{E_i} \end{aligned} \tag{5-12}$$

We can also define the reflectance and transmittance as the ratio of the energy reflected and transmitted from the incident wave at the surface.

$$\begin{aligned} R &= \frac{\mathrm{Re}(-\vec{S}_r\cdot\hat{n})}{\mathrm{Re}(\vec{S}_i\cdot\hat{n})} = \frac{|E_r|^2}{|E_i|^2} = |r|^2 \\ T &= \frac{\mathrm{Re}(\vec{S}_t\cdot\hat{n})}{\mathrm{Re}(\vec{S}_i\cdot\hat{n})} = \frac{|E_t|^2\,\mathrm{Re}(k_{tz})}{|E_i|^2\,\mathrm{Re}(k_{iz})} = |t|^2\frac{\mathrm{Re}(k_{tz})}{\mathrm{Re}(k_{iz})} \end{aligned} \tag{5-13}$$

where $\hat{n}$ is the unit vector perpendicular to the interface, and k_z is the vertical part of the wave vector.

To obtain the reflectance and transmittance from Equation 5-13, the system must satisfy the boundary condition requirement. Assuming that we have a perfect dielectric, all components of electric and magnetic field parallel to the interface should be continuous. If we define a vector consisting of two components, $\begin{pmatrix} \vec{E}_{//} \\ \vec{H}_{//} \end{pmatrix}$, then the boundary condition can be expressed as

$$\begin{pmatrix} \vec{E}_{//} \\ \vec{H}_{//} \end{pmatrix}_0 = \begin{pmatrix} \vec{E}_{//} \\ \vec{H}_{//} \end{pmatrix}_1 \tag{5-14}$$

Now, let us look at the two different polarizations.

- TE polarization

From Figure 5-7, we can write the relationship between the incident (E_+) and the reflected electric field (E_-) for TE polarization as

$$\vec{E}_{//} = (E_+ + E_-)\hat{y} \tag{5-15}$$

$$\vec{H}_{//} = \frac{1}{w\mu} k_z (E_- - E_+)\hat{x} \tag{5-16}$$

Equations 5-15 and 5-16 are general equations for the incident wave and the reflected wave at any interface. For example, in medium 0, E_+ is the incident wave and E_- is the reflected wave while in medium 1, E_+ is the refracted wave and E_- is zero for a single layer medium.

Now we can define a matrix Q_s

$$Q_s = \begin{pmatrix} 1 & 1 \\ -\frac{k_z}{c\mu k_0} & -\frac{k_z}{c\mu k_0} \end{pmatrix} \tag{5-17}$$

Equations (5-15) and (5-16) can be expressed as

$$\begin{pmatrix} E_{//} \\ H_{//} \end{pmatrix} = Q_s \begin{pmatrix} E_+ \\ E_- \end{pmatrix} \tag{5-18}$$

From the boundary condition we can write

$$Q_{s0} \begin{pmatrix} E_i \\ E_r \end{pmatrix} = Q_{s1} \begin{pmatrix} E_t \\ 0 \end{pmatrix} \tag{5-19}$$

Also we can rewrite Equation (5-19) as

$$\begin{pmatrix} E_i \\ E_r \end{pmatrix} = N \begin{pmatrix} E_t \\ 0 \end{pmatrix} \tag{5-20}$$

where $N = {Q_{s0}}^{-1} Q_{s1} = \begin{pmatrix} N_{11} & N_{12} \\ N_{21} & N_{22} \end{pmatrix}$

We can assume μ=1 and derive the reflection and transmission coefficients as

$$\begin{aligned} r_s &= \frac{E_r}{E_i} = \frac{N_{21}}{N_{11}} = \frac{k_{z0} - k_{z1}}{k_{z0} + k_{z1}} = \frac{n_0 \cos\theta_0 - n_1 \cos\theta_1}{n_0 \cos\theta_0 + n_1 \cos\theta_1} \\ t_s &= \frac{E_t}{E_i} = \frac{1}{N_{11}} = \frac{2k_{z0}}{k_{z0} + k_{z1}} = \frac{2n_0 \cos\theta_0}{n_0 \cos\theta_0 + n_1 \cos\theta_1} \end{aligned} \tag{5-21}$$

- TM polarization

For TM polarization, from Figure 5-7, we can similarly write the relationship between the incident (H_+) and the reflected magnetic field (H_-).

$$\vec{H}_{//} = (H_+ - H_-)\hat{y} \tag{5-22}$$

$$\vec{E}_{//} = \frac{c^2 \mu}{n^2 w} k_z (H_+ + H_-)\hat{x} \tag{5-23}$$

Now we can define a matrix Q_p

$$Q_p = \begin{pmatrix} \frac{c\mu k_z}{n^2 k_0} & \frac{c\mu k_z}{n^2 k_0} \\ 1 & -1 \end{pmatrix} \tag{5-24}$$

Equations (5-22) and (5-23) can be expressed as

$$\begin{pmatrix} E_{//} \\ H_{//} \end{pmatrix} = Q_p \begin{pmatrix} H_+ \\ H_- \end{pmatrix} \tag{5-25}$$

From the boundary condition we can write

$$Q_{p0} \begin{pmatrix} H_i \\ H_r \end{pmatrix} = Q_{p1} \begin{pmatrix} H_t \\ 0 \end{pmatrix} \tag{5-26}$$

Also we can rewrite Equation (5-26) as

$$\begin{pmatrix} H_i \\ H_r \end{pmatrix} = N' \begin{pmatrix} H_t \\ 0 \end{pmatrix} \tag{5-27}$$

where $N' = {Q_{p0}}^{-1} Q_{p1} = \begin{pmatrix} N'_{11} & N'_{12} \\ N'_{21} & N'_{22} \end{pmatrix}$

We can assume μ=1 and derive the reflection and transmission coefficients as

$$\begin{aligned} r_p &= \frac{E_r}{E_i} = \frac{N'_{21}}{N'_{11}} = \frac{{n_0}^2 k_{z1} - {n_1}^2 k_{z0}}{{n_0}^2 k_{z1} + {n_1}^2 k_{z0}} = \frac{n_0 \cos\theta_1 - n_1 \cos\theta_0}{n_1 \cos\theta_0 + n_0 \cos\theta_1} \\ t_p &= \frac{E_t}{E_i} = \frac{n_0}{n_1}\frac{H_t}{H_i} = \frac{n_0}{n_1}\frac{1}{N_{11}} = \frac{2n_0 n_1 k_{z0}}{{n_1}^2 k_{z0} + {n_0}^2 k_{z1}} = \frac{2n_0 \cos\theta_0}{n_0 \cos\theta_0 + n_1 \cos\theta_1} \end{aligned} \tag{5-28}$$

5.2.3 Electromagnetic fields in a thin film

Now, we can look at the electromagnetic fields in a thin film coating as shown in Figure 5-5. There is a single layer coating (n_1) between medium 0 (n_0) and 2 (n_2). Assuming that the inside of the coating the wave propagates along both x and z directions, then parallel components of electromagnetic field can be written as

$$E_{//}(x,z,t) = [A\sin(k_z z) + B\cos(k_z z)]e^{-ik_x x + iwt}$$
$$H_{//}(x,z,t) = [C\sin(k_z z) + D\cos(k_z z)]e^{-ik_x x + iwt} \tag{5-29}$$

For TE polarization, from Maxwell's equations, we can write

$$\nabla \times \vec{E} = -\mu \frac{\partial}{\partial t}\vec{H} \Rightarrow -i\frac{\partial E_{//}}{\partial z} + k\frac{\partial E_{//}}{\partial x} = -i\mu\omega(iH_{//} + kH_{\perp}) \tag{5-30}$$

$$\frac{\partial E_{//}}{\partial z} = i\mu\omega H_{//} \tag{5-31}$$

From Equations (5-29) and (5-31) with boundary conditions, we can solve for A,B,C, and D.

$$\left.\frac{\partial E_{//}}{\partial z}\right|_{z=0} = Ak_z = i\mu\omega H_{//}(0) \Rightarrow A = \frac{ic\mu k_0}{k_z}H_{//}(0)$$
$$\frac{\partial^2 E_{//}}{\partial z^2} = i\mu\omega\frac{\partial H_{//}}{\partial z} \Rightarrow -k_z^2 E_{//}(0) = i\mu\omega k_z C \Rightarrow C = \frac{ik_z}{c\mu k_0}E_{//}(0) \tag{5-32}$$
$$B = E_{//}(0)$$
$$D = H_{//}(0)$$

Now we can rewrite the solution for the parallel component of electromagnetic field in matrix format.

$$\begin{pmatrix} E_{//}(z) \\ H_{//}(z) \end{pmatrix} = \begin{pmatrix} \cos k_z z & \frac{ic\mu k_0}{k_z} \\ \frac{ik_z}{c\mu k_0} & \cos k_z z \end{pmatrix}\begin{pmatrix} E_{//}(0) \\ H_{//}(0) \end{pmatrix} = M^{-1}\begin{pmatrix} E_{//}(0) \\ H_{//}(0) \end{pmatrix}$$
$$\begin{pmatrix} E_{//}(0) \\ H_{//}(0) \end{pmatrix} = \begin{pmatrix} \cos k_z z & -\frac{ik_z}{c\mu k_0} \\ -\frac{ic\mu k_0}{k_z} & \cos k_z z \end{pmatrix}\begin{pmatrix} E_{//}(z) \\ H_{//}(z) \end{pmatrix} = M\begin{pmatrix} E_{//}(z) \\ H_{//}(z) \end{pmatrix} \tag{5-33}$$

For TM polarization, similarly we can get A,B,C, and D.

$$\begin{pmatrix} E_{//}(z) \\ H_{//}(z) \end{pmatrix} = \begin{pmatrix} \cos(k_z z) & -\frac{ic\mu k_z}{n^2 k_0}\sin(k_z z) \\ -\frac{in^2 k_0}{c\mu k_z}\sin(k_z z) & \cos(k_z z) \end{pmatrix} \begin{pmatrix} E_{//}(0) \\ H_{//}(0) \end{pmatrix} = M^{-1} \begin{pmatrix} E_{//}(0) \\ H_{//}(0) \end{pmatrix}$$
$$\begin{pmatrix} E_{//}(0) \\ H_{//}(0) \end{pmatrix} = \begin{pmatrix} \cos(k_z z) & \frac{ic\mu k_z}{n^2 k_0}\sin(k_z z) \\ \frac{in^2 k_0}{c\mu k_z}\sin(k_z z) & \cos(k_z z) \end{pmatrix} \begin{pmatrix} E_{//}(z) \\ H_{//}(z) \end{pmatrix} = M \begin{pmatrix} E_{//}(z) \\ H_{//}(z) \end{pmatrix} \quad (5\text{-}34)$$

5.2.4 Reflection and transmission at a multilayer surface

From the results we have obtained in previous sections, we can now solve for the reflection and transmission of a multilayer coated surface as shown in Figure 5-6. The effect of each layer can be represented by the matrix in Equations (5-33) and (5-34) by taking the thickness of the layer as the value z. Combining the matrix Q and the matrix M, now we can define the matrix N as

$$N = Q_a^{-1} M Q_s = \begin{pmatrix} N_{11} & N_{12} \\ N_{21} & N_{22} \end{pmatrix} \quad (5\text{-}35)$$

where a stands for ambient and s stands for the substrate.

We can then obtain the reflection and transmission coefficients

$$t_s = \frac{1}{N_{11}} = \frac{2k_{za}}{k_{za}M_{11} + k_{zs}M_{22} - \frac{k_{zs}k_{za}}{k_0}M_{12} - k_0 M_{21}}$$
$$r_s = \frac{N_{21}}{N_{11}} = \frac{k_{za}M_{11} - k_{zs}M_{22} - \frac{k_{zs}k_{za}}{k_0}M_{12} + k_0 M_{21}}{k_{za}M_{11} + k_{zs}M_{22} - \frac{k_{zs}k_{za}}{k_0}M_{12} - k_0 M_{21}} \quad , \text{ TE polarization} \quad (5\text{-}36)$$

$$t_p = \frac{n_a}{n_s}\frac{1}{N_{11}} = \frac{2n_s n_a k_{za}}{n_a^2 k_{zs} M_{11} + n_s^2 k_{za} M_{22} + n_a^2 n_s^2 k_0 M_{12} + \frac{k_{zs}k_{za}}{k_0} M_{21}}$$

$$r_s = \frac{N_{21}}{N_{11}} = \frac{n_a^2 k_{zs} M_{11} - n_s^2 k_{za} M_{22} + n_a^2 n_s^2 k_0 M_{12} - \frac{k_{zs}k_{za}}{k_0} M_{21}}{n_a^2 k_{zs} M_{11} + n_s^2 k_{za} M_{22} + n_a^2 n_s^2 k_0 M_{12} + \frac{k_{zs}k_{za}}{k_0} M_{21}} \quad \text{, TM polarization} \tag{5-37}$$

Here we can define the q factor for each layer.

$$\begin{aligned} q_j &= n_j \cos\gamma_j \text{ for TE} \\ q_j &= n_j / \cos\gamma_j \text{ for TM} \end{aligned} \tag{5-38}$$

where n_j is the refractive index of each layer and γ_j is the propagation angle in each layer. Using Equation 6-38, we can now write the characteristic matrix in general format.

$$M_j = \begin{pmatrix} \cos\varphi_j & (i/q_j)\sin\varphi_j \\ iq_j \sin\varphi_j & \cos\varphi_j \end{pmatrix} \tag{5-39}$$

where $\varphi_j = k_z d_j$ and d_j is the thickness of the layer j.

5.2.5 Antireflection coating design

Up to this point, we assume that the incident wave on the layer was a plane wave. For many coating application this can be true however, when we consider a semiconductor laser we can not assume that the incident wave is a plane wave since the diffraction is a major issue and it has to be considered in the calculation. The beam emitted from the laser diverges according to Gaussian optics.

$$\vartheta_0 = \frac{2}{\pi}\frac{\lambda}{2W_0} \tag{5-40}$$

where $2W_0$ is the spot size of the bean at the interface, λ is the wavelength, and ϑ_0 is the divergence cone half angle. In order to calculate the facet reflectivity of the

semiconductor laser, we have to break down the mode into a sum of many different plane waves, called plane wave decomposition and minimizing the overall reflection from all the reflected waves incident on the laser facet at different angles [48-50].

Now let us start with a single layer antireflection coating. When we deposit the semiconductor laser with a single dielectric layer, there will be reflections from the dielectric layer and the substrate layer. In order to make the deposited film work as an antireflection coating, we have to make sure that the interference between the two reflections are destructive. Making the interference to be destructive can be achieved if two reflected beams have the phase difference of π and have the same magnitude. For normal incidence, we can get the phase difference of π if the film thickness is a quarter wavelength. Also, from the Fresnel's law we get

$$\frac{n_1 - n_0}{n_1 + n_0} = \frac{n_2 - n_1}{n_2 + n_1} \Rightarrow n_1 = \sqrt{n_0 n_2} \tag{5-41}$$

For oblique incidence the reflection is

$$r = \frac{(n_1 - n_2)^2 \cos^2 \varphi_1 + i(n_0 n_2 / n_1 - n_1)^2 \sin^2 \varphi_1}{(n_1 + n_2)^2 \cos^2 \varphi_1 + i(n_0 n_2 / n_1 + n_1)^2 \sin^2 \varphi_1} \tag{5-42}$$

As we can see from Equation 5-41 and 5-42, the reflection can be removed when $\cos\varphi_1$=0 and $n_1 = \sqrt{n_0 n_2}$. The condition $\cos\varphi_1 = 0$ also implies that the film thickness needs to be adjusted with the angle of incidence in such a way that $d = \frac{\lambda}{4\cos\theta}$, where λ is the wavelength of light in the layer, for the best single layer antireflection coating we need to have good control over the index of refraction and the film thickness. Since n_0 is 1 and n_2 is 3.5, n_1 needs to be 1.87. There is no film that has the index of refraction of 1.87, the closest one is Ta_2O_5 which has a index around 1.9. at λ=3.5um. Figure 5-8 shows the simulation results from IC laser which is single layer

antireflection coated with Ta_2O_5 film. This coating design is optimized for 3.45um wavelength. As we can see, the best facet reflectivity is only $5x10^{-3}$ due to the index difference with the required index of n_1=1.87.

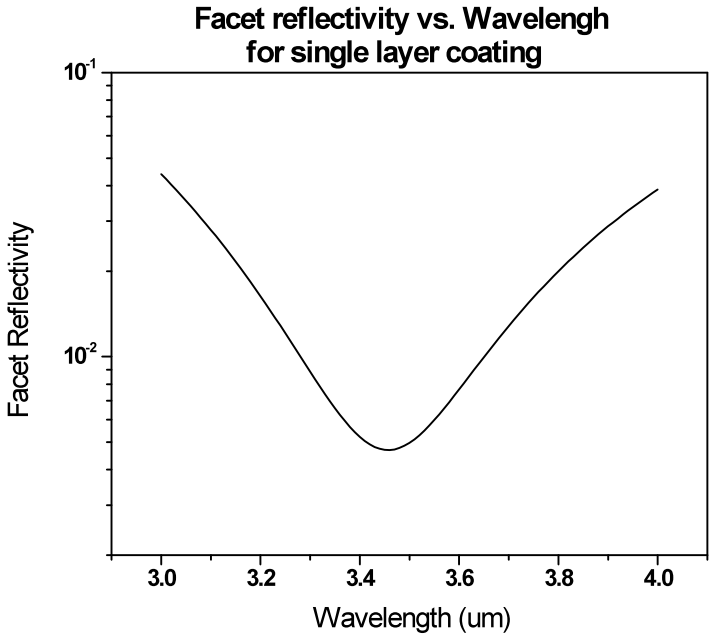

Figure 5-8 Single layer antireflection coating with Ta_2O_5 film optimized for 3.45um

For a double layer antireflection coating, we need to consider four index values (ambient, film1, film2, and the substrate) and two phase thicknesses for the two film layers (φ_1 and φ_2). From the matrices Q_a, Q_s, M_1, and M_2, we can find the zero reflectance condition when

$$\begin{cases} n_1 n_2 (n_s - n_0) + (n_0 n_2^2 - n_s n_1^2)\tan\varphi_1 \tan\varphi_2 = 0 \\ n_2 (n_1^2 - n_s n_0)\tan\varphi_1 + n_1 (n_2^2 - n_s n_0)\tan\varphi_2 = 0 \end{cases} \quad (5\text{-}43)$$

When we consider the ambient refractive index of 1, we can rewrite Equation 5-43 as

$$\begin{cases} \tan^2\varphi_1 = \dfrac{(n_s-1)(n_2^2-n_s)n_1^2}{(n_1^2n_s-n_2^2)(n_s-n_1^2)} \\ \tan^2\varphi_2 = \dfrac{(n_s-1)(n_s^2-n_1)n_2^2}{(n_1^2n_s-n_2^2)(n_2^2-n_s)} \end{cases} \tag{5-44}$$

From Equation 5-44, we can find the index requirements for two layer antireflection coating since the right hand side of the equations need to be positive. This implies that $(n_2^2-n_s),(n_1^2n_s-n_2^2),(n_s-n_1^2)$ should all be positive or only one of the three needs to be positive in order to meet the requirement. Figure 5-9 shows the simulation results for an IC laser with a double layers antireflection coating with ZnS (n_2=2.25 @3.5um) and SiO_2 (n_1=1.48 @3.5um) films. This coating design is optimized for 3.85um wavelength. As we can see, the best facet reflectivity is much lower than a single layer coating and theoretically we can achieve a facet reflectivity as low as $4x10^{-8}$. Using a double layers coating, previously we have obtained experimentally a coating reflectivity of $3.4x10^{-5}$. Figure 5-10 shows example of the threshold change of a laser before and after double layer coating.

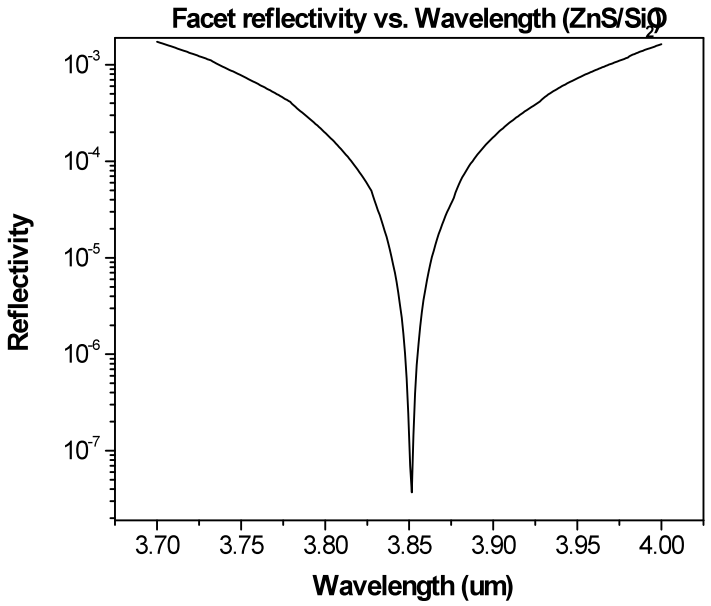

Figure 5-9 Simulation results of double layer coating (ZnS/SiO_2), facet reflectivity vs. wavelength

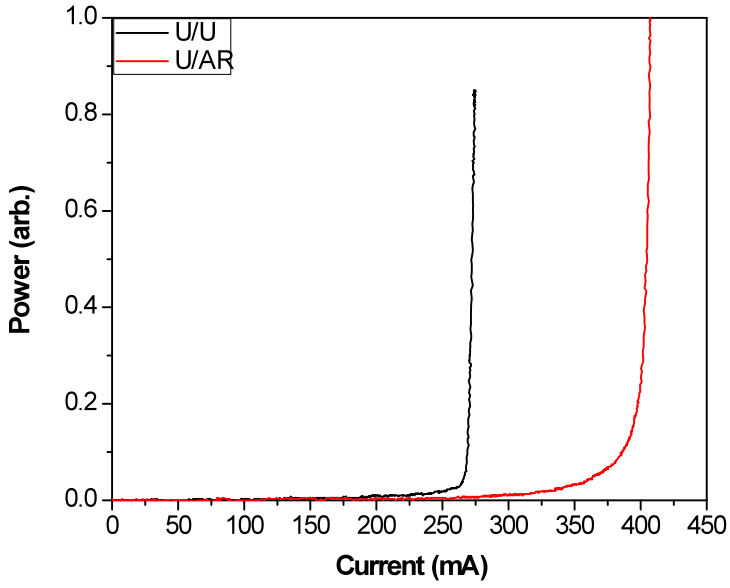

Figure 5-10 Example of the threshold change before and after a double layer coating is applied to a semiconductor laser facet

Chapter 6: Interband Cascade Laser Performance Improvements

In this chapter, we will talk about interband cascade laser performance improvements that we made during my Ph.D study. When we started the IC laser project, we could not operate our IC laser CW at room temperature. Now, we can operate our laser CW at room temperature. Also, we get the record low internal loss value in an interband cascade laser. This dramatic improvement did not just happen in one day. We have spent a lot of time to improve our fabrication steps and have studied various aspects of laser performance improvements including increasing the mode confinement in the active region using separate confinement regions, optimizing the lower cladding and ridge width to reduce the internal loss, reducing the dissipated power by reducing the number of cascades, reducing the free carrier absorption by adjusting the doping of each layer, and reducing the size of the injection region. With these improvements and facet coatings that we mentioned in previous chapter, now the maximum continuous wave mode output power is 62mW at room temperature and the internal loss is 4.8cm^{-1}. A detailed description of each improvement is discussed below.

6.1 Mode Confinement

At the beginning of IC laser project, our IC laser structure was very different from what we have now. For example, the structure only had the core and the

cladding region. There were two main problems with our previous structure. First, there was very poor light confinement in the active region since the difference of index of refraction between the core region and the cladding region was very small. Second, our core thickness was not thick enough to confine the light in the core region.

The solution to this light confinement problem was to introduce the separate confinement regions (SCR) between the core and the upper/lower cladding regions. This approach to increasing the light confinement in the active region was first proposed by Naval Research Lab. We used GaSb for our SCR material since it has higher index of refraction and it also has higher thermal conductivity. By using GaSb as the SCR material not only we can increase the light confinement but also we can improve our thermal performance. A detailed index profile of our IC laser structure is shown in Figure 6-1.

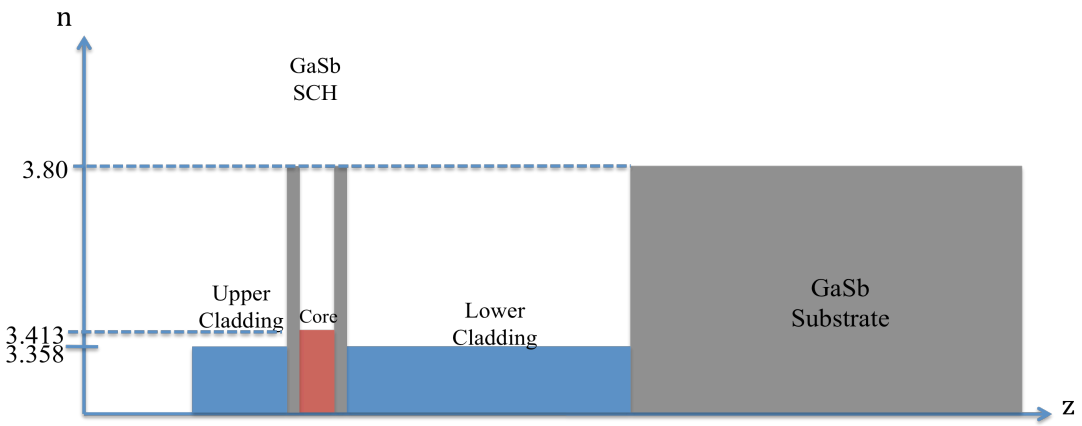

Figure 6-1. Index profile of IC laser

However, there is one disadvantage in using GaSb as a separate confinement region material. As we can see from Figure 6-1, GaSb materials have an index

refraction of 3.8 which is much higher than the core or the cladding region. So if we design our structure with too thick of a separate confinement region then light can leak out of the core region, and it can be confined in the separate confinement region instead. Figure 6-2 and 6-3 shows the mode within the SCH region. We can clearly see that there is small dip in the core area due to the index difference between the core and the SCR.

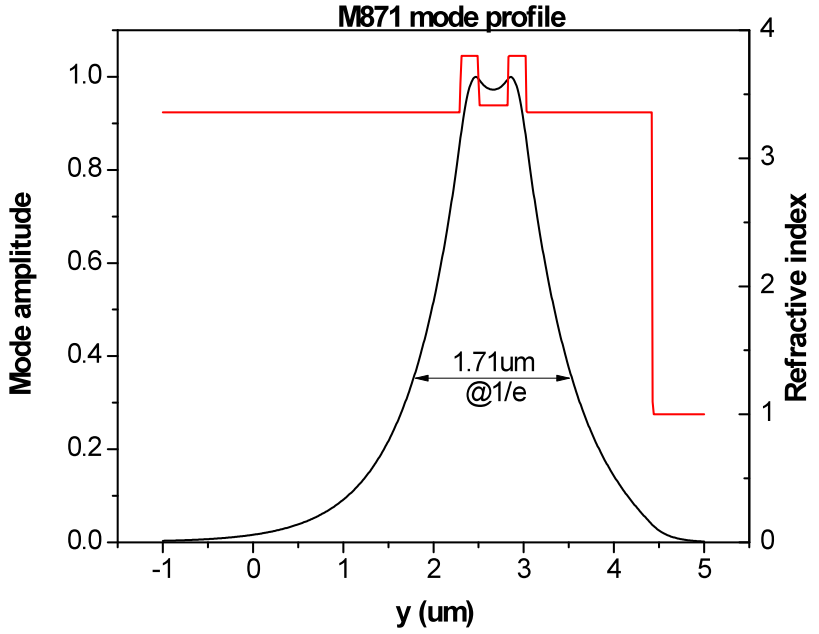

Figure 6-2. The mode profile with SCR

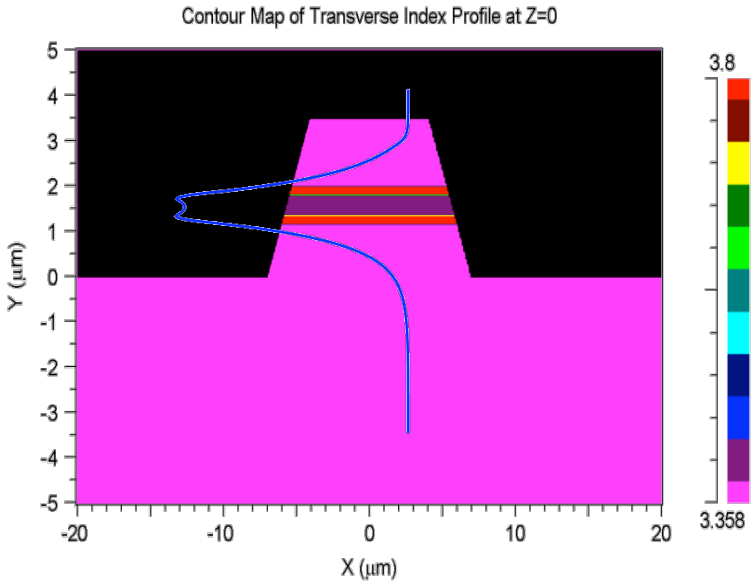

Figure 6-3. Transverse index profile and mode profile

In order to find the optimal separate confinement region thickness, we have performed a confinement factor simulation. The confinement factor Γ is defined by the ratio between the optical mode in the active region to the optical mode in all the regions.

$$\Gamma = \frac{\text{Optical mode in the active region}}{\text{Optical mode in all the regions}} = \frac{\int_{\text{Active region}} |E|^2 dy}{\int_{\text{All regions}} |E|^2 dy} \qquad (6\text{-}1)$$

where dy is the thickness of total layers that are used in the beam propagation simulation

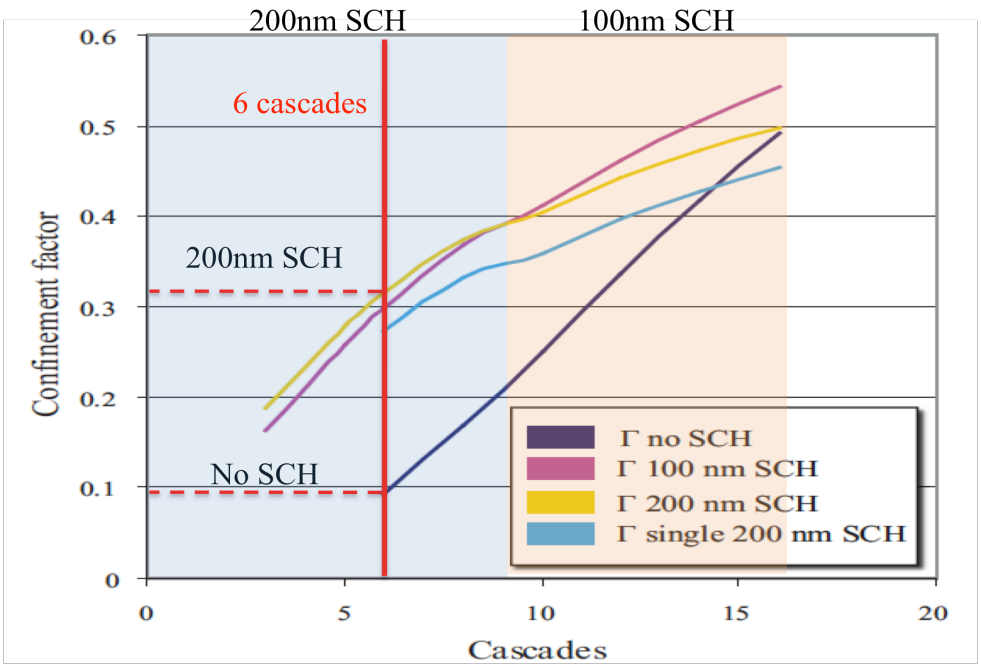

Figure 6-4. Confinement factor simulation result

The confinement factor simulation results are shown in Figure 6-4. It is very important to remember here that Γ is given by the ratio of the optical mode in the core region, including both the injection region and the active region, to the optical mode in all the regions. As we can see from Figure 6-4, there is a crossing point in a 9 cascade laser design between 200nm SCH and 100nm SCH. The reason for this crossing point is that when the number of cascades increases, the active region thickness also increases so that we do not need to have a thick separate confinement region to pull the mode from the cladding region. From various simulations and experiments, we have found that the optimal number of cascades is in fact a 5~6 cascade design. For a 6 cascade laser design, we need to have about 200nm of separate confinement region which gives more than a three times higher confinement factor than a no SCR laser design. Another reason for having less number of cascades

is to reduce the power dissipated in the structure allowing higher temperature cw operation of the laser.

6.2 Reduce Internal Loss

In addition to increasing the confinement factor, we have investigated ways to reduce the internal loss. We first tried to determine the optimal lower cladding thickness and ridge width. Figure 6-5 shows the detailed IC laser structure with simple mode profile. It is clear that we need to have the lower cladding since the substrate has very high index of refraction compared to the active region. Without the lower cladding region, all the light will leak out through the substrate.

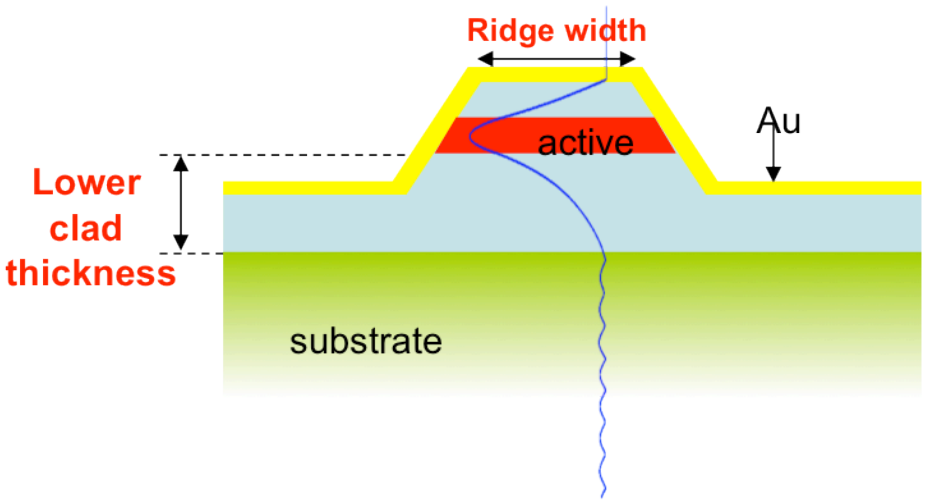

Figure 6-5 IC laser structure with simple mode profile

The simplest solution is just to put a thick lower cladding region. However, as we saw in the previous section, the lower cladding regions are InAs/AlSb supperlattice layers and it has very low thermal conductivity, so inserting a thick cladding region

degrades the thermal performance. In order to find the optimal thickness for the lower cladding region, we performed loss calculations and results are shown in Figure 6-6.

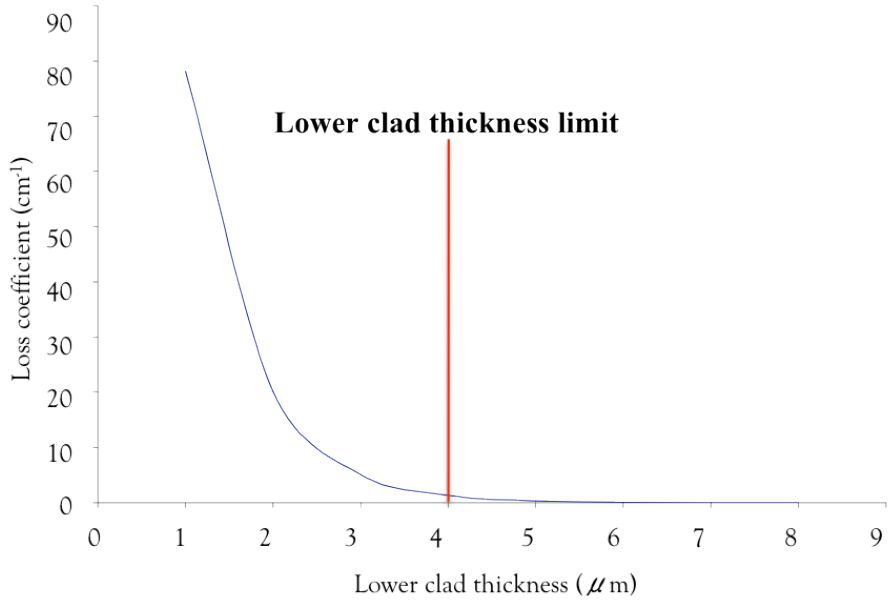

Figure 6-6 Loss coefficient vs. Lower cladding thickness

As we can see from Figure 6-6, we can reduce the loss when we increase the lower cladding thickness since the light does not reach to the substrate, but at the same time it reduces heat extraction capability from the active region. We have found that we need at least 4um of lower cladding to have low loss and reasonable thermal performance.

When light travels in the waveguide, it is also confined in the lateral direction within the ridge. If the ridge width is too narrow then most of the light is absorbed by the metal contact and the sidewall roughness becomes a serious issue due to the light scattering. On the other hand, if the ridge width is too wide then the heat generated in the active region needs to travel a longer distance to get extracted by the metal

contact. Wider ridge width thermal performance was discussed in the previous chapter. In order to find the optimal thickness for the lower cladding region, we have performed calculations, and results are shown in Figure 6-7.

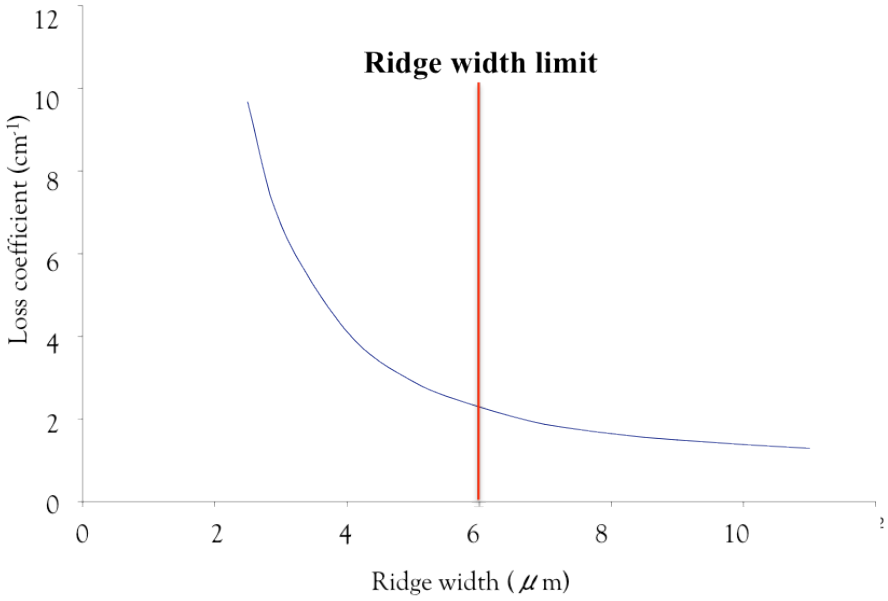

Figure 6-7 Loss coefficient vs. Ridge width

We have found that we need to fabricate IC lasers with ridges wider than 6um to have a reasonably lower loss coefficient. Most of time, we have fabricated 10um and 13um devices to have lower loss coefficients and to lower the scattering loss from the rough sidewall.

6.3 Other improvements and laser characterization

6.3.1 12 Cascades, p-doped separate confinement region ICLs

A 12-cascade IC laser was grown by MBE according to the structure that was described in the previous section. In this IC laser, the 200 nm thick separate confinement regions (SCRs) were p-doped at a concentration of 2.5 x $10^{17}cm^{-3}$. Ridge lasers of 10 um width were defined by contact lithography. A double trench structure was etched using a mixture of phosphoric acid, hydrogen peroxide, and tartaric acid. This structure maintains the planarity of the sample, allowing us to mount the device epi side down. We have stopped the etch process in the superlattice lower optical cladding, just below the separate confinement layer (SCL). We then have deposited a 400 nm thick Si_3N_4 dielectric layer using plasma enhanced chemical vapor deposition (PECVD). Ti/Pt/Au metal contacts were evaporated by e-beam evaporator. The laser devices were cleaved in different lengths between 0.5 and 3 mm long. Devices with uncoated facets were mounted epi-up on copper heat sinks soldered to a TE cooler.

In order to minimize thermal effects, low duty cycle (1 kHz) 200 ns current pulses were used to drive the lasers. By varying the pulse duration from 200 ns to several μs, we have observed that the slope efficiency of the lasers was very dependent on the pulse duration, in particular for lasers operated at room temperature. It was also observed that the threshold current density was less sensitive as compared to the slope efficiency when the pulse duration was varied. The emission wavelength of the lasers was around 3.5 um. Equations 2-18 and 2-19 describes the dependence of the threshold current density J_{th} on cavity length L_{cav} and the inverse of the slope efficiency 1/S versus L_{cav}:

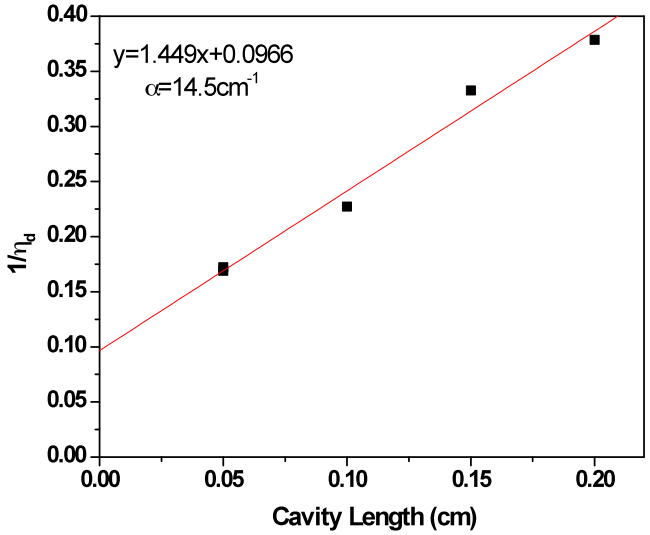

Figure 6-8 1/Differential efficiency vs. Cavity length measured at T = 240 K

A plane wave decomposition of the mode profile in the laser allowed us to extract the facet reflection coefficient to be R = 0.38. Figure 6-8 shows our measurement of the inverse of the slope efficiency of the laser versus the cavity length for four different laser lengths measured at T = 240 K. In these measurements, we made sure that pulse durations of about 200 ns did not lead to any measurable dependence of the slope efficiency by extending the pulse duration by a factor of 2 and observing no change to the slope efficiency.

From this measurement, we extracted the internal quantum efficiency per cascade of 1/(.0966 * N) = 0.86 at T=240K. From Equation 2-19, by taking the ratio of the slope to the intercept and multiplying the result by ln (1/R), we found that the internal loss is 14.5 cm^{-1}. For the same sample, we also measured the threshold current density versus $1/L_{cav}$ at 240 K. The results are shown in Figure 6-9.

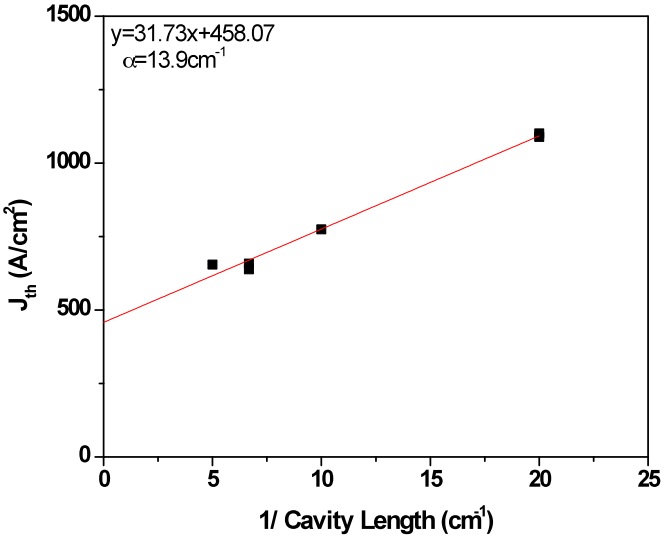

Figure 6-9 J_{th} vs. 1/Cavity length @ -33 °C for 12 cascade IC laser with p-doped SCR

Using Equation 2-18, dividing the ordinate by the slope and multiplying by ln(1/R), we extract that $n_t\Gamma\frac{dg}{dn}+\alpha_i=13.9cm^{-1}$. Comparing this result with the result obtained for the internal loss in the laser (14.5 cm^{-1}), we conclude that the transparency density term $n_t\Gamma\frac{dg}{dn}$ is much smaller than α_i so it can be neglected. This is consistent with observations from another research team [51] who measured n_t at lower temperatures and found this term to be small. We do not expect that the relative size of these two terms will change significantly with temperature. In addition, we believe that the confinement factor (as we will see) is smaller in our sample as compared to this other group, reducing even further the size of the n_t term. By neglecting this term, we find that the threshold current measurement approach gives us a very similar value of α_i. The advantage of measuring the internal loss using the threshold current is that this approach is much less sensitive to thermal effects as the

temperature of the sample is increased up to room temperature.

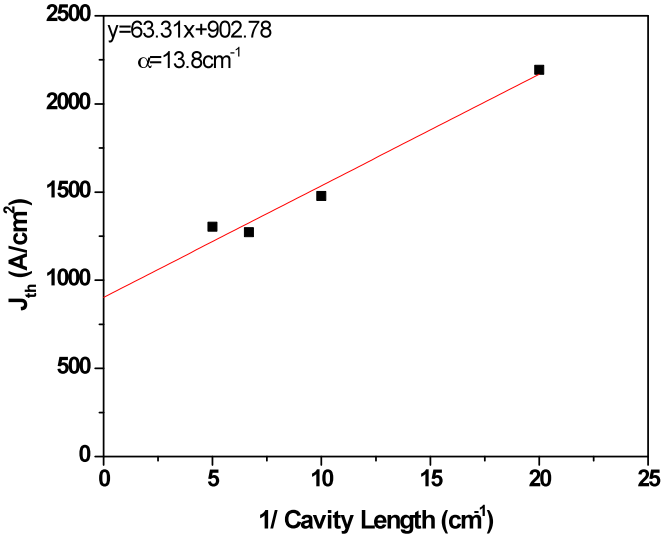

Figure 6-10 J_{th} vs. 1/Cavity length @ -0.4 °C for 12 cascade IC laser with p-doped SCR

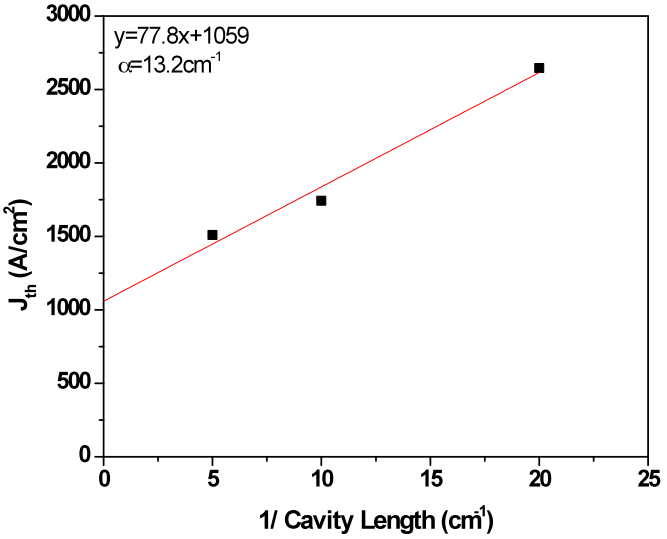

Figure 6-11 J_{th} vs. 1/Cavity length @ 7.7 °C for 12 cascade IC laser with p-doped SCR

Figures 6-10 and 6-11 show plots of J_{th} vs $1/L_{cav}$ at T = 273.7 and T = 281 K. Neglecting the n_t term, we extract that the internal loss in the laser at T = 273.7 and T = 281 K as 13.8 cm^{-1} and 13.2 cm^{-1} respectively. Comparing these results to the T = 240 K results, we conclude that the internal loss coefficient is mostly temperature independent over the temperature range that was studied. These results are in sharp contrast to previous results [51-53] which indicated a strong temperature dependence of the absorption coefficient over the same temperature range. These other reported results were obtained using slope efficiency measurements and longer pulses, which are more susceptible to temperature effects and therefore less reliable. From Equation 2-18 we can extract the gain per unit current density at threshold, $G_J = \frac{1}{q}\eta_i \tau \Gamma \frac{dG}{dN}$, by taking the inverse of the measured slope of J_{th} vs $1/L_{cav}$ and multiplying by 1/ln(R).

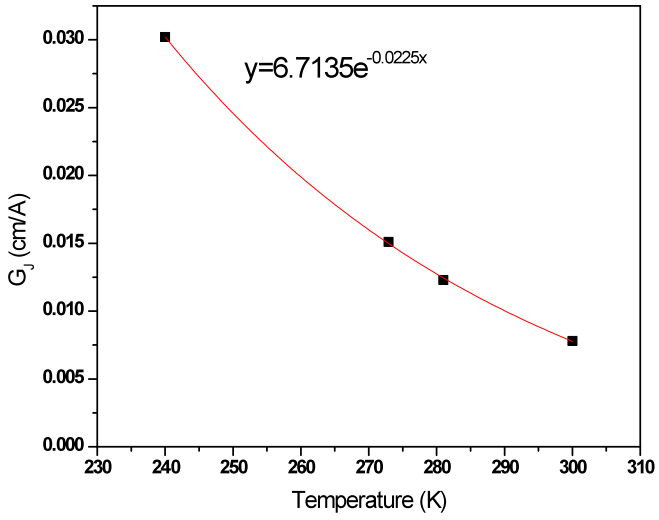

Figure 6-12 Gain per unit current density vs. Temperature for 12 cascade IC laser with p-doped

In Figure 6-12, we plotted the gain per unit current density at threshold as a function of temperature. We extract a characteristic temperature of T_0 = 45 ˚C and a gain per unit current density at threshold of 0.00781 cm/A at room temperature. Our value of the gain per unit current density at threshold is lower than the value of .011 cm/A measured at T = 300 K by another group [51] by about 30 %. We suspect that this difference comes from a proportionally lower value of the confinement factor in our samples due to a possibly longer electron injection region.

6.3.2 12 Cascades, n-doped separate confinement region ICLs

In order to assess the role of doping in the separate confinement regions, another IC laser was grown with two n-doped, 200 nm thick separate confinement regions. The doping concentration in the separate confinement region was 2 x 10^{17}cm^{-3} and tellurium was used for n-doping. Apart from the change in the type of doping, the rest of the laser structure was identical to a 12 cascade IC laser with p-doped SCR sample. This sample was also processed similarly. A plot of J_{th} vs $1/L_{cav}$ at room temperature is shown in Figure 6-13. By taking the ratio of the ordinate to the slope and multiplying the result by ln(R), we extract an internal loss coefficient of 10.5 cm^{-1}. As expected, the internal loss is reduced 3 cm^{-1} by using n-type doping in the separate confinement region. We attribute the 3 cm^{-1} loss coefficient to inter-valence band absorption in the p-doped material, as it has been reported to be the dominant absorption mechanism near 3.5um [54]. The absorption in n-doped material is believed to be due to inter-valley conduction band absorption [54].

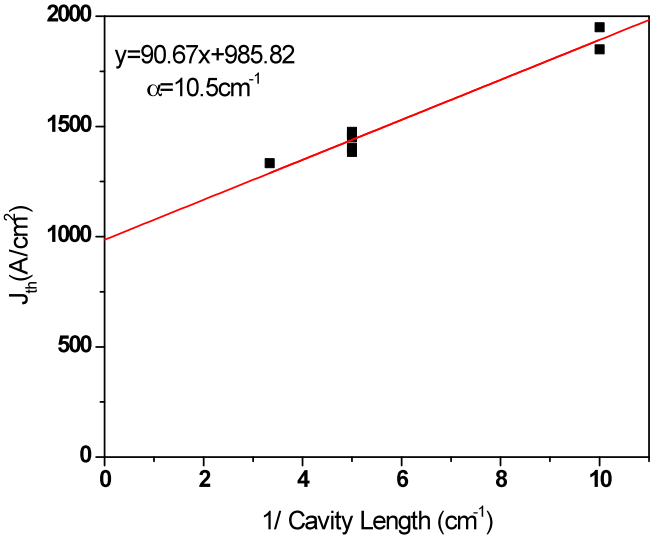

Figure 6-13 J_{th} vs. 1/Cavity length @RT for 12 cascade IC laser with n-doped SCR

6.3.3 6 Cascades, n-doped separate confinement region ICLs

In order to better understand how loss and gain vary as a function of the number of cascades, we grew a 6 cascade IC laser. The laser structure was identical to the 12 cascade IC laser with n-doped SCR sample, except that the number of cascades was reduced from 12 to 6 cascades. A measurement of J_{th} vs $1/L_{cav}$ at room temperature is shown in Figure 6-14. By taking the ratio of the ordinate to the slope and multiplying the result by ln(R), we extract an absorption coefficient of 7.1 cm^{-1}. The internal loss coefficient is reduced by a factor of 10.5/7.1 = 1.47 when going from 12 cascades to 6 cascades. The slope of J_{th} vs $1/L_{cav}$ is increased by 123/90.7 = 1.36. A simulation of the mode size indicates that the confinement factor is reduced by a factor of 1.4 when the number of cascades is reduced from 12 to 6 cascades.

Assuming that the differential gain per cascade dg/dn stays the same, we expect that the internal loss would decrease by the ratio of the confinement factors and we expect that the modal differential gain would increase by the same ratio, in good agreement with what is observed.

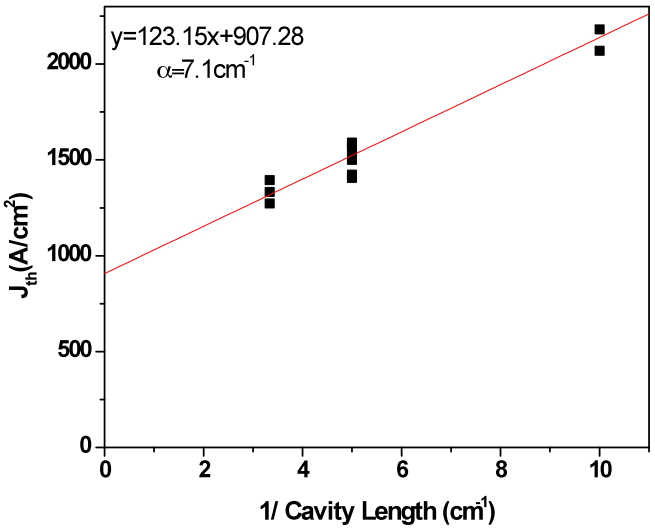

Figure 6-14 J_{th} vs. 1/Cavity length @RT for 6 cascade IC laser with n-doped SCR

6.3.4 6 Cascades, n-doped separate confinement region ICLs after reduction of losses in the hole injection region

A new 6 cascade, n-doped separate confinement region, IC laser was grown with the goal of further reducing losses in the active region. Since p-doping is used in the hole-injection region and since absorption is always larger for p-doped materials, we reduced the p-doping in both the GaInSb and the GaSb wells next to the active

region. The p-doping in the GaInSb well was reduced from .7 x $10^{17}cm^{-3}$ to .4 x $10^{17}cm^{-3}$ and the p-doping in the GaSb well was reduced from 2.5 x 10^{17} to 1 x $10^{17}cm^{-3}$. A measurement of J_{th} vs $1/L_{cav}$ at room temperature was performed in this sample and is shown in Figure 6-15. An internal loss coefficient of 4.8 cm^{-1} was extracted, a record low value for an interband cascade laser. The optical confinement factor appears to have also been reduced by a factor of 1.3, which might indicate that a loss reduction leads to a smaller extent of the wavefunction into the surrounding GaInSb well. A further reduction of the doping in the two surrounding wells (hole-injection layers) might lead to a further reduction of internal losses in the IC lasers. Using this material, we demonstrated a significant improvement in the high-temperature operation of our IC lasers compared to our previous best results of Tmax= 214 K [55]. We obtained a maximum cw temperature of operation of Tmax= 276 K in this material.

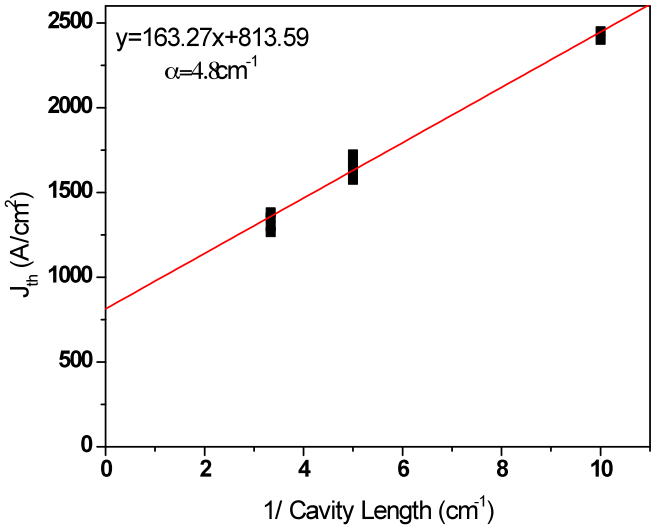

Figure 6-15 J_{th} vs. 1/Cavity length @RT for 6 cascade IC laser with reduced losses in the hole-injector

6.4 Reduce Injection Region Thickness

In order to operate IC lasers CW at room temperature, we need to reduce the injection region that is currently 553.9 Å long. Reducing the injection region by 250 Å will improve the confinement factor from $31x10^{-3}$ to $36x10^{-3}$ as we can see from the lower plot of Figure 6-16. Note that the confinement factor here is given by the mode overlap with the QWs region not with the ICL cascade region. In addition to a shorter injection region, we can further improve the confinement factor by adding one more quantum well in the ICL structure.

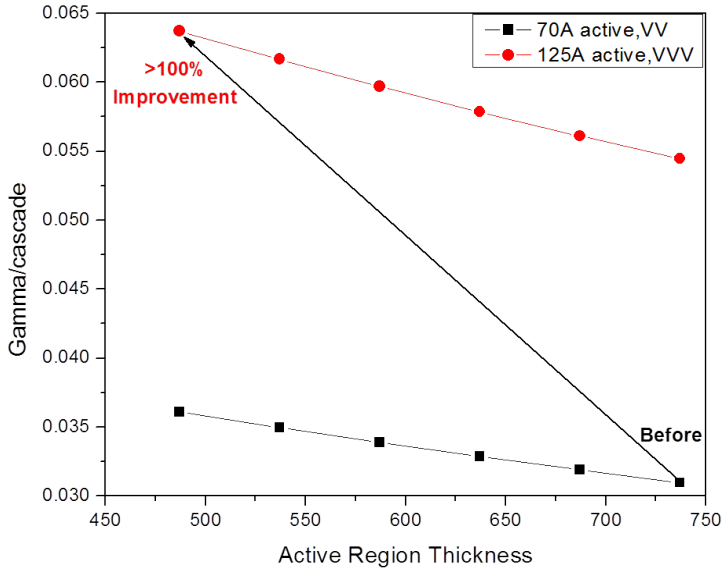

Figure 6-16. Gamma/cascade vs. injection region thickness for 70 Å and 125 Å QWs

Currently we have two quantum wells (InAs/GaInSb/InAs) that are approximately 70 Å thick and other active region layers such as GaInSb electron blocking layers are 113 Å making total active region thinkness 737 Å. If we add one

more quantum well in the ICL structure (InAs/GaInSb/InAs/GaInSb/InAs) then the quantum wells thickness will increase to 125 Å. The effect of these two the changes, a shorter injection region and adding one more quantum well, should increase the confinement factor by more than 100 % from $31x10^{-3}$ to $64x10^{-3}$ as we can see from the upper plot of Figure 6-16. Also, by adding a quantum well, we can increase dg/dn, the differential gain per cascade. As a result, Γ dg/dn should increase significantly and, according to Equation 2-18, this will reduce the threshold current density so that we will be able to operate IC lasers CW at room temperature.

6.5 Au/Sn Epi-down mounting

In order to operate the IC laser at room temperature, we have to find a way to improve thermal dissipation. The most obvious improvement is how the laser device is mounted to its heatsink. The traditional and most commonly used way to mount IC lasers is the epitaxial side-up mounting. There are several advantages of doing epi-up mounting. First, the active region is far away from the solder on the substrate so large variation of the solder thickness can be tolerated without covering the facets that might cause beam shadowing or device shorting. Second, the epi-up mounting relaxes the requirements of length of the heatsink and the precision of the laser placement while mounting the laser. It is very clear that the heatsink must be longer than the laser, because heat generated from the overhang region will not be dissipated easily. However, if the heatsink is too long then the beam may start being clipped by the heatsink surface. The epi-up mount is much more tolerant of the laser and submount

length mismatch than the epi-down mounting [56, 57]. The epi-up and the epi-down mounting using a conventional die attach equipment is shown in Figure 6-17.

However, for thermal performance, the epi-up mount is not very attractive since the ICL has very low thermal conductivity cladding layers (1.4 um upper, and 4 um lower) as we can see from table 4-1. The heat generated in the active region has to travel through the 4 um thick lower cladding layer and 100 um GaSb substrate before it reaches the heatsink. This longer path and low thermal conductivity cladding lead to an increase of the thermal resistance of the device. High thermal resistance prevents the IC laser from operating CW at room temperature. As we saw in Figure 4-4, we can lower the thermal resistance by mounting the IC laser epi-down. The thermal simulation and experimental results show that we can improve the thermal resistance by approximately 20 % by doing the epi-down mounting.

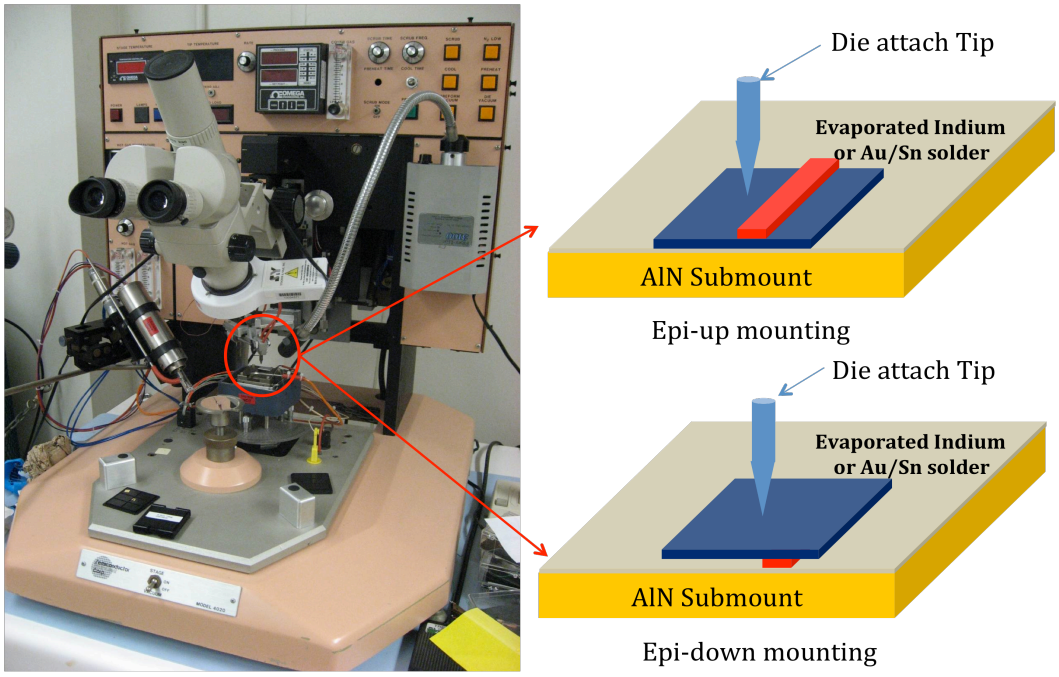

Figure 6-17. Epi-up and down mounting using either Indium or Au/Sn

We performed the epi-down mounting using evaporated indium on an aluminum Nitride (AlN) submount. AlN is the standard submount for InP material since the coefficient of thermal expansion (CTE) of the AlN ($4.5x10^{-6}\ K^{-1}$) matches to InP. However, GaSb has a CTE of $7.75x10^{-6}\ K^{-1}$ and will create a large mismatch with the AlN submount. Such a large mismatch creates undesirable stress in the IC laser structure, both those frozen in after soldering and those occurring because of normal operation temperature gradients. These stresses degrade the laser performance significantly and could lead to laser failure. Also, the use of indium is not very desirable due to its rapid oxidation rate and is not compatible with flux free soldering [56-59]. Also, indium has the tendency to create whiskers over time, which leads to reliability issues.

In order to avoid the use of indium, many researchers have been using gold/tin (Au/Sn) eutectic solder. Since the eutectic composition of the Au/Sn alloy is 80 % Au and 20 % Sn, Au/Sn material has very low oxidation rate and it can be used without flux. Also Au/Sn is compatible with standard micro fabrication techniques. However, because Au/Sn is a hard solder with very high melting temperature (~300 ºC), Au/Sn should be used with matching CTE submount & device. A good candidate for matching the CTE submount with the GaSb material is Beryllium oxide (BeO) which has a CTE of $8\ x10^{-6}\ K^{-1}$. BeO has a thermal conductivity of 330 W/mK which is even higher than AlN and has 10^{15} ohm-cm resistivity.

Also, our IC lasers seem to be sensitive to temperatures above 320 ºC so we have performed an annealing study on our IC laser samples. The goal of this study was to

assess the impact of mounting IC lasers using a hard solder process (i.e. Au/Sn) by measuring the change of the laser threshold over a similar temperature cycling process used for mounting lasers. We wanted to study the change of the laser threshold following a temperature rise of the laser chip to temperatures similar to the ones encountered during the mounting of laser chips over short periods of time, of order 5 minutes. Figure 6-18 shows the results that were obtained for the laser threshold current following several temperature rises of the sample and keeping the temperature at each step for 5 minutes. As can be seen, there is a sizable change of the threshold current.

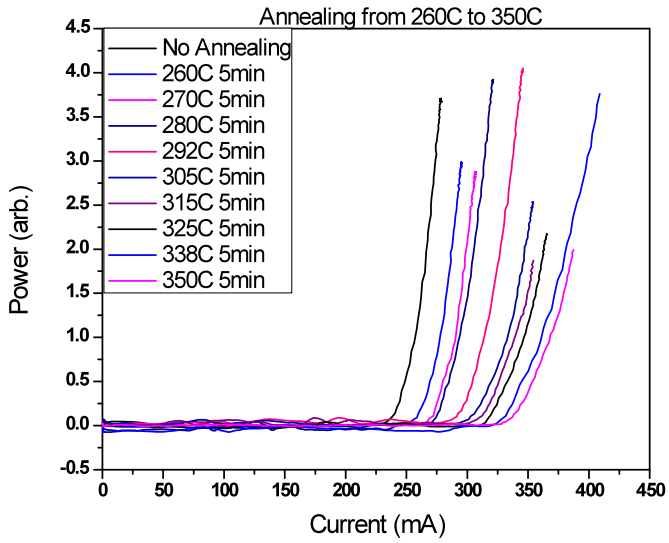

Figure 6-18 Change of the laser threshold for temperature step annealing from 260 ºC to 350 ºC.

Figure 6-19 shows the change of the laser threshold when the temperature is increased in one step from room temperature to 350 ºC. The temperature is maintained at 350 ºC for 5 minutes and then it is lowered.

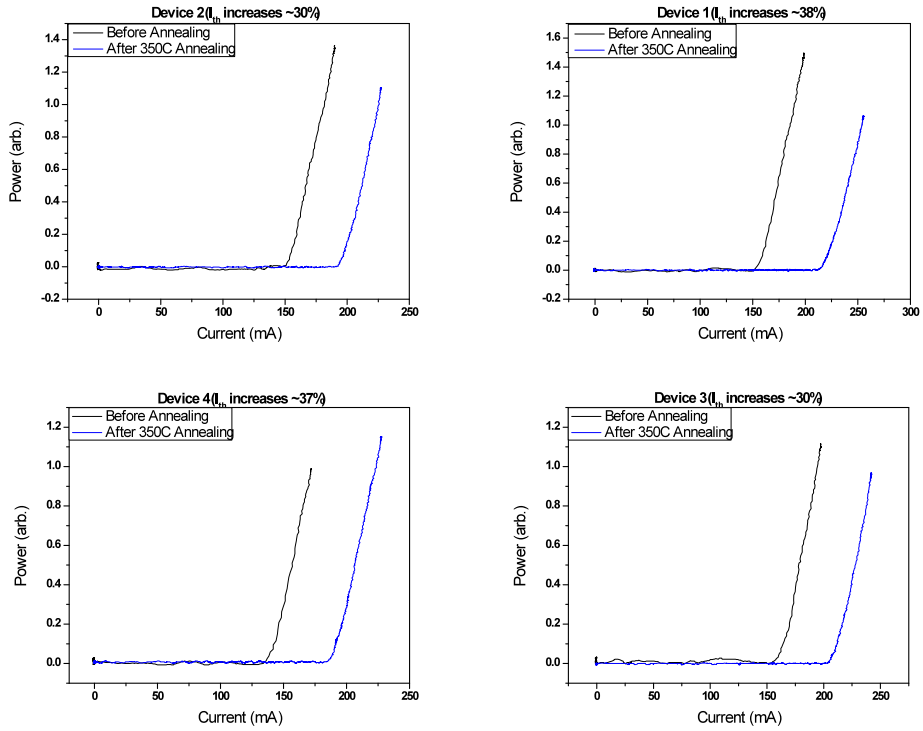

Figure 6-19 Change of the laser threshold as the temperature is increased from RT to 350C and kept there for 5 min for 4 different samples

As shown in Figure 6-19, we see a significant laser threshold increase of about 30 %. We postulate that this threshold increase is due to diffusion of metal in the active region. For these lasers, a standard Ti/Pt/Au metallization was used on both sides of the laser. We have also looked at different barrier metals to achieve thermally stable ohmic contacts.

The usual epitaxial side contact to the laser structure consists of (Ti/Pt/Au) with (30nm/100nm/150nm) thicknesses. Titanium works as an adhesive layer and Platinum works as a diffusion barrier for gold. The thickness of Au in this contact is not of critical importance since it will be followed by 3um of electroplated gold.

Devices that use this composition have been annealed at 350 ºC for 1min (the universal annealing condition for this study) and the threshold current was increased

by 30% after annealing. In order to improve the thermal stability of the contact the most natural approach is to increase the barrier. In case of Titanium the minimum thickness that serves the purpose of adhesion should be used. For these reasons we used the combination of (10nm/200nm/150nm) which worked fine before the annealing, and became shorted after annealing at 350 ºC. Then we went back to the original combination and tried to move in a different direction. At the same time it seemed like a good idea to also place a very small layer of platinum to block titanium in case it contributed to the diffusion. The next combination we tried was (Pt/Ti/Pt/Au) with thickness (5nm/40nm/40nm/150nm) and the threshold current increased by 35% after annealing. At this point it appeared that the increase of the Titanium thickness might positively affect the thermal stability. In fact, it was observed that the (Ti/Pt/Au) combination with (60nm/40nm/150nm) thicknesses did not achieve good Ohmic contact. No diode-like voltage/current behavior was observed.

The next approach was to try materials other than Titanium and Platinum. The first candidate was Molybdenum and we used the (Mo/Pt/Au) combination with thicknesses of (25nm/40nm/150nm); the threshold current increased by 30% after annealing. The results suggest that (Mo/Pt/Au) is also a decent contact but it did not outperform the (Ti/Pt/Au) contacts.

The next candidate was Tungsten (W) and we used it in (Cr/W/Au) combination with thicknesses of (2nm/50nm/150nm). In this case we observed a diode-like voltage/current, which suggests that the device must have begun to lase. However, we only obtained the amplified spontaneous emission and lasing was not

observed. To summarize the results, the Ti/Pt/Au still gives the best results. We still need to find suitable materials for thermally stable contacts.

In addition to thermally unstable ohmic contacts we have found another issue that prevents us to use Au/Sn for an epi-down mount. The SEM pictures of Au/Sn epi-down mounting show that the trench areas were not filled with Au/Sn. The difference between the indium solder and the Au/Sn solder is clearly shown in Figure 6-20. Indium solder filled up the trench area completely but Au/Sn solder did not fill up the trench area. We believe that this happens because thick electroplated gold diffuses into the Au/Sn as soon as the laser has made in contact with high temperature Au/Sn solder and it raises the Au/Sn melting temperature. The solution is to put the gold diffusion barrier metal after the electroplating.

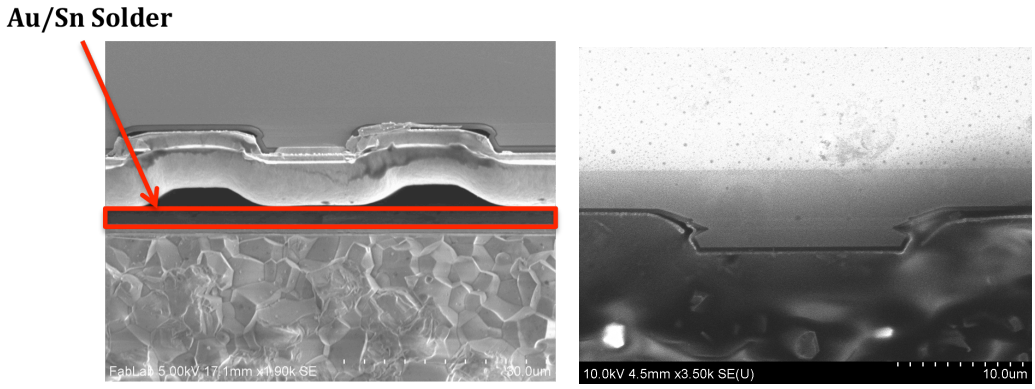

(a) (b)

Figure 6-20. SEM picture of epi-down mount using (a) Au/Sn, (b) Indium on AlN submount

6.6 Room Temperature CW Operation

With all improvements that we mentioned in earlier chapters, a 5 cascade, n-doped separate confinement region IC laser was grown with a reduced size electron-injector. The length of the electron-injector was reduced from 55 nm to 25 nm for each stage. 10 μm wide ridge lasers of length 1, 2, 3, and 5 mm were used for a J_{th} vs length^{-1} analysis. The results are shown in Figure 6-21. An internal loss of 4.9 cm^{-1} was extracted and a threshold current density as low as 320 A/cm^2 was obtained in 5mm long devices, which compares to the best IC lasers operated CW at room temperature. By reducing the length of the electron injector, a significant reduction of the slope and of the intercept of the curve of J_{th} vs length^{-1} was obtained. This indicates that much lower threshold current densities are now achievable. After the J_{th} vs. cavity length measurement, it was very clear that we would get the room temperature operation since the threshold current density was very low. Using this material, we demonstrated an output power of 23mW/facet with a 3mm long uncoated laser. With HR/AR coatings we demonstrated 41mW output power with 3mm long devices.

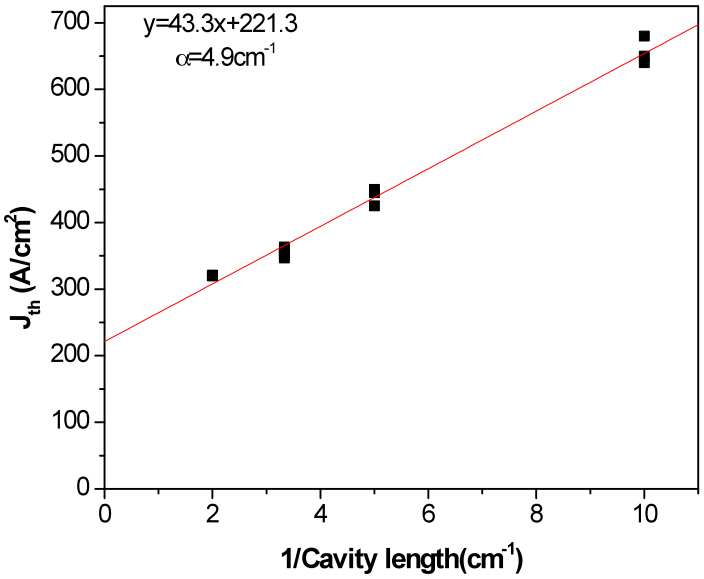

Figure 6-21 J_{th} vs 1/L for a 5 cascade IC laser with reduced length electron injector.

Figure 6-22 shows the current-voltage-light measurement results of 3mm U/U, HR/U, and HR/AR coated IC laser. As we expected, after the HR coating on the back facet, the slope efficiency is increased from 76mW/A to 105mW/A and the threshold current density is decreased from 180mA to 160mA. When we added single layer AR coating on the front facet, the slope efficiency is increased from 105mW/A to 163mW/A and the threshold current increased from 160mA to 225mA. HR coating reflectivity was calculated to be about 95% and AR coating reflectivity was calculated to be about 8%. This calculation is based on the threshold current density and the slope efficiency change.

After HR/AR coatings we expected to get even higher power since our sample has similar threshold current density, slope efficiency and V_{th} compared to the one that emits a record high power from NRL. However, at higher injection current, the

voltage across our IC laser is much higher than the NRL IC laser. As we can see from Figure 6-22 and 6-23, our 3mm device shows a voltage ~3.4V @600mA as compared to an NRL device of 2mm long which shows a voltage~2.7V @600mA. This voltage difference makes our laser dissipate more power at higher injection current which results in a faster thermal rollover. We believe that we can solve this problem by adjusting the doping level in the injection structure in our laser.

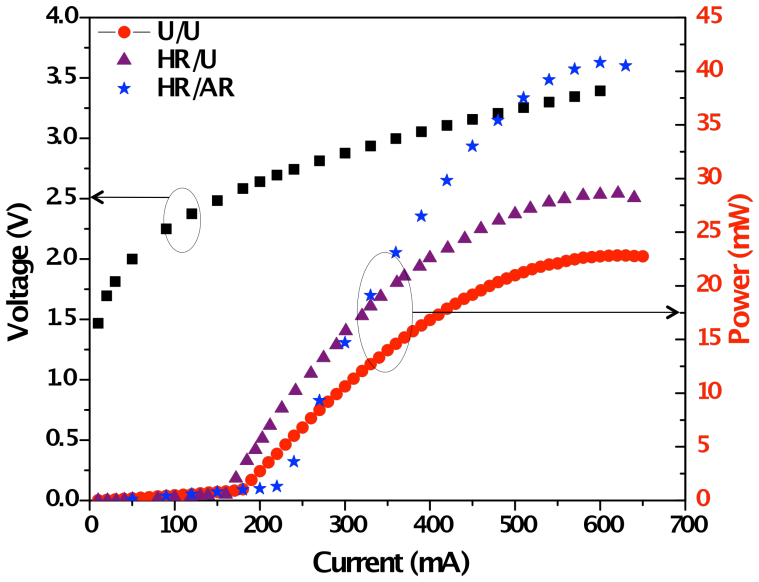

Figure 6-22 IVL measurement results of U/U, HR/U, and HR/AR coated 3 mm long, 13 μm ridge lasers, at room-temperature (T=20 ˚C).

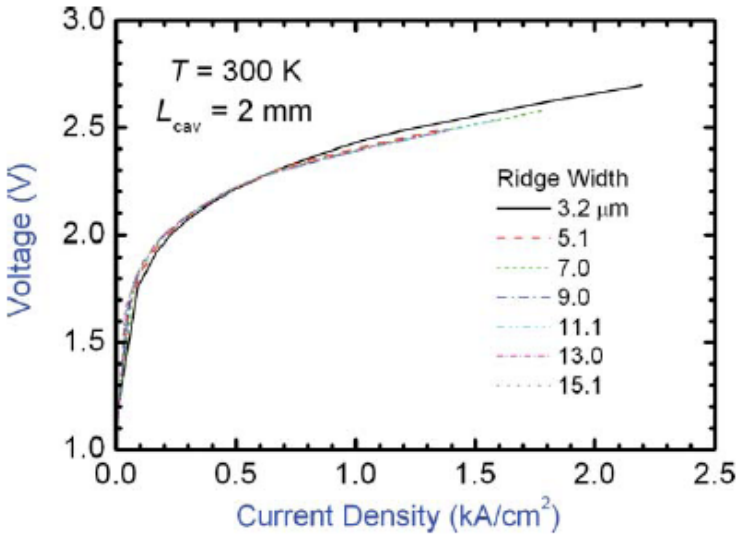

Figure 6-23 Current density vs. voltage characteristics of NRL 2mm devices [16]

In order to increase the output power, we have fabricated longer cavity length IC lasers and have also optimized the AR coating design to get lower reflectivity than a standard reflectivity that we typically can obtain of 10^{-2} with single layer coating.

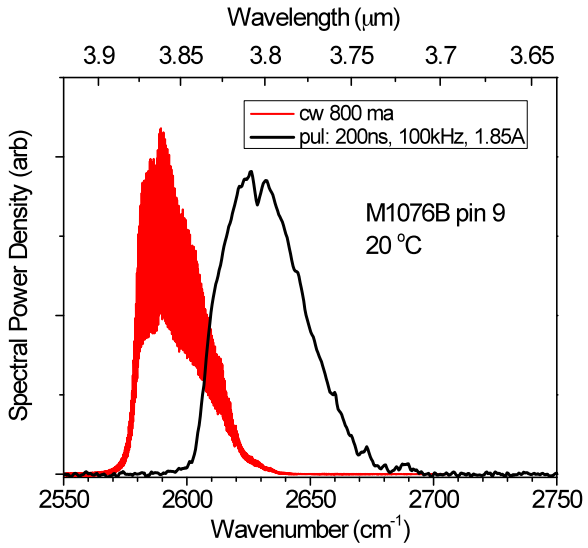

Figure 6-24 5 cascade IC laser emission spectrum of pulsed and CW measurements

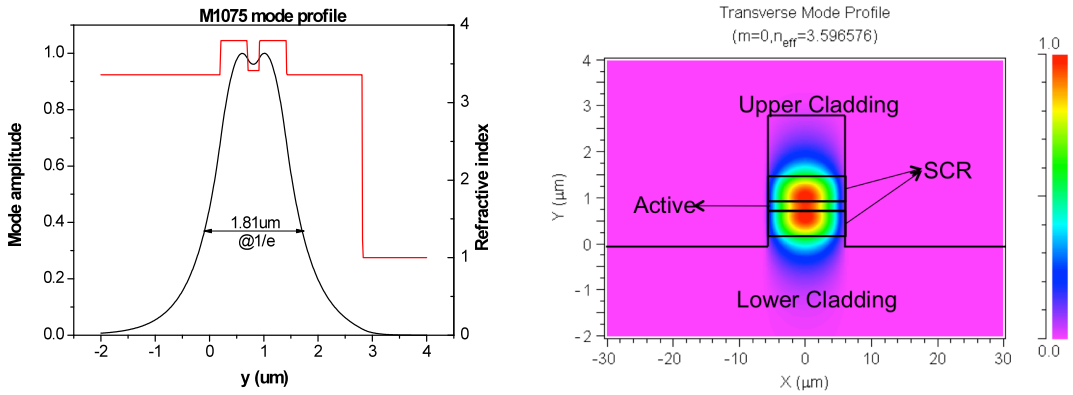

Figure 6-25 Mode profile of 5 cascade IC laser

To have an accurate AR coating design, we needed to know the emission spectrum and mode profile as shown in Figures 6-24 and 6-25. We then simulated a double layer AR coating with ZnS/SiO_2 and the simulation result of reflectivity vs. wavelength is shown in Figure 5-9. To precisely control the film thicknesses, we monitored the reflected power from a reference sample in the e-beam evaporator by reflectometry in addition to the crystal monitor as shown in Figure 6-26. The wavelength of light that we used for the reflectometry system is 1.31um and this is why we do not see low reflected power in Figure 6-26 after AR coating.

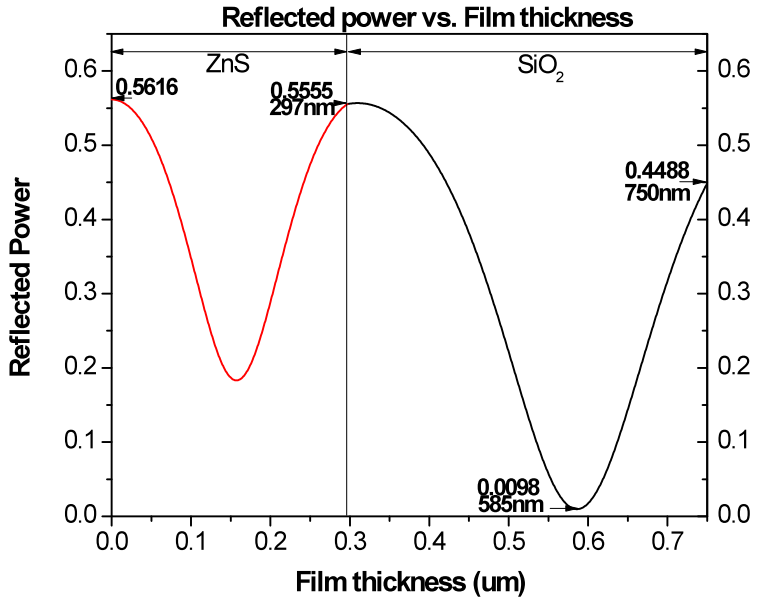

Figure 6-26 Reflected power vs. Film thickness using 1.31um laser

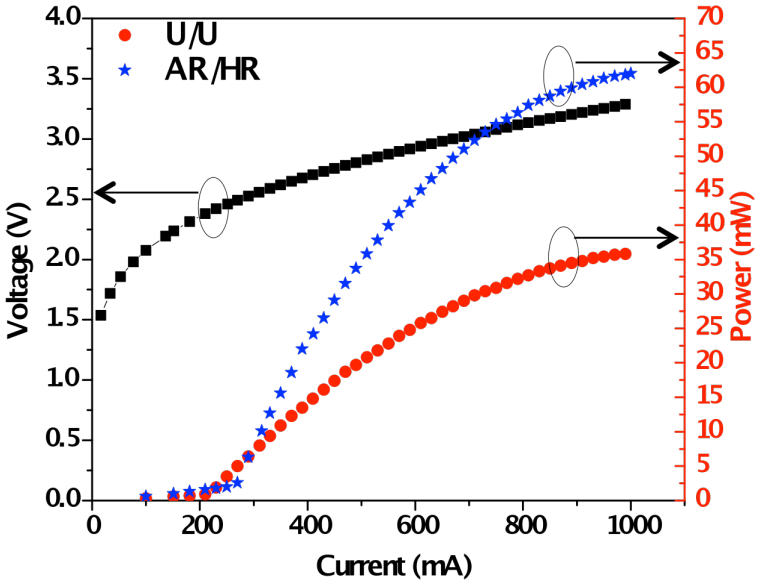

Figure 6-27 IVL measurement results of U/U and HR/AR coated 5 mm long, 12 μm ridge lasers, at room temperature (T=20 ˚C).

Figure 6-27 shows the cw current-voltage-light measurement results in a 5mm long U/U, HR/U, and HR/AR coated IC lasers at RT. With a 5mm long device, we demonstrated an output power of 35.8mW/facet uncoated. With HR/AR coating we can get 62mW output power and the laser slope efficiency is increased from 75mW/A to 170mW/A. After the HR/AR coatings the threshold current increased to 270mA. HR coating reflectivity was calculated be about 95% and AR coating reflectivity was expected to be lower 0.1%. In fact, after HR/AR coating we expected to have higher slope efficiency since we have very good quality coating but we observed some device degradation after coatings. We believe that this performance degradation comes from AR coating temperature. As we mentioned earlier our lasers are very sensitive to temperature but we have been coating our laser at higher temperature (200ºC). This might lead to performance degradation similar to what we mentioned in epi-down mounting section.

Now, we are in the process of coating our laser at lower temperature to reduce performance degradation. Solving this problem will allow us to operate IC laser with higher output power at room temperature.

Chapter 7: Conclusion and Future work

In this chapter, we will summarize the challenges that we faced and improvements that we made during my Ph.D study. Also we will discuss the future direction of this project in order to develop applications that we mentioned earlier.

7.1 Conclusion

Throughout my Ph.D study, I have focused on research that can improve the performance of IC laser for cw operation temperature as well as its output power. It all started with improving the device fabrication processes. At the beginning we developed wet etching processing using phosphoric acid based etchant but now we use dry etching processing with flash wet etching. Dry etching based processing improves the device performance consistency and the thermal behavior. After the process development, we spent most of our time on improving the device performance. This included improving the thermal characteristics, optimizing the lower and the upper cladding thickness to reduce loss, introducing SCH region to achieve higher confinement factor, reducing the number of cascades, adjusting the doping concentration in the active region, and reducing the injection region thickness.

With all these improvements, a 5 cascade, n-doped separate confinement region IC laser was grown with a reduced size electron-injector. This laser can generate an output power of 62mW with a 5mm long cavity length with HR/AR coating with an extracted internal loss of 4.8cm^{-1} and a threshold current density of as

low as 300A/cm^2. We believe that we can increase the output power by further adjusting the doping level of the active region structure of IC lasers.

Achieving a high power cw room temperature operation IC laser is a significant milestone toward many applications. The next step will be developing applications using our new and improved IC lasers.

7.2 Future work

Throughout this project, we were able to discover and improve many aspects of interband cascade lasers and now we have high power interband cascade lasers that can operate cw at room temperature. As we mentioned earlier, the mid-IR (3~5um) spectral region can be used in many civilian and military applications such as chemical sensing, free space optical communications, and IR countermeasures. These applications also require narrow, single spectral mode output that can be tuned over as wide a wavelength as possible with high output power. Previously, our group demonstrated an external cavity laser with a tuning range of 300nm in pulsed mode operation at -40 ºC [44].

It seems that the easiest way to have a single spectral mode IC laser is to have a narrow ridge of about 5um. However, narrow ridge devices can suffer from scattering loss due to the rough sidewall. Another approach is the distributed feedback (DFB) structure. The main challenge of DFB operation is the suppression of lasing in higher-order lateral modes, TE_{0m} with m>0. Corrugated sidewalls, as suggested by NRL can be used to suppress the higher order modes [60].

Also, we still need to increase the output power. One approach is to increase the number of quantum wells in the active region. By increasing the number of

quantum well in the active region, first we can improve the confinement factor; second, we can reduce the carrier density in the active region. This can potentially reduce the Auger recombination.

We believe that having a high power, single spectral mode and high tuning range room temperature cw interband cascade laser is the ultimate goal for this project and we also believe that it will be achieved in the near future by our group members.

Part 2:High efficiency p-side down InGaN/GaN solar cell

Chapter 8: Introduction

According to the United State Geological Survey (USGS), conventional crude oil production is expected to peak in 2037, but no one knows exactly how long we can continue to use conventional crude oil [61]. Also, a by-product of burning coal and crude oil is greenhouse gases, which contribute to increasing the concentration of carbon dioxide, methane, and nitrous oxides in the atmosphere. Indeed, these gases have increased dramatically since 1950. Many researchers have investigated renewable energy sources that can replace fossil fuel based energy resources. Solar energy is one of the best candidates for replacement. As a matter of fact, solar energy is much greater than all other renewable energy sources, including wind energy, geothermal energy, and fossil based energy, combined.

Since the 1950s, silicon solar cells have been intensively studied and developed. Solar cell technology has greatly benefited from the maturity of silicon technology developed originally for the IC industry. This has led to the development of high quality single crystal silicon wafers with low dislocation densities. However, because of the poor spectral overlap between the absorption of a silicon cell and the spectrum of solar light, silicon solar cells cannot fundamentally achieve high efficiency. In order to achieve high efficiency solar cells, researchers have investigated many alternatives including tandem cells, GaAs, and III-Nitride materials. During my Ph.D study, I have worked on developing high efficiency p-side down III-Nitiride solar cells. III-Nitride solar cells consist of multiple semiconductors thin films generally produced using molecular beam epitaxy (MBE) or metal organic chemical vapor deposition (MOCVD). Using these deposition techniques, people

have been able to grow good quality III-Nitride material and this has led us to develop high efficiency solar cells. Also having grown the solar cell with the p-layer down, it is possible to use the polarization charges that develop in the GaN material system to our advantage. Also, p-side down structures allow the possibility of realizing an etch-free fabrication process.

In Chapter 9, I will present the background information on solar cells including the operation principles and the characterization of solar cells. Also I will discuss various high efficiency solar cell approaches, challenges in the InGaN technology such as low quality templates, high p-type doping, polarization, and ohmic contact to p-InGaN. A p-side down solar cell design is presented in Chapter 10. The advantages of p-side down structure are also discussed in this chapter. In Chapter 11, the experimental procedure is explained including the mask design and the etch-free GaN/InGaN solar cell fabrication steps. Preliminary film and device characterization results are presented in Chapter 12. In Chapter 13, I will conclude with summarizing our approaches to achieving high efficiency solar cell using III-Nitride technology and future work.

Chapter 9: Background

9.1 P-N junction diodes

A basic photovoltaic device can be made using a p-n junction diode. Figure 9-1 shows a simple p-n junction diode structure and its band diagram. The n-type semiconductor region has a high concentration of elections but a small hole concentration. Electrons can flow easily through n-type semiconductor without recombining with holes. In the p-type semiconductor region, holes can flow easily through the p-type region without recombining with electrons. This asymmetry in the semiconductor structure is the basic requirement for photovoltaic energy conversion.

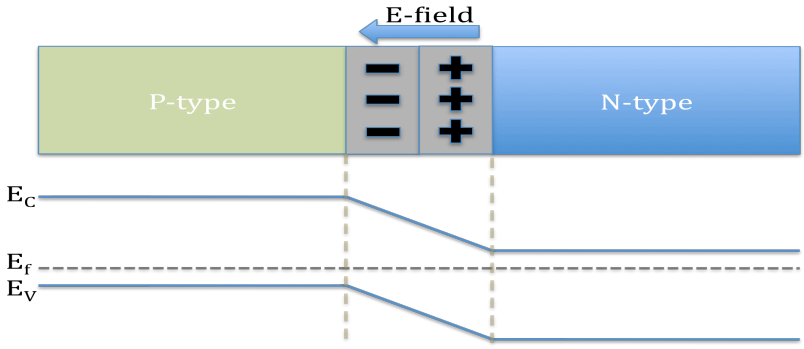

Figure 9-1. Simple P-N junction diode structure and band diagram

The asymmetry in the carrier transport properties encourages a flow of photo-generated electrons from the p-type region to the n-type region, and a flow of holes in the opposite direction. The p-n junction can be operated in three different conditions, forward, reverse and zero (equilibrium) bias. For a detector, reverse bias is applied and for solar cell, no bias (zero bias) is applied to the p-n junction.

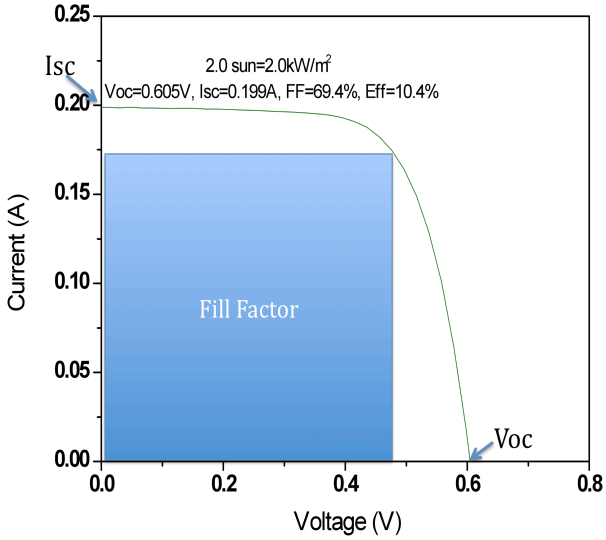

Figure 9-2. Solar cell I-V curve.

Three parameters are usually considered to characterize the solar cell I-V characteristics, and these are shown in Figure 9-2. One of these is the short-circuit current I_{sc}. Ideally, this is equal to the generated light current I_{ph}. When the band gap of the semiconductor material decreases, the short-circuit current density increases. More photons have the energy required to create electron-hole pairs as the gap becomes smaller. A second parameter is the open-circuit voltage V_{oc}. V_{oc} can be derived from the diode equation and is given by Eq (9-1).

$$V_{OC} = \frac{kT}{q}\ln(\frac{I_L}{I_0}+1) \tag{9-1}$$

V_{OC} is determined by the properties of the semiconductor and it depends on the saturation current I_0. The saturation current is determined by the material properties and is given by Equation (9-2).

$$I_0 = A(\frac{qD_e n_i^2}{L_e N_A} + \frac{qD_p n_i^2}{L_p N_D}) \tag{9-2}$$

where A is the cross sectional area of the diode, D is the diffusion constant, L is the diffusion length. Since $n_i^2 = N_c N_v \exp(-\frac{E_g}{kT})$, a reasonable estimate of the saturation current as a function of band gap is given by Equation (9-3)

$$I_0 \propto \exp(-\frac{E_g}{kT}) \text{ A/cm}^2 \tag{9-3}$$

Equation (9-3) indicates that the maximum value of V_{oc} decreases with decreasing the band gap. This trend is opposite from that observed for I_{SC}. As we have seen, I_{SC} increases with a decrease of the band gap since more incident light can be absorbed by the solar cell.

The power output for any operating point in the fourth quadrant is equal to the area of the rectangle indicated by Figure 9-2. One particular operating point (V_{op}, I_{op}) will maximize this power output. The third parameter, the fill factor, FF, is defined as Equation 9-4.

$$FF = \frac{V_{op} I_{op}}{V_{oc} I_{sc}} \tag{9-4}$$

It is a measure of how "square" the output characteristics are. For cells of reasonable efficiency, it has a value in the range of 0.7 to 0.85. Ideally, it is a function only of the open-circuit voltage Voc. The energy-conversion efficiency, η is then given by Equation (9-5).

$$\eta = \frac{V_{op} I_{op}}{P_{in}} = \frac{V_{oc} I_{sc} FF}{P_{in}} \tag{9-5}$$

where P_{in} is the total power in the light incident on the cell. Energy-conversion efficiencies of commercial silicon solar cells generally lie in the 10% to 15% range [63].

9.2 Efficiency limits in a single junction solar cell

There are several major loss mechanisms in a solar cell and those are shown in Figure 9-3. One of the major loss mechanisms is the transmission of long-wavelength photons. If the energy of incident photons is less than the semiconductor band gap, then such photons are not absorbed in the semiconductor and are transmitted through the solar cell. In the case of silicon, this loss mechanism cuts down the single-junction silicon solar cell efficiency by 23%.

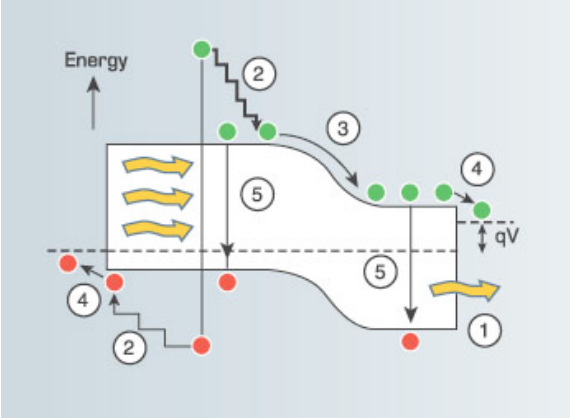

Figure 9-3. Loss processes in a standard solar cell: (1) non-absorption of below band gap photons; (2) lattice thermalisation loss; (3) junction voltage loss (4) contact voltage losses; (5) recombination loss [62]

Another complementary major loss mechanism is the thermalization loss. It is caused when the photo-excited electron-hole pair quickly loses its energy in excess of the semiconductor band gap due to absorption of a high-energy photon. Due to this thermalization loss the electron-hole pair relaxes quickly down to the conduction or valence band edge. Hence, a high-energy blue photon would only be as effective as a low-energy red photon. Another loss mechanism is due to the fact that the output

voltage is less than the potential equivalent to the semiconductor band gap energy. Voltage losses can be caused by losses at the diode junction or due to contact resistance. For silicon, the actual band gap is about 1.1 eV however, the maximum output voltage possible is about 700 mV.

Recombination loss is another loss mechanism that can affect solar cell performance. Any material defect sites can work as a recombination site. The electrons and holes recombine at defect sites or dislocation instead of migrating to their respective junctions, thereby reducing the solar cell performance. So high quality material growth technique is required for reducing the recombination loss.

Also, there is the fill factor loss. The fill factor loss is caused by the series resistance and the shunt resistance. From the solar cell equivalent circuit shown in Figure 9-5, we can tell that R_S should be as small as possible and R_{SH} should be as large as possible. The major contributors to the series resistance R_S are the bulk resistance of the semiconductor material making up the cell, the bulk resistance of the metallic contacts and interconnections, and the contact resistance between the metallic contacts and the semiconductor. The shunt resistance R_{SH} is caused by leakage across the p-n junction, leakage around the edge of the cell, and in nonperipheral regions in the presence of crystal defects and precipitates of foreign impurities in the junction region.

There are also temperature related effects. The short-circuit current of solar cells is not strongly temperature dependent. It tends to increase slightly since the semiconductor band gap decreases with temperature. The other parameters such as the V_{oc} and FF both decrease with a temperature increase. Figure 9-4 shows the effect

of temperature and parasitic resistance on the output characteristics of a solar cell. Other loss mechanisms include reflection and shading losses.

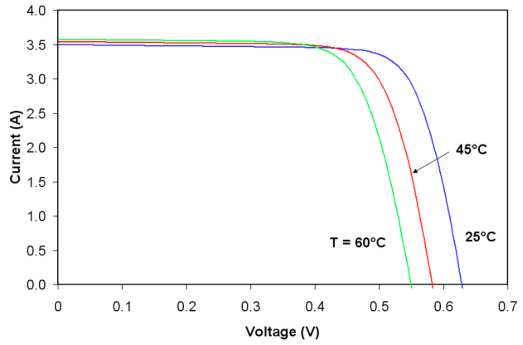

(a)

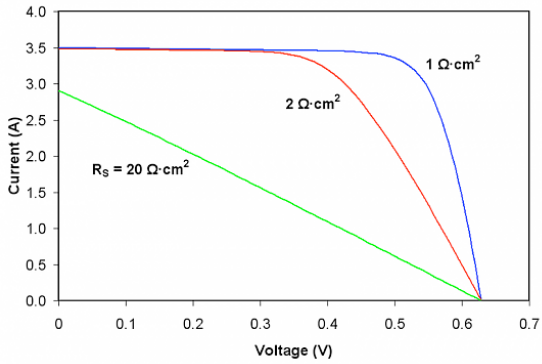

(b)

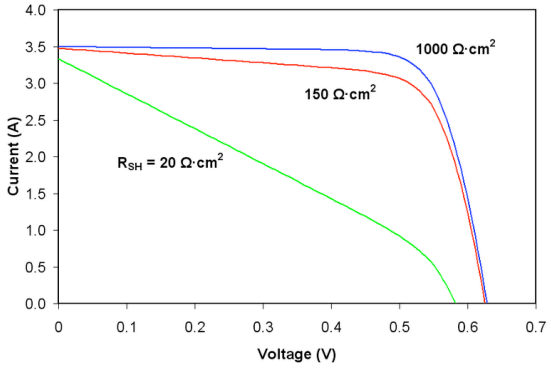

(c)

Figure 9-4. Effect of temperature and parasitic resistance on the output characteristics of solar cell (a) Effect of temperature (b) Effect of series resistance Rs, (c) Effect of a shunt resistance R_{SH} [62].

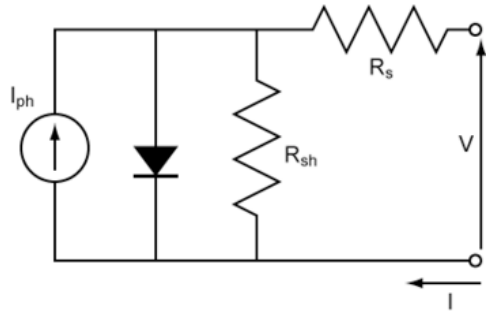

Figure 9-5. The solar cell equivalent circuit

9.3 High efficiency approaches

In order to increase the solar cell efficiency, there has been a lot of research on reducing the thickness of the wafer, buried contacts to reduce contact shading, and reduction of surface reflection by texturing. Our discussion was based on the single-junction silicon solar cells. Other types of solar cells include tandem solar cells and quantum well solar cells. Different material systems such as Ga(In)N and GaAs are also being researched.

9.3.1 Tandem solar cells

A tandem solar cell is one of the approaches that can deliver high efficiency solar cells. Stacking two or more cells that have different band gaps creates the basic structure of a tandem solar cell. Each cell converts a different range of photon energies to electrical current. The higher gap cells are stacked on the top and they absorb the high-energy photons and transmits the lower energy photons to the next level of the solar cell. Tandem solar cells sound easy to make but in reality,

increasing the number of stacks adds complications and also increases the series resistance.

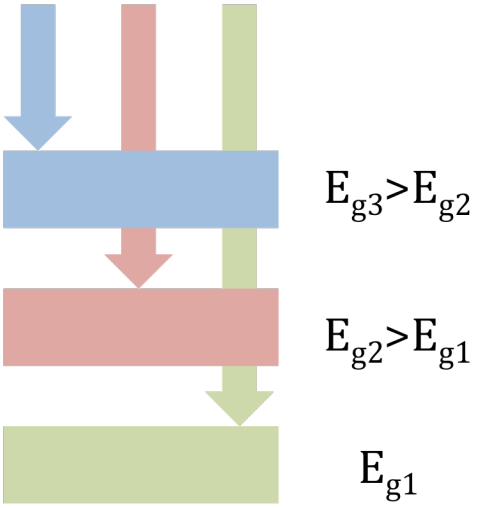

Figure 9-6. Concept of a tandem cell

9.3.2 III-Nitride solar cells

Recently it was found that the band gap energy of InN is 0.7 eV. By Combining InN with GaN which has a band gap energy of 3.4 eV, we can create the InGaN material[64-66]. The band gap of the InGaN material covers most of the visible region. It has been considered a perfect candidate for the next generation high efficiency solar cell. However, the InGaN material system faces many challenging issues such as no native substrate, difficulty of achieving high p-type doping in InGaN, large lattice mismatch, spontaneous polarization and the generation of large piezoelectric polarization in the presence of strains.

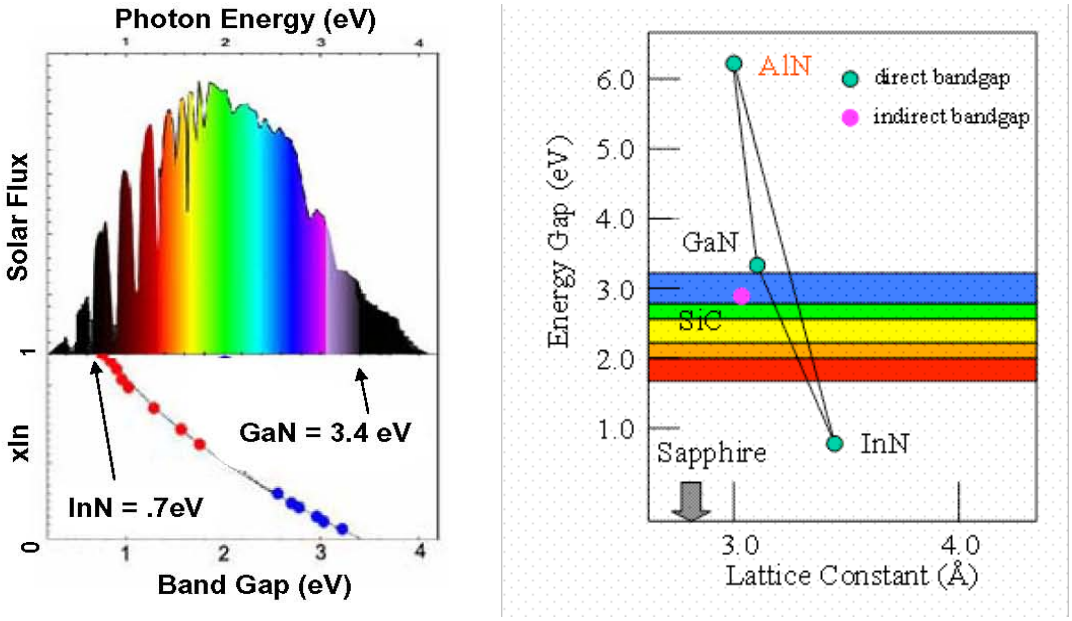

Figure 9-7 Band gap energy and lattice constant of III-Nitride materials [62]

9.4 Challenges in the InGaN Technology

As previously mentioned, InGaN technology promises many advantages. However, there are also many technical challenges to overcome.

9.4.1 Substrate material and growth quality

The III-Nitride material crystallizes in a wurtzite crystal structure. The most commonly used substrate materials are sapphire and silicon carbide (SiC). However, due to the large lattice constant mismatch (16% for GaN on shppire, 29% for InN on sapphire and 3.5% for GaN on SiC, 19% for InN on SiC) and thermal expansion coefficient mismatch, we get a high dislocation density. Higher indium composition is especially hard to achieve due to a large lattice mismatch [67,68].

9.4.2 High p-type doping

High p-type doping of the GaN material is difficult due to the high background concentration of donors that result from unintentional incorporation of impurities such as oxygen or silicon. High n-type background concentration compensates the p-dopants. Also, relatively high acceptor levels and low activation efficiency make it even harder. For p-type doping, magnesium (Mg) is typically used and the activation energy of Mg in GaN is about 208 meV [63]. Increasing the indium composition would lower the activation energy so theoretically it is possible to have high indium composition p-type InGaN material. However, as mentioned earlier, high indium composition in InGaN is not easy since the crystal quality degrades with increasing indium composition. Having a highly doped p-type material helps to have a lower resistance p-type contacts, and having a lower resistance p-type contact helps to reduce the grid spacing for the top contact.

9.4.3 Polarization

The wurtzite structure III-nitride shows its unique characteristic, the polarization effect. There are two types of polarization. One is the spontaneous polarization and the other is the piezoelectric polarization. Polarization exists in the III-nitride material due to the non-centro symmetry of the structure and the large ionicity of the covalent bond between metal and nitrogen. The GaN crystal shows two opposite sequences of layer in the c-plane, Ga-face or N-face. Gallium atoms can be replaced by Indium or Aluminum atoms. Ga-face GaN means that the Gallium atom is on the top position of the bilayer and N-face GaN means that the Nitrogen atom is on the top position of the bilayer [69,70].

- Spontaneous polarization

Spontaneous polarization exists in the III-nitride material due to the non-centro symmetry of the structure. Figure 9-8 (a) shows three polar planes in GaN crystal. The direction of the spontaneous polarization in the III-nitride is from the N-atom to the closest metal atom. In the Ga-face GaN on c-plane, the spontaneous polarization direction is toward the substrate as shown in Figure 9-8 (b), when the first layer grown on the substrate (GaN) assumed to be fully relaxed

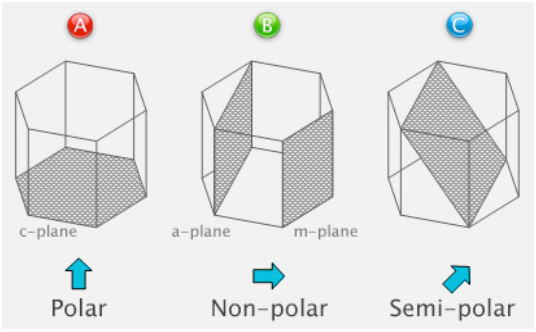

(a)

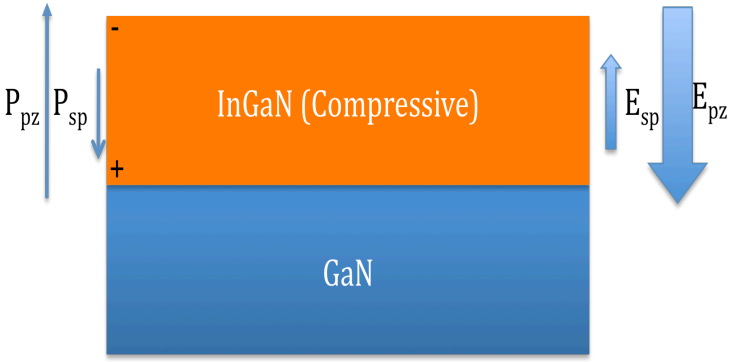

C-plane [0001] Ga-face polarization effect

(b)

Figure 9-8. (a) Three polar planes in GaN crystal [62], (b) C-plane Ga-face polarization effect

- Strain and Piezoelectric polarization

When III-nitride material is grown in the MOCVD or MBE chamber, the epi-layer will suffer strain since there is a lattice mismatch to the substrate material. Spontaneous and piezoelectric polarizations are in parallel and add to each other when the planar strain is tensile and are opposite when the planar strain is compressive (detailed piezoelectric polarization calculation is shown in appendix C). Many researchers are also investigating non-polar plane (m-plane) and semi-polar plane to control polarization effects [71].

9.4.4 Ohmic contact to p-InGaN

One of the major disadvantages of having a low p-type InGaN material is the challenge in getting high quality contacts. There is no readily available metal that can form an ohmic contact to p-type InGaN since InGaN has a high work function. Many researchers have investigated different metals for the ohmic contact which include, Pt/Ni/Au, Ni/Pt/Au, Pd/Pt/Au, Pt/Au, Cr/Au, and Au. However, these metal contacts still show Schottky behavior. Recently NiO_x has been used for contacts and showed a contact resistance as low as 10^{-6} Ohm*cm^2. However, NiOx film absorbs the incident light and it would reduce the efficiency [72].

9.4.5 Phase separation

The large difference in interatomic spacing between GaN and InN can give rise to a solid phase miscibility gap, which is also the probable cause of multiple phases and consequent multi-peak luminescence. Phase separation depends on the temperature, indium composition and the strain of the InGaN films. Phase separation not only

works as a recombination site but also it can reduce the open circuit voltage as well as the fill factor [73-75].

Chapter 10: P-side Down Solar Cell Design

For conventional c-plane, Ga-face crystals, p-up devices have a polarization field that opposes the carrier sweeping and collection. Also, in order to make a n-metal contact, conventional p-up devices need to be exposed to plasma and that might give rise to some metal contact problems. We therefore designed a high quantum efficiency p-side down InGaN/GaN solar cell. GaN layers are grown using proprietary multi-wafer Hydride Vapour Phase Epitaxy (HVPE) growth machines designed and built by TDI Oxford Plasma Inc. One of the key advantages of the technique is its high growth rate, up to 100 μm per hour, which is almost two orders of magnitude faster than typical MOCVD and MBE processes. The HVPE growth machines are equipped with an atmospheric-pressure horizontal hot-wall quartz reactor and multi-zone resistively heated furnace. For gas flow distribution and control, the gas-handling system is constructed based on electronic mass flow controllers. Commercial 2-inch diameter c-plane sapphire wafers are used as substrates. The gas flow rates can be maintained in such a way as to obtain GaN growth rates in the range of 0.3-3.0 μm/min that allow growth of both nm-thick and um-thick GaN layers. Undoped as-grown GaN layer has n-type conductivity. For n-type doping, Si is used as a donor. To grow p-type GaN layers, Mg is used as an acceptor. Typically, as-grown GaN layers doped with magnesium have p-type conductivity (the doping does not require activation). Good quality GaN layers will be grown on sapphire wafers with a low dislocation density ($< 1 \times 10^8 /cm^3$).

The thickness of the top InGaN layer is determined by the absorption profile. It is well known that InGaN absorption coefficient is as high as 10^5 cm^{-1} at the band edge. From simple calculation of absorption vs. layer thickness we can see that InGaN absorbs more than 95% of the incident light within the first 300 nm and more than 99 % within the first 500 nm. Figure 10-1 shows the simulation result of transmission vs. layer thickness. Also, since the top layer is a n-type layer we had to calculate the diffusion length of holes. The value of the hole diffusion length limits the thickness of the n-type layer and the hole diffusion length calculation is shown in Equation 9-6. Here we assume that the minority life time τ_p=0.8 ns, τ_n=2 ns and mobility μ_p=26 cm^2/Vs, μ_n=113 cm^2/Vs [76].

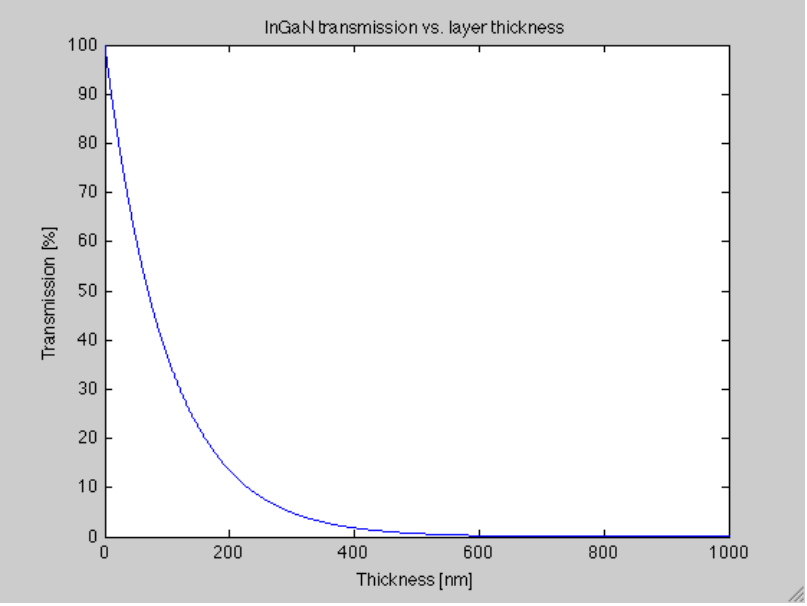

Figure 10-1. Transmission vs. InGaN layer thickness

$$\frac{D}{\mu} = \frac{kT}{q}, \quad L = \sqrt{D\tau} \tag{9-6}$$

We get D_p= 0.673 cm^2/s,D_n=2.93 cm^2/s L_p=230 nm and L_n=776 nm from Eq 9-6. As a result we proposed the following GaN p-down solar cell design, shown in Figure 10-2.

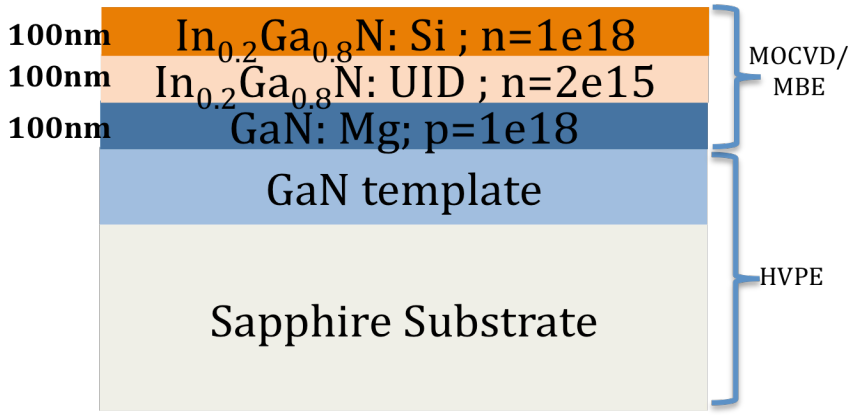

Figure 10-2. p-down p-i-n solar cell structure

Using the HVPE grown substrate supplied by TDI, ARL will grow the inverted structure presented in Figure 10-2 by MOCVD. Having grown the solar cell with the p-layer down, it is possible to use the polarization charges that develop in the GaN material system to our advantage. For instance, a theoretical calculation of the band structure shows that carriers generated in the intrinsic layer can be easily swept away in a short circuit (no applied voltage) configuration, shown in Figure 10-3 (b) and 10-4 (a). This implies that, in an open-circuit configuration (no current), a relatively large open-circuit voltage is required, which leads to a high efficiency solar cell. Figures 10-3 (a) and 10-4 (b) show what happens to the band structure when a conventional p-up solar cell structure is grown. As can be seen, a very small electric field is present when no external voltage is applied to the structure. In such a structure, it is expected that the open-circuit voltage will be quite low and will result in a low efficiency solar cell [77-79].

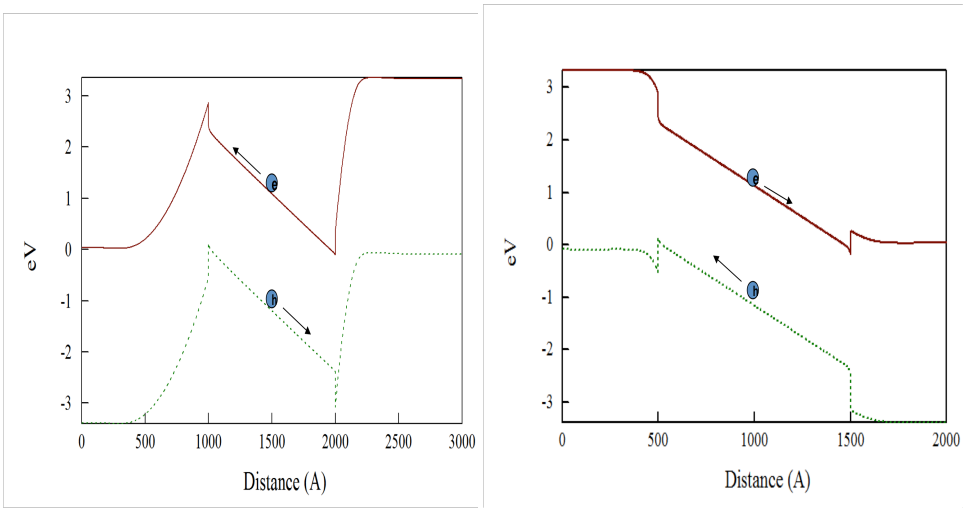

Figure 10-3 (a) conventional p-up devices: polarization field opposes carrier sweep out and collection, (b) p-down devices: polarization field and junction field in the same direction, aiding carrier sweep out and collection

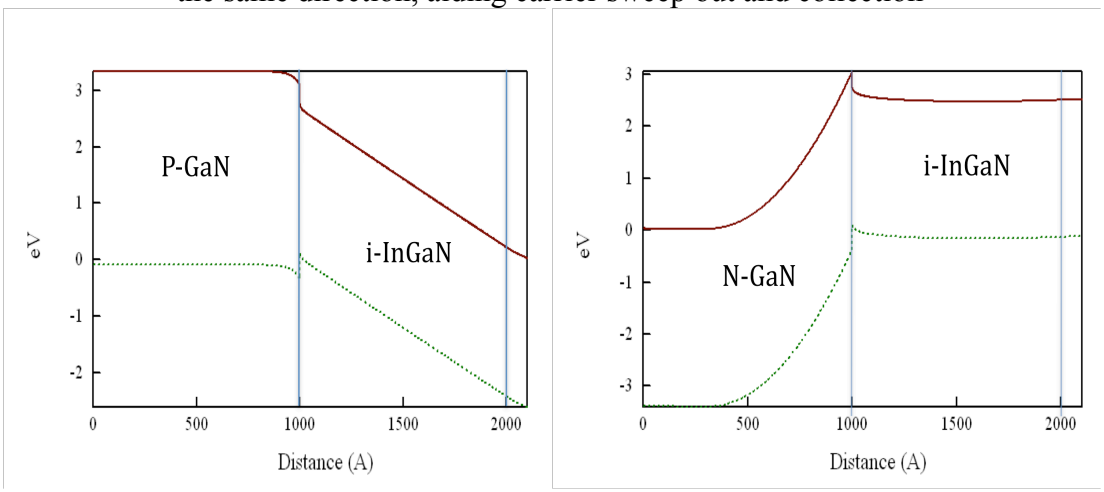

Figure 10-4 (a) Our p-down p-i-n structure band diagram, (b) p-up p-i-n structure band diagram

In addition, we used selective re-growth of the inverted structure. This will allow us to avoid putting the sample in an ICP-RIE chamber and facing the problem of p-layer compensation. Also, it might help us to reduce the use of interdigitated fingers n-type InGaN because we will have a higher conductivity. Reducing the use

of interdigitated fingers on n-type InGaN will possibly increase our efficiency since there will be less shadow loss and absorption from the top metal contact.

Chapter 11: Experimental Procedures

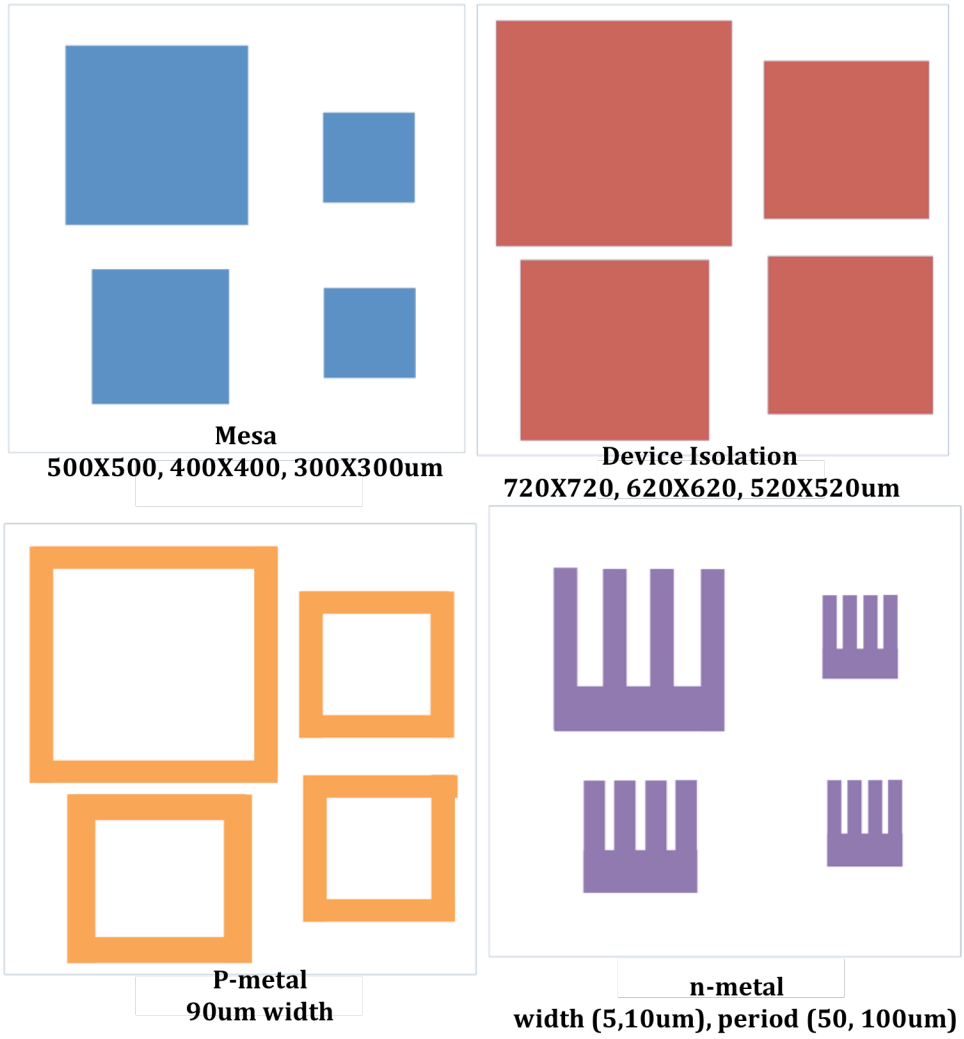

Figure 11-1 GaN p-down solar cell mask design

We designed the mask for GaN solar cells that are grown by HVPE and MOCVD. It is shown in Figure 11-1. The first mask is made for defining the mesa or the selective growth area. There are three mesa sizes 500X500 um, 400X400 um, and 300X300 um. The second mask is for device isolation. After the selective re-growth, we etch down to the insulating layer (GaN:Fe) to avoid any possibility of current

spreading through the p-type GaN layer when we measure the individual devices. The third mask is for the p-metal contact. The width of this p-metal contact is about 90 um so that we can wire bond later when we test the individual devices. The last mask is for the n-metal and we design this mask such that we can have interdigitated fingers on the n-contact layer. We vary the width of the fingers as well as their period. In this way, we can see what the optimal contact will be. We have also designed the mask for GaN solar cells that are grown by HVPE and MBE. Since the inverted structure that is grown by MBE machine is not a selective growth process, we have modified the mask so that we can etched inverted structure outside of mesa area.

GaN solar cell processing starts from cleaning the p-doped GaN on sapphire grown by HVPE. After the standard cleaning process, the lift-off resist (LOR) 5A and the shipley 1813 photoresists are deposited on the sample, exposed by UV light and developed. LOR 5A is the lift-off layer that will create the undercut. Silicon dioxide film is deposited by e-beam evaporation. This deposition will cover the entire area including the mesa area and then LOR is removed with the deposited silicon dioxide. It is critical to create the good undercut since it affects the re-growth sidewall quality as it shown in Figure 11-2.

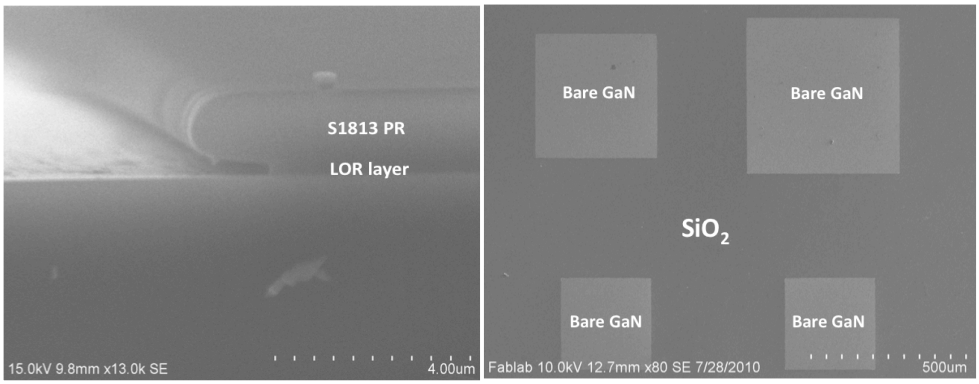

Figure 11-2 Lift-off resist layer and S1813 undercut for SiO_2 deposition

After this step, the selective mesa area is defined. The sample will be transferred to the MOCVD for growing the inverted structure. After the selective growth, the SiO_2 will be removed by wet etching. Before putting the metal contacts, we plan to isolate the individual solar cell to prevent any possible current spreading. The final step will be the n- and p-metal contact formations. We use Ti/Al/Ni/Au contact for n-metal contact and Ni/Au for p-metal contact. The GaN solar cell processing steps are shown in Figure 11-3.

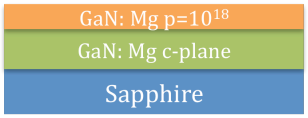

Step 1: Cleaning

Step 2: Coat lift off layer and PR

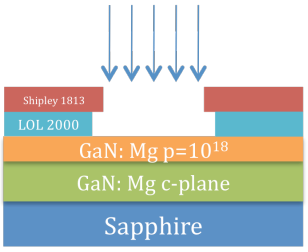

Step 3: Photo and develop. Develop in standard developer. The developer will etch the underlying LOL2000

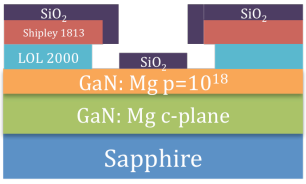

Step 4: Deposit SiO_2 film

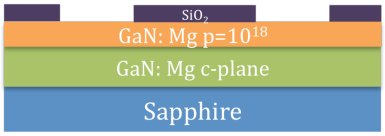

Step 5: Lift off and clean

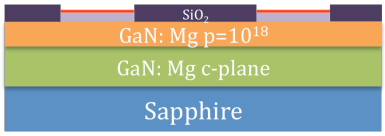

Step 6: Localized growth
(InGaN: u and InGaN: n)

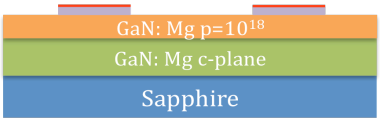

Step 7: Remove SiO_2 film

Step 10-11: Metal contacts for both n and p

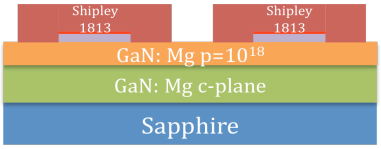

Step 8: coat, photo, and develop
This step defines the area we etch in next step

Step 9: Dry etch GaN to isolate individual device
Then remove PR

Figure 11-3. P-down GaN solar cell (HVPE and MOCVD) processing steps

Chapter 12: Preliminary Experimental Results

12.1 Film analysis

12.1.1 Hall effect, four-point, and hot probe measurements

We have performed some preliminary measurements on GaN:Mg doped samples and GaN:Fe doped samples on sapphire substrate including Hall Effect, four-point probe, and hot probe measurements. These measurements helped us to understand the nature of the GaN film on sapphire. Table 12-1 shows the GaN:Fe doped semi-insulating layer sheet resistance measurement using a four-point probe[80,81]. Sheet resistances of ~ 10^9 ohm/sq were demonstrated which is more than adequate for use as base layers for the optimization of the growth of p-type GaN template layers.

Sample number	Thickness (um)	Sheet Resistance (Ohm/Sq)	Resistivity (Ohm*cm)
1663-2	6	9.97E+08	598200
1665-2	5	1.36E+09	680000
1666-2	5	1.31E+09	655000

Table 12-1. GaN:Fe doped semi-insulation layer sheet resistance measurement results

We have also performed Hall Effect measurements on many GaN:Mg doped samples. Table 12-2 shows the results of the Hall Effect measurements. At the beginning of project, we can see clearly that all of our samples were found to be n-type rather than p-type as a result of thin n-conduction layer on the surface from

HVPE growth. These results were confirmed by UMD and ARL Hall Effect measurements

Sample Number	GaN:Mg Thickness (um)	Hall Carrier Type	Carrier Concentration ($1/cm^3$)	Mobility	Resistivity (Ω*cm)	Sheet Resistance (Ω / □)
11VS1811-3	4.2	N	5.1E+17	90.22	1.35E-01	322
11VS1810-1	4.0	N	6.8E+17	74.97	1.22E-01	306
11VS1809-2	4.0	N	8.1E+17	61.96	1.25E-01	311
11VS1808-3	4.0	N	9.1E+17	71.67	9.65E-02	241

Table 12-2. GaN: Mg doped p-type layer Hall effect measurement results

To understand the doping concentration of the surface, we have used the combination of dry etching and wet etching methods. For the dry etching method we have used Cl_2 plasma to etch GaN film followed by aqua regia (mixture of nitric acid and hydrochloric acid) wet etching step and results are shown in Table 12-3. As we can see from Table 12-3, the simple dry-wet etching method does not remove the surface n-layer.

	Concentration (cm^{-3})	Resistivity (Ohm cm)	Conductivity (1/ Ohm cm)	Mobility (cm^2/ Vs)
11VS1926-2 before	4.62e18	4.00e-2	2.50e1	3.39e1
11VS1926-2 after	4.23e18	4.38e-2	2.29e1	3.38e1
11VS1927-2 before	1.14e18	1.03e-1	9.70e0	5.33e1
11VS1927-2 after	1.45e18	8.68e-2	1.15e1	4.96e1

Table 12-3 Comparison of the Hall effect measurements before and after dry-wet etching process

After many trials, our group has developed a method to remove the thin n-conduction layer on the surface and now we measure a p-layer on the surface. The removal of the conducting n-layer helps in making good ohmic p-metal contacts.

12.1.2 Circular transmission line method (CTLM)

To accurately measure the specific contact resistance of ohmic contact, we used circular test patterns. Unlike rectangular test patterns, the circular test patterns can avoid fabrication of a mesa structure. The definition of mesa is required to confine the current flow between two contacts. Figure 12-1 shows the circular test patterns where r=200um, d=8,14,20,30,50um. By measuring I-V between the outer contact pad and inner contact pad, we can get the total resistance R_t between the contacts. Also, from the slope and y-intercept of ln(R/r) vs. R_t plot, we can calculate the sheet resistance R_{sh}, the transfer length L_t, which is defined as the point below the metal contact where the value of the applied voltage drops to 1/e of its value, and the specific contact resistance ρ_c.

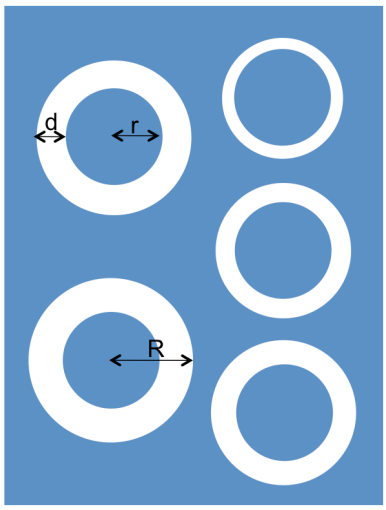

Figure 12-1 Circular test pattern for contact resistance measurement

Table 12-4 shows the sheet resistance and the specific contact resistance of two different metal contacts with different annealing temperatures. From these results, we

found that the Ni/Au combination gives better specific contact resistivity than the Pt/Au metal contact.

		$R_{sh}1$ (Ω)	$R_{sh}2$ (Ω)	$R_{sh}3$ (Ω)	$R_{sh}4$ (Ω)	ρ_c1 (Ωcm^2)	ρ_c2 (Ωcm^2)	ρ_c3 (Ωcm^2)	ρ_c4 (Ωcm^2)
Ni/Au (300A/ 1500A)	**Before annealing**	180754.67	207345.11	200992.81	205001.49	**0.01740334**	**0.00704649**	**0.01927651**	**0.01610781**
	After annealing 2min @400C	240891.04	238553.69	230655.73	253966.35	0.04764176	0.05355942	0.06146951	0.04824446
	After annealing 2+3min @400C	264804.84	259526.97	266155.73	273802.37	0.11215589	0.10988510	0.15422283	0.17410336
Pt/Au (300A/ 1500A)	**Before annealing**	402035.90	428689.17	290804.67	285030.42	0.07955294	0.09613117	0.01182144	0.05479464
	After annealing 2min @400C	445352.17	477050.84	317244.31	312054.40	0.06837077	0.07927659	0.00541511	0.03816621

Table 12-4 the sheet resistance and the specific contact resistance of two different metal contacts with different annealing temperature

We also investigated the effect of SiO_2 on p-contact since silicon or oxygen might diffuse into the p-layer at high growth temperatures. It was found that after annealing at 500˚C, a SiO_2 treated surface has similar sheet and contact resistance as compared to an untreated surface. Some of the measurement results are shown in Figure 12-2.

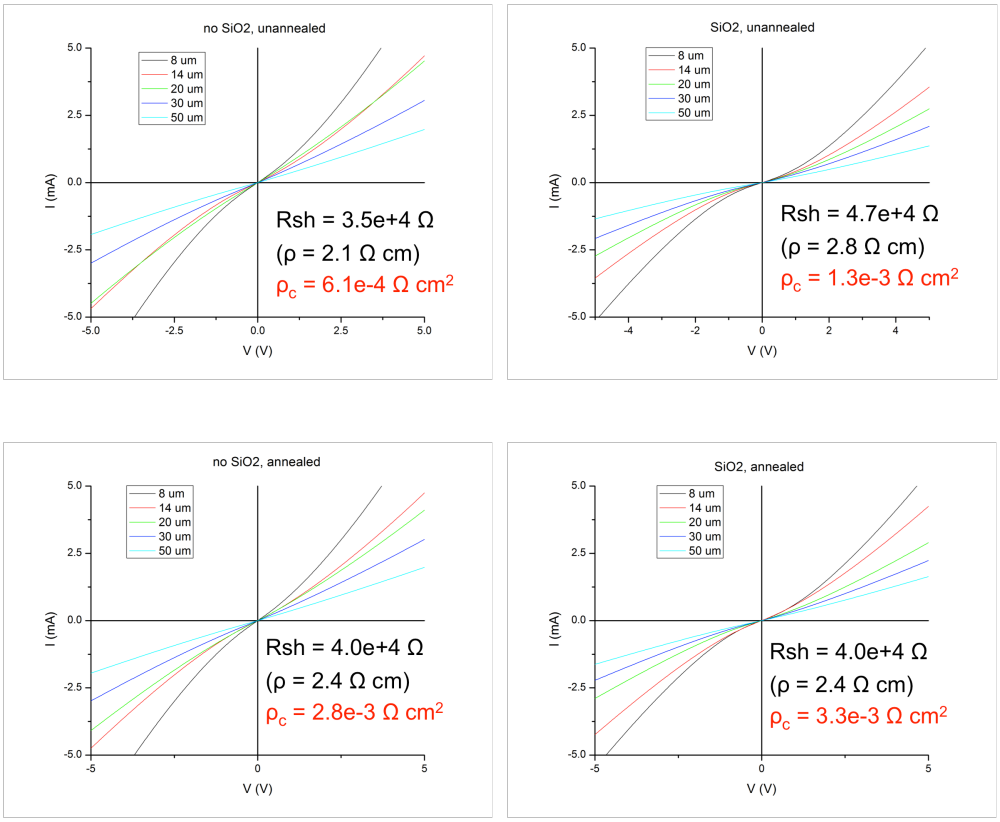

Figure 12-2 Annealing study with/without SiO_2 present

12.2 Device growth and testing results

During my Ph.D. study, we have tested many grown structures both p-i-n and n-i-p. The first structure that ARL has grown was p-GaN (150nm), UID-InGaN (100nm), and n-InGaN (100nm) structure on HVPE grown templates (0.5um, p-doped) by plasma assisted molecular beam epitaxy. p-i-n structures were grown in the MBE chamber continuously without any interruption. Photoluminescence (PL) measurements were performed on one of the grown samples (E756 sample) and Figure 12-3 shows the PL data obtained.

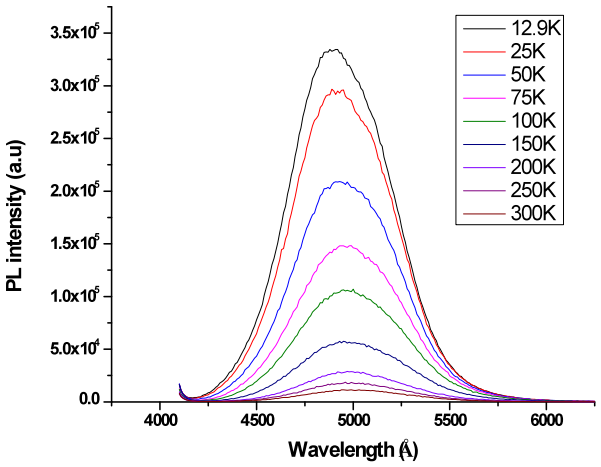

Figure 12-3 PL measurement data for p-i-n InGaN/GaN solar cell (E756)

The photoluminescence peak occurs around 500nm, which indicated that the composition of indium is about 27%. Also, at higher temperature, we observed a red shift which is expected since the band gap energy is reduced as the temperature is increased. Using a dry etching recipe, we have processed p-i-n InGaN/GaN solar cells. I-V data a for 100nm UID InGaN/GaN solar cell is shown in Figure 12-4. Also, we observed that the solar cell emitted green light around the metal and mesa edges when a forward bias was applied to it. This might indicate that there are localized energy states created by stress when we deposit metal contacts. In addition, this might indicate that we need to do passivation of the mesa sidewalls to reduce sidewall recombination. Also, we found that there is a large reverse bias leakage current due to shunting paths in the material. We believe that we can reduce these shunting passes by growing a thicker GaN template.

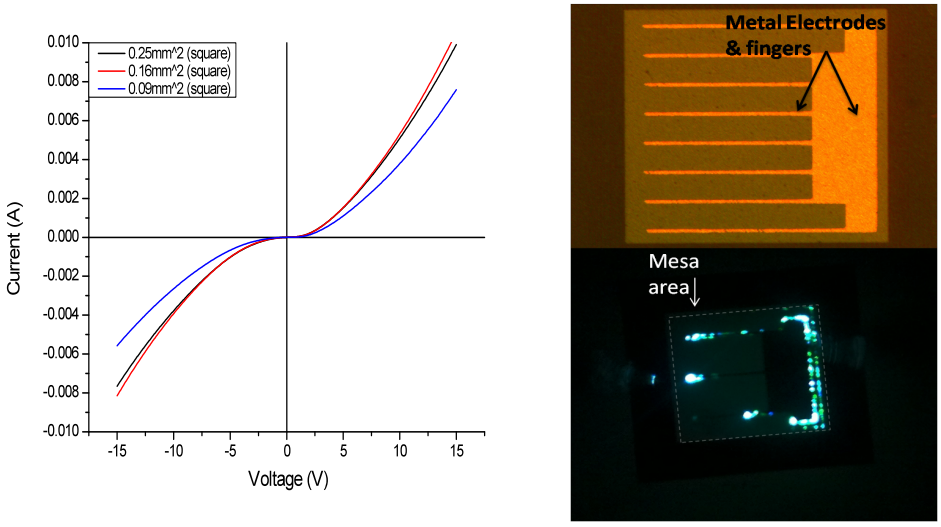

(a) (b,c)

Figure 12-4. (a) I-V data of 100nm UID InGaN/GaN solar cell, (b,c) processed and forward biased solar cell

The next structures used a re-growth technique. Photoluminescence (PL) measurements were performed on two of the grown samples (E811 without re-growth, E814 with re-growth) and Figure 12-5 shows the PL data obtained.

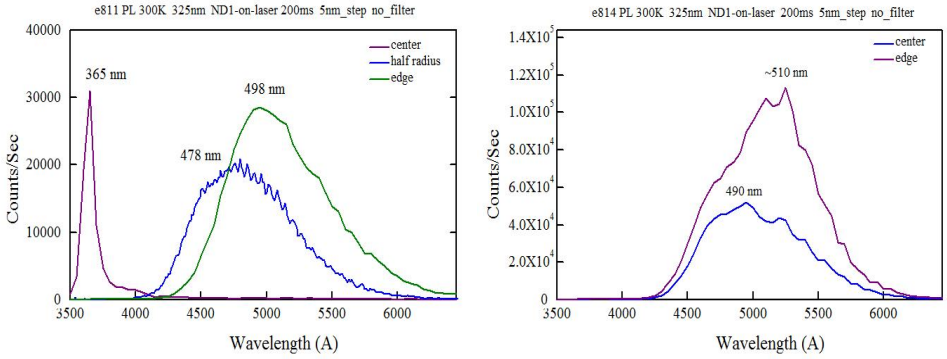

Figure 12-5. Photoluminescence measurement data for p-i-n InGaN/GaN solar cell (E811 ad E814)

There is a difference in the photoluminescence peak at the center and the edge of the samples, which indicates that indium composition varies throughout the samples.

Indium composition can be easily calculated from the PL peak and it varies from 22%~27%

The ARL has grown a p-GaN (1um) layer on sapphire and then we defined a "re-growth" area by using a SiO_2 mask technique. After we finished the re-growth patterning, the samples were returned to ARL for selective re-growth. UID-InGaN and n-InGaN have been grown on both samples. Samples were then returned to our facility for further processing. The re-growth technique was only applied to one (E814) of the two samples for comparison.

The E811 sample was dry etched using inductively coupled plasma-reactive ion etching for defining the mesa areas. E814 sample's mesa areas have already been defined by SiO_2 masking in the previous step and SiO_2 was removed by hydrofluoric acid. P-metal and n-metal contacts were deposited using electron beam evaporator. Fully processed InGaN/GaN solar cells are shown in Figure 12-6.

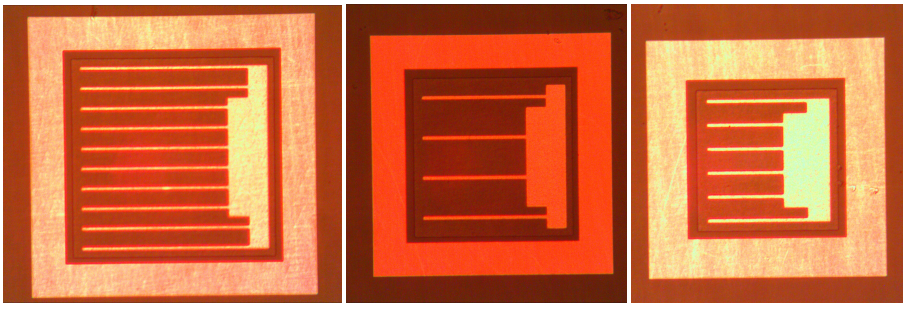

Figure 12-6 Processed InGaN/GaN solar cells (500x500um^2, 400x400um^2, and 300x300um^2)

Solar simulator and I-V testing have been performed on these samples. For the solar simulator measurement, we used 1.5 sun with AM1.5G filter. The solar simulator results are summarized in table 2.

	Voc (V)	Jsc (mA/cm^2)	FF (%)	Efficiency
400x400um^2, 10um width and 100um period fingers	0.191	0.525	31.01	0.021
400x400um^2, 10um width and 100um period fingers	0.188	0.514	30.78	0.020
500x500um^2, 10um width and 500um period fingers	0.201	0.419	31.96	0.019

Table 12-5 Solar simulator measurement results

Observed V_{oc} is lower than what others have reported due to the large saturation current. Also, the measured fill factor is lower since we have high series resistance R_s. In addition to solar simulator measurements we measured I-V characteristics and results are shown in Figure 12-7. Also, we still observed that the solar cell emitted green-blue light around the metal and mesa edges when a forward bias was applied to it.

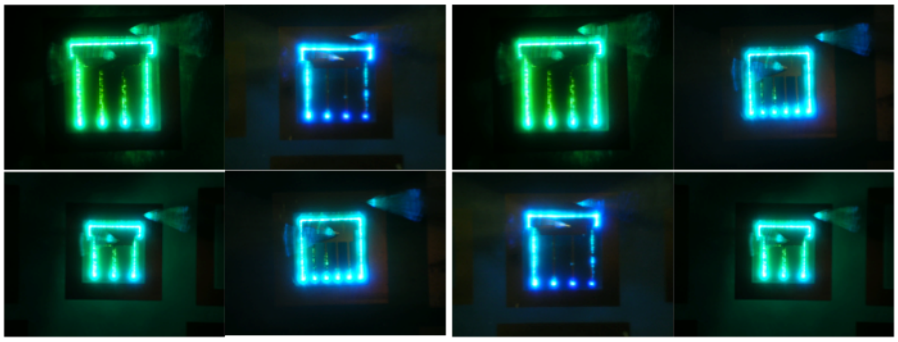

(a) (b)

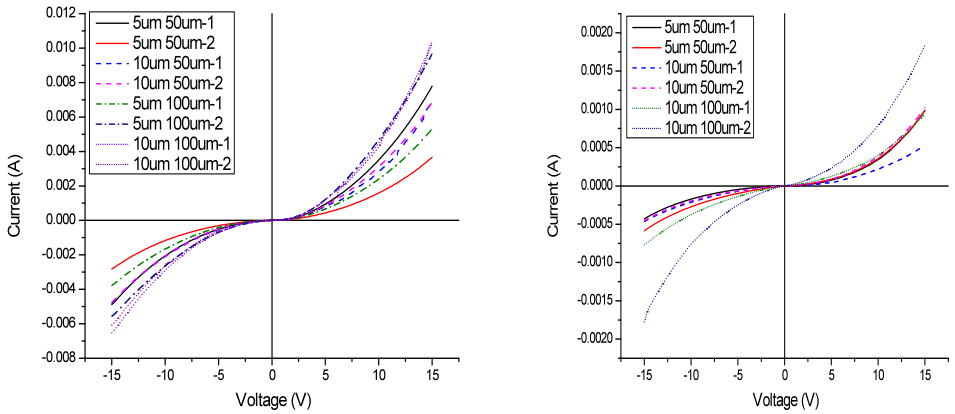

(c) (d)

Figure 12-7 (a) E811 forward biased, (b) E814 forward biased, (c) I-V characteristic of E811, and (d) I-V characteristic of E814

For a third structure, we tried a GaN/InGaN/GaN (1um/100nm/100nm) structure (E827) on 300nm AlN buffer/nucleation template on sapphire substrate to maximize absorption in the intrinsic region as well as to avoid defects in the InGaN top layer. We tested this structure using an UV LED to see the UV response. The LED gives 11.05mW power, peak wavelength at 374nm and FWHM is 26nm. Figure 12-8 shows the current and power density of 500X500um devices and Table 12-6 shows the device test results summary.

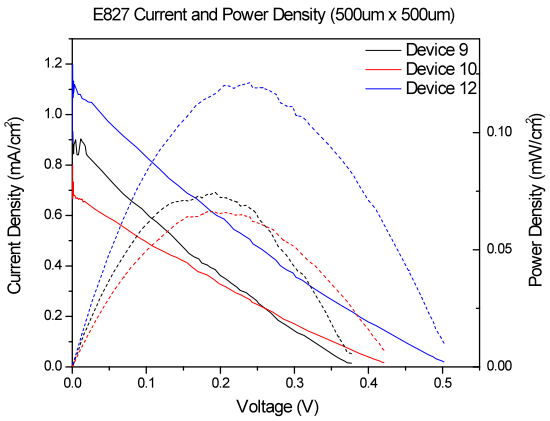

Figure 12-8 E827 (n-i-p) structure current and power density

	Series Resistance (Ω cm^2)	Shunt Resistance (Ω cm^2)	Open Circuit Voltage (V)	J_{sc} (mA/cm^2)	Fill Factor (%)	Quantum Efficiency (%)	Maximum Power (uW)	Responsivity (mA/mW)
Device 9	1.5e3	3.2e3	0.377	0.9	21.17	0.0017	0.186	2.11e-4
Device 10	1.2e3	1.9e3	0.421	0.7	19.69	0.0015	0.166	1.81e-4
Device 12	1.2e3	2.9e3	0.502	1.1	27.18	0.0027	0.303	2.71e-4

Table 12-6 E827 (n-i-p) structure test results summary

There might be two main reasons why we get low quantum efficiency with an UV light source. First, E827 PL shows peak emission at 361nm but the UV LED has peak emission at 374nm. As a result, photons might only be absorbed partially in GaN and InGaN, resulting in low quantum efficiency even with an UV light source. Secondly, electron hole pairs that are generated in InGaN might just recombine at the defect sites due to poor material quality. Also, we observed that the series resistance is too high and the shunt resistance is too low, indicating poor quality.

After testing many different structures, we have made a great number of discoveries. The most important improvement that we need to make is the material quality. Poor material quality can cause many critical problems including low shunt resistance, low extraction efficiency, etc. Also, we need to improve our fabrication processing by adding sidewall passivation. To understand the material quality, in the future measurements, we should measure the wavelength dependence of the quantum efficiency.

Chapter 13: Conclusion and Future work

13.1 Conclusion

The band gap of the InGaN material covers most of the visible region and it has been considered a perfect candidate for the next generation high efficiency solar cell. However, the InGaN material system faces many challenging issues such as no native substrate, difficulty of achieving high p-type doping of InGaN, large lattice mismatch, spontaneous polarization and the generation of large piezoelectric polarization in the presence of strain.

During my Ph.D study, I implemented a novel p-side down high efficiency InGaN/GaN solar cell. For conventional c-plane, Ga-face crystals, p-up devices suffer from a large piezo-electric polarization. Having grown the solar cell with the p-side down, it is possible to minimize the role that the piezo-electric polarization charges play to make a better solar cell. In addition, I used selective re-growth of the inverted structure. This will allow doing etch-free processing. Also, it might also help us to reduce the size of interdigitated fingers which should lead to increase efficiency since there will be less shadow loss and absorption due to the fingers. Having a high efficiency solar cell will reduce the use of crude oil and will help minimize the spread of pollution in the atmosphere.

13.2 Future work

During my Ph.D study, We have encountered several problems, such as processing of p-side down solar cell without any surface damage, achieving p-type ohmic contact, and improving the quality of material. We were able to solve most of the problems or are in the process of solving them. Even though we could not demonstrate a very high efficiency solar cell, now we know what we should do in the future. We believe that in order to achieve high quantum efficiency using III-Nitride material, most importantly we have to control dislocation density. To reduce threading dislocation density, we are planning to grow thick GaN template on sapphire. Also, we are planning to use freestanding GaN substrate to reduce the dislocation density as low as 10^6 cm^2. However, even with freestanding GaN substrate we have to control epitaxial film quality as well.

Recently, we started our collaboration with Naval Research Lab on III-Nitride project and they have patents on growing confined epitaxy on SiC substrate. With these techniques, we can also control the film quality.

Publications

Patent

P1: **Geunmin Ryu**, Athanasios Chryssis, Mario Dagenais, "High Spatial Resolution Incoherent optical Frequency Domain Reflectometry for health Monitoring of Fiber Optics Links", US Provisional Patent 61/100465, September, 2008

Peer-reviewed Publications

J1: Geunmin Ryu, Athanasios Chryssis, Jeyran Amirloo, Simarjeet Saini, Fred J. Towner and Mario Dagenais, "Gain and losses and Room temperature operation in Interband cascade lasers", *IEEE Photonics journal*, (accepted)

J2: Kwangsik Choi, Filiz Yesikov, **Geunmin Ryu,** SiHyung Cho, Mario Dagenais, Neil Goldsman, and Martin Peckerar, "Focused Asymmetric Metal-Insulator-Metal Tunneling Diode: DC Characteristics and RF Rectification Analysis", *IEEE Transaction on Electron Devices,* vol. 58, pp. 3519, 2011

J2: Kwangsik Choi, **Geunmin Ryu,** Filiz Yesilkoy, Athanasios Chryssis, Mario Dagenais, Neil Goldsman, and Martin Peckerar, "Geometry Enhanced Asymmetric Rectifying Tunneling Diodes", *Journal of Vacuum Science Technology B*, vol.28, pp.C6O50, 2010

J3: **Geunmin Ryu**, Mario Dagenais, Mattew T. Hurley, and Philip DeShong, "High Specificity Binding of Lectins to Carbohydrate-Functionalized Fiber Bragg Graings: A New Model for Biosensing Applications", *Journal of Selected Topics in Quantum Electronics*, a special issue on: Biophotonics, May/June, 2010

J4: Christopher J. Stanford, **Geunmin Ryu**, Mario Dagenais, Mattew T. Hurley, and Philip DeShong, "Covalent Attachment of Glucose to an Evanescent Wave Fiber Bragg Grating Bio-Sensor", *Journal of Sensors*, vol.2009, Article ID 982658, 7pages. 2009. doi:10.1155/2009/982658 **(invited)**

(Under review & Preparation for publications)

J6: **Geunmin Ryu** and Mario Dagenais, "Incoherent Optical Frequency Domain Reflectometry (IOFDR) for Faults Detection of Avionic Fiber Optics Networks ", *Photonics Technology Letter*, under preparation for journal publication

J7: **Geunmin Ryu**, Athanasios Chryssis, and Mario Dagenais, "Thermal impedance simulation and measurement of Epi-up and Epi-down mounted Interband cascade laser near room temperature", under preparation for journal publication

Refereed Conference Proceedings Articles

R1: **Geunmin Ryu**, Mario Dagenais, Matthew T. Hurley, and Philip DeShong, "High Specificity Biding of Lectins to Carbohydrate Functionalized Etched Fiber Bragg Grating Optical Biosensor", *IFMBE Proceedings 26th Southern Biomedical Engineering Conference*, College Park, MD, April 30– May 2, 2010

R2: Mario Dagenais, **Geunmin Ryu**, Simargeet Saini, F. Toudeh-fallah, R. Gyurek, and P. Donner, "Semiconductor Optical Amplifier Switch Matrices for Optical Header Recognition", Optoelectronic Integrated Circuits X, Edited by Eldada Louay A, Lee El-hang, Proceedings of the SPIE, vol. 6897, pp. 68970X-68970X-13, 2008 **(invited)**

Presentations in Conferences (Presenter underlined)

C1: Geunmin Ryu, Jeyran Amirloo, Simarjeet Saini, Fred J. Towner and Mario Dagenais, "High Power, Low Loss Room Temperature Operation in Interband Cascade Lasers", *CLEO 2012*, (submitted)

C2: Kwangsik Choi,Filiz Yesikoy, **Geunmin Ryu,** Mario Dagenais, and Martin Peckerar, "Zero-bias Rectifying performance Enhancement of MIM Tunneling Diodes by Geometric Field Enhancement and Boling Water Oxidation", The 55th International Conference on Electron, Ion, Photon Beam Technology and Nanofabrication, Las Vegas, Nevada, May 31– June 4, 2011

C3: Athanasios Chryssis, **Geunmin Ryu**, and Mario Dagenais,, "Thermal Impedance of Epi-Up and Epi-Down Interband Cascade Lasers", The 23rd Annual Meeting of the IEEE Photonics Society, Denver, Colorado, November 7-11, 2010

C4: Athanasios Chryssis, **Geunmin Ryu**, and Mario Dagenais,, "Measurement of internal quantum efficiency and temperature dependence of gain and loss in interband cascade lasers near room-temperature", 22nd IEEE International Semiconductor Laser Conference, Kyoto, Japan, September 26-30, 2010

C5: Kwangsik Choi, **Geunmin Ryu,** Filiz Yesilkoy, Athanasios Chryssis, Mario Dagenais, Neil Goldsman and Martin Peckerar, "Surface Plasmon and Geometry Enhanced Asymmetric Rectifying Tunneling Diodes", The 54th International Conference on Electron, Ion, Photon Beam Technology and Nanofabrication, Anchorage, Alaska, June 1-4, 2010

C6: **Geunmin Ryu**, Mario Dagenais, Matthew T. Hurley, Philip DeShong, "High Specificity Binding of Lectins to Carbohydrate Functionalized Etched Fiber Bragg Grating Optical Biosensor", The 26th Southern Biomedical Engineering Conference, College Park, April 30– May 2, 2010

C7: Simargeet Saini, **Geunmin Ryu**, and Mario Dagenais, "All Optical Header Recognition and Optical Packet Routing using Semiconductor Optical Amplifier Switch Matrices", Photonics 2008, International Conference on Fiber Optics and Photonics, New Delhi, India, December 13-17, 2008

C8: **Geunmin Ryu**, Mario Dagenais, "Incoherent Optical Frequency Domain Reflectometry for health Monitoring of Avionics Fiber Optics Networks", 2008 IEEE Avionics Fiber-Optics and Photonics Conference, San Diego, September 30– October 2, 2008

C9: Athanasios N. Chryssis, **Geunmin Ryu**, Mario Dagenais, "High Resolution Incoherent Optical Frequency Domain Reflectometry", Capital Science 2008, Arlington, VA, March 29-30, 2008

C10: Mario Dagenais, **Geunmin Ryu**, Simargeet Saini, F. Toudeh-fallah, R. Gyurek, and P. Donner, "Semiconductor Optical Amplifier Switch Matrices for Optical Header Recognition", SPIE Photonics West 2008, San Jose, CA, January 19-24, 2008 **(invited)**

Appendices

A) ICL Standard Processing Flow

- **Dielectric deposition for dry etching mask (This step only applies for the dry etching method)**
    - Si_3N_4 3000A by PECVD 30 mins
    - Password: mario, mario
    - Recipe (load SiN @ 200C)
    - Edit final steps (change time to 30min, ~5500A)
    - Push run
    - **Do not interrupt system wait until SiN process starts (Look if you can see purple plasma)**

- **Ridge patterning**
- Take out Photoresist (AZ5214E) from refrigerator to warm up to room temperature.
- Cleaning
    - Acetone 30s
    - Methanol 30s
    - IPA 30s
    - Blow dry with Nitrogen
- Put the samples into oven (110˚C ~120˚C) for 10 min to dry completely
- While the samples are in the oven do some preparation for next steps
    - Clean Mask, Chuck for spinner
    - Mix developer (AZ400K: DI water = 1:4 = 20ml : 80ml)
    - Mix wet etchant (Mix with tweezer) "**USE PROTECTIVE GROVE FOR HANDLING ACID"**
- **RIE Cleaning**
    - Pressure: 400, RF: 100, O2: 50 for 15sec
- Mount the sample on Glass slide
    - 1500rpm for 40s
    - Place the sample on the slide
    - Bake 90˚C~95˚C for 1min
- HMDS coating
    - Spin coat 3000rpm for 40s
- Spin coating AZ 5214E
    - 4000rpm for 40s
- Soft baking 90˚C~95˚C for 1min
- Photolithography
    - 365nm (Ch1) for 8s
- Develop (AZ400K: DI water = 1:4 = 20ml : 80ml)

    - Develop the sample (about 20s)
- Hard baking 120˚C~125˚C for 20min

- Ridge Etching

- Wet etching

- Ridge Etching (Phosphoric acid [H_3PO_4]: Hydrogen peroxide [H_2O_2]:H_20= 30ml : 30ml : 90ml) and 5g Tartaric Acid powder

    - Use the shallow glassware
    - RPM 230~250
    - Etching for 5min30s (trench should be about 3.2um deep)- **if possible check this with small sample each time since etch rate is very sensitive to temperature**
    - Rinse with DI water
    - Blow Dry
- Remove Photoresist
    - Immerse into acetone and IPA, then blow dry
    - Check under microscope

- Dry etching

- Si_3N_4 etching:
    - RIE (oxide recipe): 90s, ~6000A/min
    - ICP-RIE (Si_3N_4 recipe): 150s, ~2650A/min)
- ICL etching
    - GaSb recipe: ~5700/min
    - Pressure: 2.5mTorr, Strike pressure: 5mTorr, RF: 100W, ICP: 400W, Helium backing: 10Torr, Ar: 2.5sccm, and BCl_3: 12.5sccm
- ICL Wet etching (~15s) for smooth surface
- Si_3N_4 removal:
    - RIE (oxide recipe): 90s, ~6000A/min
    - ICP-RIE (Si_3N_4 recipe): 150s, ~2650A/min)

- Dielectric Deposition

- Si_3N_4 3000A by PECVD 20minutes
- Password: mario, mario
- Recipe (load SiN @ 200C)
- Edit final steps (change time to 20min, 160A/min deposition rate)
- Push run
- **Do not interrupt system wait until SiN process starts (Look if you can see purple plasma)**

- Dielectric Opening patterning (AZ5214 single coating)

- Take out Photoresist (AZ5214E) from refrigerator to warm up to room temperature.
- Some preparation for next steps
    - Clean Mask, Chuck for spinner
    - Mix developer (AZ400K: DI water = 1:4 = 20ml : 80ml)
- HMDS coating (For adhesion problem between Si_3N_4 and PR)
    - Spin coat 3000rpm for 40s
- Spin coating AZ 5214E
    - 4000rpm for 40s
- Soft baking 90˚C~95˚C for 1min
- Photolithography
    - 365nm (Ch1) for 8s
- Develop (AZ400K: DI water = 1:4 = 20ml : 80ml)
    - Develop the sample for 1min
- Hard baking 120˚C~125˚C for 1min

- Dielectric Opening patterning (AZ5214 double coating)

- Take out Photoresist (AZ5214E) from refrigerator to warm up to room temperature.
- Take out Photoresist (AZ5214E) from refrigerator to warm up to room temperature.
- Some preparation for next steps
    - Clean Mask, Chuck for spinner
    - Mix developer (AZ400K: DI water = 1:4 = 20ml : 80ml)
- HMDS coating (For adhesion problem between Si_3N_4 and PR)
    - Spin coat 3000rpm for 40s
- Spin coating AZ 5214E
    - 2500rpm for 40s
- Soft baking 90˚C~95˚C for 1min
- Spin coating AZ 5214E (second layer)
    - 2500rpm for 40s
- Soft baking 90˚C~95˚C for 2min
- Photolithography
    - 365nm (Ch1) for 20s
- Develop (AZ400K: DI water = 1:4 = 20ml : 80ml)
    - Develop the sample for 1min
- Hard baking 120˚C~125˚C for 2min

- Dielectric Opening patterning (SPR 220-7)

- Take out Photoresist (SPR 220-7) from refrigerator to warm up to room temperature.
- Preparation for next steps

    - Clean Mask, Chuck for spinner
    - Prepare developer (352)
- HMDS coating (For adhesion problem between Si_3N_4 and PR)
    - Spin coat 3000rpm for 40s
- Spin coating SPR220-7
    - Start from 0rpm and increase until 6000rpm for 60s
- **Proximity Soft baking**
    - **Placed the sticks from cotton swab on the top of the hot plate and place the sample on top of these 60sec 105˚C.**
- **Contact Soft baking**
    - **Place the sample on top of hotplate for 90sec 105˚C**
- Photolithography
    - 365nm (Ch1) for 17.5s
- **WAIT FOR AT LEAST 45min**
- Develop (352)
    - Develop the sample for 3min (Depends on dielectric width, for 2um & 5um opening 1min 30s should be enough)

- RIE Etching (Si_3N_4)

- RIE (oxide recipe): 90s, ~6000A/min
- ICP-RIE (Si_3N_4 recipe): 150s, ~2650A/min)
- Remove Photoresist
    - Immerse into acetone and IPA, then blow dry
    - Check under microscope

- First metal lift-off patterning (flexible mask, image reversal)

- HMDS coating (For adhesion problem between Si_3N_4 and PR)
    - Spin coat 3300rpm for 40s
- PR coating
    - Spin coat 4000rpm for 40s
- Soft baking 90˚C~95˚C for 1min
- Photolithography
    - 365nm, Ch1 for 8s
- Hard baking 120˚C for 1min
- Photolithography
    - Expose without mask for 15s
- Develop (AZ400K: DI water = 1:4 = 20ml : 80ml)
    - Develop sample (about 20s)
- Check under microscope

- First epi-side metal deposition

- Start with native oxide removal
  - HCl : H2O=1 : 10= 10ml:100ml for 30s
- E-beam Metal Deposition
  - Ag/**Ti/Pt/Au**(thickness can be varied)=500/**300/1000/1000A**
- Lift-off
  - Immerse samples into Acetone, IPA, then blow dry

- Electroplating connection

- **Deposit either Ti or Au to connect all of ridges for electroplating (1500A)**

- Second metal lift-off patterning (image reversal)

- Mount the sample on Glass slide
  - 1500rpm for 40s
  - Place the sample on the slide
  - Bake 90˚C~95˚C for 1min
- HMDS coating
  - Spin coat 3300rpm for 40s
- PR coating
  - Spin coat 4000rpm for 40s
- Soft baking 90˚C~95˚C for 1min
- Photolithography
  - 365nm, Ch1 for 8s
- Hard baking 120˚C for 1min
- Photolithography
  - Expose without mask for 15s
- Develop (AZ400K: DI water = 1:4 = 20ml : 80ml)
  - Develop sample (about 20s)
  - Check under microscope

- Electroplating

- **Heat up the solution for 60C for at least 30min**
- **Current goes through device (device is ground)**
- **Use 2.5mA for 13min depend on the sample size(3um deposited)**

- Third metal deposition

- **Deposit 1000A of Au on top of electroplated Au**
- Lift-off
  - Immerse samples into Acetone, IPA, then blow dry

- Thinning

- Mounting on Cleaned Micro-Slide

- Applying wax on center of slide then put slide on the hot plate (150˚C)

- Go to , set hot plate 150˚C
- Put the fixture on hot plate then apply wax on the fixture
- Put sample & micro-slide on the fixture
- Take the fixture from hot plate and cool it down
- Thinning using sand paper
- Measure thickness between slide and sample. It should be about 120um (100um sample and 20um wax)

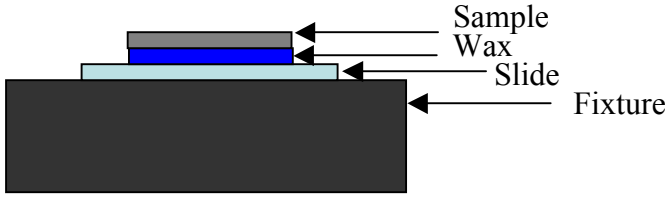

- After thinning, leave fixture on hot plate when wax melts, detach slide from fixture
- **FROM HERE YOU NEED TO BE EXTREMELY CAREFUL**
- Go to Kim Cleanroom
- Clean around sample with acetone to remove any dirty particles from thinning

- Backside Metal Deposition (See Metal Deposition Procedure)

- Ti/Pt/Au (Thickness can be varied)

- Cleaving

- Take sticky paper from drawer
- Attach sample (epi side up)
- Scratch where you want to cleave
- Cover with transparent vinyl from table top
- Put sample on blade and focus on blade
- Apply pressure with holding both sticky paper & vinyl
- Pick small sample using vacuum tweezer

B) Epi-up and down thermal simulation program (10um ridge)

Epi-up

```
title
 "10um ridge laser Epi-up Thermal simulation"

variables
      Temp(0.0)

definitions

parameters
      S=0.0                {set default Power Density}
      kx
     ky              {declare constants kx, ky - thermal conductivity in plane-parallel and
normal directions}
      CurrentDensity=1000/1       {set current density through device in Amps/Cm^2}
      Voltage=3            {set voltage across device in Volts}
      CavityLength = 1000.0   {set cavity length in microns}
      Tsink=25             {set arbitrary Cu heat sink temperature}
      structure=200.0              {set structure half-width}
      mesa=10.0            {set mesa full width in microns}
      thickIn=2 {from 0.3}           {set In layer thickness}
      thickAu=0.3           {set Au layer thickness}
      thickSiN=0.3          {set SiN thickness}
      thickAlN=1000.0           {set heat sink thickness}
      thickSub=80.0          {set substrate thickness}
            thickLClad1=2.5
      thickLClad2=1.5        {set lower clad thickness}
      thickActive=0.4422        {set active region thickness}
      thickUClad=1.4          {set upper clad thickness}
      thickscr=1
      lip=2        {set width of SiN on mesa top edge}
{derived parameters}

      thickEPAu=5
      L5=structure
      L2=mesa/2
      L3=L2+thickSiN
      L4=L3+3
      L1=L2-lip

      Volume= mesa*thickActive*CavityLength
```

```
      ActiveArea = mesa*CavityLength
      Current = ActiveArea*CurrentDensity*(1e-8)
      PowerDensity =Voltage*Current/Volume

      H1=thickAlN
      H2=thickAlN +thickIn
      H3=thickAlN +thickIn+thickSub
      H4=thickAlN +thickIn+thickSub+thickSiN +thickLClad1
      H5=thickAlN +thickIn+thickSub+thickLClad1+thickLClad2
      H6=thickAlN +thickIn+thickSub+thickLClad1+thickLClad2 +thickscr
      H7=thickAlN +thickIn+thickSub+thickLClad1+thickLClad2
+thickscr+thickActive
     H8=thickAlN +thickIn+thickSub+thickLClad1+thickLClad2
+thickscr+thickActive+thickscr
      H9=thickAlN +thickIn+thickSub+thickLClad1+thickLClad2
+thickscr+thickActive+thickscr+thickUClad
      H10=thickAlN +thickIn+thickSub+thickLClad1+thickLClad2
+thickscr+thickActive+thickscr+thickUClad+thickSiN
      H11= thickAlN +thickIn+thickSub+thickSiN+thickAu+thickEpAu +2.5
      H12= thickAlN +thickIn+thickSub+thickLClad1+thickLClad2
+thickscr+thickActive+thickscr+thickUClad+thickSiN+thickAu+thickEpAu

{Thermal Properties
All entries are in Watts/meter/Kelvin and results are multiplied by 1.0e-6 to change to
Watts/micron/Kelvin
}

      kAlN=285.0e-6
      kIndium=82.0e-6
      kGold=297.0e-6 {from 317}
      kSiN=2e-06 {kAl2O3=28-35 x e-06,    kSiO2=1.40e-06 }
      kGaSb=32.0e-6 {from 33}
      kxLClad=25e-6
      kyLClad=2e-6
      kxUClad=25e-6
      kyUClad=2e-6
      kActive=4e-6

equations

      dx(kx*dx(Temp)) + dy(ky*dy(Temp)) +S = 0

boundaries

      region 1      {Overall Boundary of SDL problem}
      kx=kAlN
```

```
        ky=kAlN
 start(0.0,0.0)
        value(Temp) = Tsink {set low edge of AlN to Tsink}
 line to (200,0.0)
natural(Temp)=0
 line to (L5,H11) to (L4,H11) to (L4,H12)
 to (0.0,H12) to finish

 region 2          {In bond region}
 kx=kIndium
 ky=kIndium
 start(0.0,H1)
 line to (L5,H1) to (L5,H2) to (0.0,H2) to finish

 region 3          {Substrate region}
 kx=kGaSb
 ky=kGaSb
 start(0.0,H2)
 line to (L5,H2) to (L5,H3)
 to (0.0,H3) to finish

 region 4          {Lower Cladding region}
 kx=kxLClad
 ky=kyLClad
 start(0.0,H3)
 line to (L5,H3) to (L5,H3+2.5)
 to (0.0,H3+2.5) to finish

region 5
kx=kxLClad
ky=kyLClad
start (0.0,H3+2.5)
line to (L2,H3+2.5) to (L2,H5)
to (0, H5) to finish

 region 4          {Lower Cladding region}
 kx=kxLClad
 ky=kyLClad
 start(0.0,H3)
 line to (L2,H3) to (L2,H5)
 to (0.0,H5) to finish


 region 6          {Lower SCR region}
 kx=kGaSb
 ky=kGaSb
```

```
    start(0.0,H5)
    line to (L2,H5) to (L2,H6)
    to (0.0,H6) to finish

    region 7          {Active region}
    kx=kActive
    ky=kActive
    S=PowerDensity
    start(0.0,H6)
    line to (L2,H6) to (L2,H7)
    to (0.0,H7) to finish

region 8          {Lower SCR region}
    kx=kGaSb
    ky=kGaSb
    start(0.0,H7)
    line to (L2,H7) to (L2,H8)
    to (0.0,H8) to finish


    region 9    {Upper Cladding region}
    kx=kxUClad
    ky=kyUClad
    start(0.0,H8)
    line to (L2,H8) to (L2,H9)
    to (0.0,H9) to finish

    region 10    {SiN region}
    kx=kSiN
    ky=kSiN
    start(L2,H3+2.5)
    line to (L5,H3+2.5) to (L5,H4)
    to (L3,H4) to (L3,H10)
    to (L1,H10) to (L1,H9)
    to (L2,H9) to finish

    region 11     {Au region}
    kx=kGold
    ky=kGold
    start(L3,H4)
    line to (L5,H4) to (L5,H11)
    to (L4,H11) to (L4,H12)
    to (0.0,H12) to (0.0,H9)
    to (L1,H9) to (L1,H10)
    to (L3,H10) to finish
```

```
monitors


plots

grid(x,y) report(globalmax(temp)) as 'MaxTemp' report ((globalmax(temp)-
Tsink)/(Current*Voltage)) as 'Rthermal'
      report(current)

contour(Temp)
contour(Temp) zoom(0.0,H3-20.0,3*(L4-thickEPAu),20.0+(H9-H3)+thickEpAu)
contour(Temp) zoom(0.0,H3,L4,(H9-H3)+3)
elevation(Temp) from (0.0,H4) to (0.0,H9)

vector((Kx*(-dx(Temp))),(Ky*(-dy(Temp)))) as "HEAT FLUX"
vector((4000*Kx*(-dx(Temp))),(4000*Ky*(-dy(Temp)))) as "HEAT FLUX" zoom
(0.0,H3-3,L4,(H9-H3)+6)

end
```

Epi-down

```
title
 "10um ridge laser Epi-down Thermal simulation"

variables
      Temp(0.0)

definitions

{parameters}
      S=0.0                 {set default Power Density}
      k                    {declare constants kx, ky - thermal conductivity in plane-parallel
and normal directions}
      CurrentDensity=1000/2        {set current density through device in Amps/Cm^2}
      Voltage=6             {set voltage across device in Volts}
      CavityLength = 2000    {set cavity length in microns}
      Tsink=25              {set arbitrary Cu heat sink temperature}
      structure=200.0               {set structure half-width}
      mesa=10.0             {set mesa full width in microns}
      thickIn=2            {set In layer thickness}
      thickAu=0.3           {set Au layer thickness}
```

```
    thickSiN=0.3          {set SiN thickness}
    thickAlN=1000.0           {set heat sink thickness}
    thickSub=80.0          {set substrate thickness}
    thickLClad1=1.5         {set lower clad thickness}
    thickLClad2=2.5         {set lower clad thickness}
    thickActive=0.8844       {set active region thickness}
    thickUClad=1.4          {set upper clad thickness}
    thickscr=0.2
        thickEPAu=5
    lip=2        {set width of SiN on mesa top edge}
{derived parameters}


                    L5=structure
                    L2=mesa/2
                    L3=L2-lip
                    L4=L2+thickSiN
                    L1=L4+3




    Volume= mesa*thickActive*CavityLength
    ActiveArea = mesa*CavityLength
    Current = ActiveArea*CurrentDensity*(1e-8)
    PowerDensity =Voltage*Current/Volume



H1=thickSub
H2=thickSub+thickLClad1+thickLClad2
H3=thickSub+thickLClad1+thickLClad2+thickscr
H4=thickSub+thickLClad1+thickLClad2+thickscr+thickActive
H5=thickSub+thickLClad1+thickLClad2+thickscr+thickActive+thickscr
H6=thickSub+thickLClad1+thickLClad2+thickscr+thickActive+thickscr+thickUClad
H7=thickSub+thickLClad1+thickLClad2+thickscr+thickActive+thickscr+thickUClad
+thickSiN
H8=thickSub+thickSiN+2.5
H9=thickSub+thickSiN+thickAu+thickEpAu+2.5
H10=thickSub+thickLClad1+thickLClad2+thickscr+thickActive+thickscr+thickUCla
d+thickAu+thickEpAu
H11=thickSub+thickLClad1+thickLClad2+thickscr+thickActive+thickscr+thickUCla
d+thickAu+thickEpAu+thickIn
```

```
H12=thickSub+thickLClad1+thickLClad2+thickscr+thickActive+thickscr+thickUCla
d+thickAu+thickEpAu+thickIn+thickAlN

{Thermal Properties
All entries are in Watts/meter/Kelvin and results are multiplied by 1.0e-6 to change to
Watts/micron/Kelvin
}

    kAlN=285.0e-6
    kIndium=82.0e-6
    kGold=297.0e-6
    kSiN=2e-06 {kAl2O3=28-35 x e-06,    kSiO2=1.40e-06 }
    kGaSb=32.0e-6
    kLClad=2e-6 {Changed from 3.6}
    kUClad=2e-6 {Changed from 3.6}
    kActive=4e-6 {changed from 4}


equations

    dx(k*dx(Temp)) + dy(k*dy(Temp)) +S = 0

boundaries

    region 1      {Overall Boundary of SDL problem}
    k=kAlN
    start(0.0,H12)
          value(Temp) = Tsink {set low edge of Cu to Tsink}
    line to (L5,H12)
    natural(Temp)=0
    line to (L5,H10) to (L1,H10) to (L1,H9)
    to (L5,H9) to (L5,0.0) to (0.0,0.0) finish

    region 2          {In bond region}
    k=kIndium
    start(0.0,H11)
    line to (L5,H11) to (L5,H10) to (0.0,H10) to finish

    region 3          {Substrate region}
    k=kGaSb
    start(0.0,0,0)
    line to (L5,0) to (L5,H1)
    to (0.0,H1) to finish

    region 4          {Lower Cladding region}
    k=kLClad
```

```
start(0.0,H1)
line to (L5,H1) to (L5,H1+2.5)
to (0.0,H1+2.5) to finish

region 5          {Lower Cladding region}
k=kLClad
start(0.0,H1+2.5)
line to (L2,H1+2.5) to (L2,H2)
to (0.0,H2) to finish


region 6          {Lower SCR region}
k=kGaSb
start(0.0,H2)
line to (L2,H2) to (L2,H3)
to (0.0,H3) to finish

region 7          {Active region}
k=kActive
S=PowerDensity
start(0.0,H3)
line to (L2,H3) to (L2,H4)
to (0.0,H4) to finish

region 8          {Lower SCR region}
k=kGaSb
start(0.0,H4)
line to (L2,H4) to (L2,H5)
to (0.0,H5) to finish


region 9    {Upper Cladding region}
k=kUClad
start(0.0,H5)
line to (L2,H5) to (L2,H6)
to (0.0,H6) to finish

region 10          {SiN region}
k=kSiN
start(L2,H1+2.5)
line to (L5,H1+2.5) to (L5,H8)
to (L4,H8) to (L4,H7)
to (L3,H7) to (L3,H6)
to (L2,H6) to finish

region 11     {Au region}
```

```
    k=kGold
    start(L4,H8)
    line to (L5,H8) to (L5,H9)
    to (L1,H9) to (L1,H10)
    to (0.0,H10) to (0.0,H6)
    to (L3,H6) to (L3,H7)
    to (L4,H7) to finish



monitors


plots

grid(x,y) report(globalmax(temp)) as 'MaxTemp' report ((globalmax(temp)-
Tsink)/(Current*Voltage)) as 'Rthermal'
    report(current) as "Current"

contour(Temp)
contour(Temp) zoom(0.0,H1,L4+1,(H7-H1+2))
contour(Temp) zoom(0.0,(H1-2),L1+2,H11-H1+10)
elevation(Temp) from (0.0,0.0) to (0.0,H12)

vector((K*(-dx(Temp))),(K*(-dy(Temp)))) as "HEAT FLUX"
vector((4000*K*(-dx(Temp))),(4000*K*(-dy(Temp)))) as "HEAT FLUX" zoom
(0.0,H1,L4+1,(H7-H1+2))
vector((4000*K*(-dx(Temp))),(4000*K*(-dy(Temp)))) as "HEAT FLUX" zoom
(0.0,(H1-2),L1+2,H11-H1+10)
end
```

C) Piezoeffect in III-Nitride heterostructures

Let us consider an arbitrary III-Nitride compound $Al_xIn_yGa_{1-x-y}N$ grown on the underlying layer with the in-plane lattice constant a_s and c_s as shown in Figure C-1.

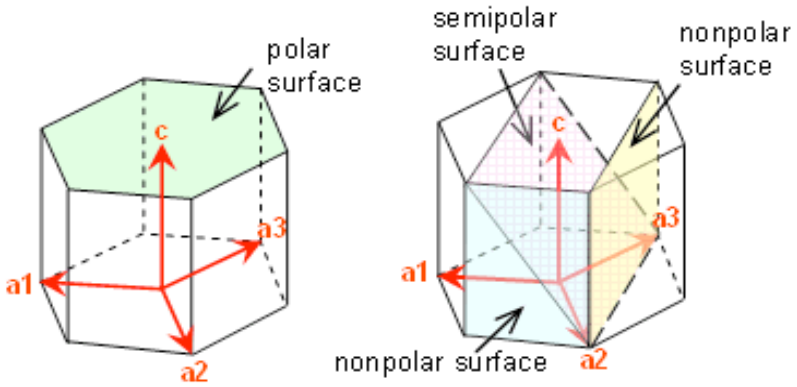

(a)

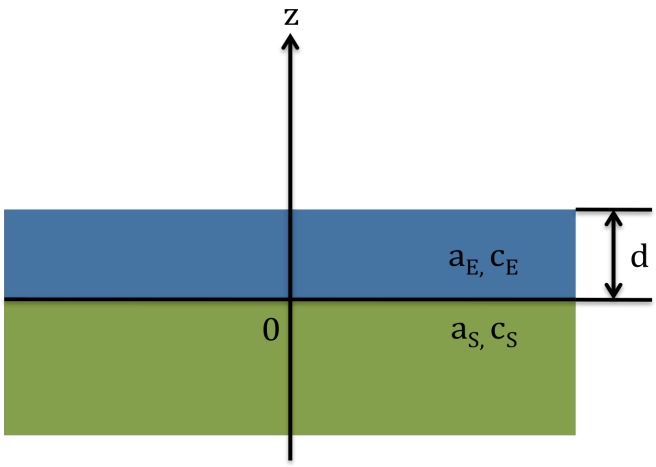

(b)

Figure C-1 (a) Wurzite structures, (b) Epitaxial layer on the underlying layer

The inclination angle Θ is the angle between the normal to the epitaxial layers and the hexagonal crystal axis. The in-plane lattice constants of the freestanding materal, a_E

and c_E would vary along the z-axis in accordance with the material composition and the Vegard law [71,82]

$$\begin{aligned} a_E &= a_{InN} \cdot y + a_{AlN} \cdot x + a_{GaN} \cdot (1 - x - y) \\ c_E &= c_{InN} \cdot y + c_{AlN} \cdot x + c_{GaN} \cdot (1 - x - y) \end{aligned} \tag{C-1}$$

However, the actual strained lattice constant need to consider the strain relaxation as well. If we take the strain relaxation into account, then the actual lattice constants become

$$\begin{aligned} a_R(z) &= (1 - \xi) \cdot a_S + \xi \cdot a_E(z) \\ c_R(z) &= (1 - \xi) \cdot c_S + \xi \cdot c_E(z) \end{aligned} \tag{C-2}$$

where ξ is the strain relaxation constant and it can be a number between 0 to 1.

The lattice mismatch along x and y axis can be defined as [71]

$$\begin{aligned} \eta_x &= [a_R - a_E]/a_E \\ \eta_y &= \frac{a_R c_R}{\sqrt{(a_E c_R \cos\theta)^2 + (a_R c_E \sin\theta)^2}} - 1 \end{aligned} \tag{C-3}$$

The strain tensor generally has 4 non-zero components

$$\begin{aligned} \varepsilon_{xx} &= \eta_x \\ \varepsilon_{yy} &= \eta_y \\ \varepsilon_{zz} &= \frac{(B_{41}\eta_x + B_{42}\eta_y)A_{32} - (B_{31}\eta_x + B_{32}\eta_y)A_{42}}{A_{31}A_{42} - A_{32}A_{41}} \\ \varepsilon_{yz} &= \frac{(B_{31}\eta_x + B_{32}\eta_y)A_{41} - (B_{41}\eta_x + B_{42}\eta_y)A_{31}}{A_{31}A_{42} - A_{32}A_{41}} \end{aligned} \tag{C-4}$$

where

$$
\begin{aligned}
A_{31} &= C_{11}\sin^4\theta + (C_{13}/2 + C_{44})\sin^2 2\theta + C_{33}\cos^4\theta \\
A_{32} &= (C_{11}\sin^2\theta + (C_{13} + 2C_{44})\cos 2\theta - C_{33}\cos^2\theta)\sin 2\theta \\
A_{41} &= \frac{1}{2}((C_{11} - C_{33})\sin^2\theta + 2C_{44}\cos 2\theta + (C_{13} - C_{33})\cos^2\theta)\sin 2\theta \\
A_{42} &= \left(\frac{C_{11} + C_{33}}{2} - C_{13}\right)\sin^2 2\theta + 2C_{44}\cos^2 2\theta \\
B_{31} &= C_{12}\sin^2\theta + C_{13}\cos^2\theta \\
B_{32} &= C_{13}(\sin^4\theta + \cos^4\theta) + \left(\frac{C_{11} + C_{33}}{4} - C_{44}\right)\sin^2 2\theta \\
B_{41} &= \frac{C_{12} - C_{13}}{2}\sin 2\theta \\
B_{42} &= \frac{1}{2}(C_{11}\cos^2\theta - (C_{13} + 2C_{44})\cos 2\theta - C_{33}\sin^2\theta)\sin 2\theta
\end{aligned}
\tag{C-5}
$$

where C_{ij} are the elastic stiffness tensor.

The total electric polarization in z component is

$$
\begin{aligned}
P_z^{tot} &= P^{spont}\cos\theta + \varepsilon_{xx}e_{31}\cos\theta + \varepsilon_{yy}(e_{31}\cos^3\theta + \frac{e_{33} - e_{15}}{2}\sin\theta\sin 2\theta) \\
&+\varepsilon_{zz}(e_{33}\cos^3\theta + \frac{e_{33} + e_{15}}{2}\sin\theta\sin 2\theta) + e_{yz}((e_{31} - e_{33})\cos\theta\sin 2\theta + e_{15}\sin\theta\cos 2\theta)
\end{aligned}
\tag{C-6}
$$

where P^{spont} is the spontaneous polarization and e_{ij} are the piezoelectric tensor.

Bibliography

[1] M.Grau, C. Lin, O. Dier, C. Lauer, and M. C. Amann, "Room-temperature operation of 3.26 μm GaSb-based type-I lasers with quinternary AlGaInAsSb barriers," *Appl. Phys. Lett.*, vol. 87, p. 241104, 2005.

[2] T. Lehnhardt, M. H¨ummer, K. Rossner, M. Muller, S. Hofling, and A. Forchel, "Continuous-wave single-mode operation of GaInAsSb/GaSb quantum well lasers emitting beyond 3 μm," *Appl. Phys. Lett.*, vol. 92, p. 183508, 2008.

[3] L. Shterengas, G. Belenky, T. Hosoda, G. Kipshidze, and S. Suchalkin, "Continuous-wave operation of diode lasers at 3.36 μm at 12 ◦C," *Appl. Phys. Lett.*, vol. 93, no. 1, p. 011103, 2008.

[4] T. Hosoda, G. Kipshidze, G. Tsvid, L. Shterengas, and G. Belenky, " Type-I GaSb-based laser diodes operating in 3.1 to 3.3 μm wavelength range," *IEEE Photon. Technol. Lett.*, vol. 22, no. 10, pp. 718–720, May 2010.

[5] T. Hosoda, G. Kipshidze, L. Shterengas, and G. Belenky, "Diode lasers emitting near 3.44 μm in continuous-wave regime at 300 K," *Electron. Lett.*, vol. 46, no. 21, pp. 1455–1456, 2010.

[6] Y. Bai, S. Slivken, S. R. Darvish, and M. Razeghi, "Room temperature continuouswave operation of quantum cascade laserswith 12.5%wallplug efficiency," *Appl. Phys. Lett.*, vol. 93, no. 2, p. 021103, 2008.

[7] A. Lyakh, R. Maulini, A. Tsekoun, R. Go, C. Pflugl, L. Diehl, Q. J.Wang, F. Capasso, and C. K. N. Patel, "3 W continuous-wave room temperature single-facet emission from quantum cascade lasers based on nonresonant extraction design approach," *Appl. Phys. Lett.*, vol. 95, no. 14, p. 141113, 2009.

[8] N. Bandyopadhyay, Y. Bai, B. Gokden, A. Myzaferi, S. Tsao, S. Slivken, and M. Razeghi, "Watt level performance of quantum cascade lasers in room temperature continuous wave operation at $\lambda \sim 3.76$ μm," *Appl. Phys. Lett.,* vol. 97, no. 13, p. 131117, 2010.

[9] A. Lyakh, R. Maulini, A. Tsekoun, R. Go, S. Von der Porten, C. Pflugl, L. Diehl, F. Capasso, and C. K. N. Patel, "High-performance continuous wave room temperature 4.0-μm quantum cascade lasers with single-facet optical emission exceeding 2 W," *Proc. Natl. Acad. Sci. U.S.A.*, vol. 107, no. 44, pp. 18799–18802, 2010.

[10] F. Capasso, "High-performance mid-infrared quantum cascade lasers," *Opt. Eng.*, vol. 49, no. 11, p. 111102, 2010.

[11] W. W. Bewley, J. A. Nolde, D. C. Larrabee, C. L. Canedy, C. S. Kim, M. Kim, I. Vurgaftman, and J. R. Meyer, “Interband cascade laser operating cw to 257 K at λ = 3.7 μm,” *Appl. Phys. Lett.,* vol. 89, no. 16, p. 161106, 2006.

[12] K. Mansour, Y. Qiu, C. J. Hill, A. Soibel, and R. Q. Yang, “Mid-infrared interband cascade lasers at thermoelectric cooler temperatures*,” Electron. Lett*., vol. 42, no. 18, pp. 1034–1036, 2006.

[13] M. Kim, C. L. Canedy, W. W. Bewley, C. S. Kim, J. R. Lindle, J. Abell, I. Vurgaftman, and J. R. Meyer, “Interband cascade laser emitting at λ = 3.75 μm in continuous wave above room temperature,” *Appl. Phys. Lett*., vol. 92, no. 19, p. 191110, 2008.

[14] C. L. Canedy, W. W. Bewley, J. R. Lindle, J. A. Nolde, D. C. Larrabee, C. S. Kim, M. Kim, I. Vurgaftman, and J. R. Meyer, “Interband cascade lasers with wavelengths spanning 2.9 μm to 5.2 μm,” *J. Electron. Mater*., vol. 37, no. 12, pp. 1780–1785, 2008.

[15] I. Vurgaftman, C. L. Canedy, C. S. Kim, M. Kim, W. W. Bewley, J. R. Lindle, J. Abell, and J.R.Meyer, “Mid-infrared interband cascade lasers operating at ambient temperatures,” *New J. Phys*., vol. 11, p. 125015, 2009.

[16] W. W. Bewley, C. L. Canedy, C. S. Kim, M. Kim, J. R. Lindle, J. Abell, I. Vurgaftman, and J. R. Meyer, “Ridge-width dependence of midinfrared interband cascade laser characteristics,” *Opt. Eng*. vol. 49, p. 111116, 2010

[17] E. R. Crosson, K. N. Ricci, B. A. Richman, F. C. Chilese, T. G. Owano, R. A. Provencal, M. W. Todd, J. Glasser, A. A. Kachanov, B. A. Paldus, T. G. Spence, and R. N. Zare, _Stable isotope ratios using cavity ring-down spectroscopy: Determination of 13c/12c for carbon dioxide in human breath,_ Analytical Chemistry, vol. 74, no. 9, pp. 2003-2007, 2002.

[18] D. Vogler and M. Sigrist, “Near-infrared laser based cavity ringdown spectroscopy for applications in petrochemical industry,” Appl. Phys. B , vol. 85, pp. 349-354, 2006.

[19] J. O. Clemmesen, F. S. Larsen, J. Kondrup, B. A. Hansen, and P. Ott, “Cerebral Herniation in Patients With Acute Liver Failure Is Correlated With Arterial Ammonia Concentration,” HEPATOLOGY Vol. 29, No. 3, 1999.

[20] J. G. Crowder, H. R. Hardaway, and C. T. Elliott, "Mid-infrared gas detection using optically immersed, room-temperature, semiconductor devices," *Measurement Science and Technology,* vol. 13, pp. 882-884, 2002.

[21] Frank Tittel, Alan Fried, "Mid-Infrared Laser Applications in Spectroscopy." *Solid-State Mid-Infrared Laser Sources* pp. 458-529, 2003

[22] M. W. Sigrist, R. Bartlome, D. Marinov, J. M. Rey, D. E. Vogler, and H. Wächter, "Trace gas monitoring with infrared laser-based detection schemes,"*Applied Physics B: Lasers and Optics,* vol. 90, pp. 289-300, 2008.

[23] R. F. Kazarinov and R. A. Suris, "Possibility of the amplification of electromagnetic waves in a semiconductor with a superlattice," *Soviet Physics Semiconductors*, vol. 5, no. 4, pp. 707–709, 1971.

[24] C. R. Pidgeon, C. M. Ciesla, and B. N. Murdin, "Suppression of nonradiative processes in semiconductor mid-infrarerd emitters and detectors," *Pro. Quant. Electron*., vol. 21, pp. 361_419, 1998.

[25] D. Hofstetter, M. Beck, T. Aellen, and J. Faist, "High-temperature operation of distributed feedback quantum-cascade lasers at 5.3um," *Appl. Phys. Lett*., vol. 78, pp. 396_398, 2001.

[26] M. Beck, D. Hofstetter, T. Aellen, J. Faist, U. Oesterle, M. Ilegems, E. Gini, and H. Melchior, " Continuous Wave Operation of a Mid-Infrared Semiconductor Laser at Room Temperatuer," *Science*, vol. 295, no. 5553, pp. 301-305, 2002

[27] D. Z. Garbuzov, H. Lee, V. Khalfin, R. Martinelli, J. C. Connoly, and G. L. Belenky, "2.3–2.7 um room temperature CW operation of In- GaAsSb/AlGaAsSb broad waveguide SCH-QW diode lasers," *IEEE Photon. Technol. Lett*., vol. 11, no. 7, pp. 794–796, Jul. 1999.

[28] S. Simanowski, N. Herres, C. Mermelstein, R. Kiefer, M. Walther, J. Wagner, and G. Weinmann, "Strain adjustment in (GaIn)(AsSb)/ (AlGa)(AsSb) QWs for 2.3–2.7 um laser structures," *J. Crystal Growth*, vol. 209, no. 1, pp. 15–20, Jan. 2000.

[29] Y. Rouillard, F. Genty, A. Perona, A. Vicet, D. A. Yarekha, G. Boissier, P. Grech, A. N. Baranov, and C. Alibert, "Edge and vertical surface emitting lasers around 2.0–2.5 um and their applications," *Phil. Trans. R. Soc. Lond. A*., vol. 359, no. 1780, pp. 581–597, Mar. 2001.

[30] J. G. Kim, L. Shterengas, R. U. Martinelli, G. L. Belenky, D. Z. Garbuzov, and W. K. Chan, "Room-temperature 2.5 um InGaAsSb/Al- GaAsSb diode lasers emitting 1Wcontinuous-wave," *Appl. Phys. Lett*., vol. 81, no. 17, pp. 3146–3148, Oct. 2002.

[31] M. Garcia, A. Salhi, A. Perona, Y. Rouillard, C. Sirtori, X. Marcadet, and C. Alibert, "Low threshold high-power room-temperature continuous- wave operation diode laser emitting at 2.26 um," *IEEE Photon. Technol. Lett*., vol. 16, no. 5, pp. 1253–1255, May 2004.

[32] L. Shterengas, G. L. Belenky, A. Gourevitch, D. Donetsky, J. G. Kim, R. U. Martinelli, and D.Westerfeld, "High-power 2.3um GaSb-based linear laser array,"

IEEE Photon. Tech. Lett., vol. 16, no. 10, pp. 2218–2220, Oct. 2004.

[33] L. Shterengas, G. Belenky, M. Kisin, and D. Donetsky, "High power 2.4 um heavily strained type-I quantum well GaSb-based diode lasers with more than 1Wof continuous wave output power and a maximum power-conversion efficiency

[34] T. Newell, X. Wu, A. L. Gray, S. Dorato, H. Lee, and L. F. Lester, "The effect of I increased valence band offset on the operation of 2 um GaInAsSb-AlGaAsSb lasers," *IEEE Photon. Technol. Lett*., vol. 11, no. 1, pp. 30–32, Jan. 1999.

[35] E. Yablonovitch and E. Kane, "Reduction of lasing threshold current density by the lowering of valence band effective mass," *IEEE J. Lightw. Technol*., vol. 4, no. 5, pp. 504–506, May 1986.

[36] K. Vizbaras and M. C. Amann, "3.6um GaSb-based type-I diode lasers with quinternary barriers, operation at room temperature," *Elec. Lett*., vol. 47, no. 17, Aug. 2011

[37] Mit open courseware. [Online]. Available: http://ocw.mit.edu/

[38] S. Tiwari and D. J. Frank, "Empirical fit to band discontinuities and barrier heights in iii-v alloy systems," *Appl. Phys. Lett.,* vol. 60, pp. 630_632, 1992.

[39] R. Q. Yang, J. D. Bruno, J. L. Bradshaw, J. T. Pham, and D. E. Wortman, "Interband cascade lasers: progress and challenges," *Physica E: Low-dimensional Systems and Nanostructures,* vol. 7, pp. 69-75, 2000.

[40] R. Q. Yang, J. L. Bradshaw, J. D. Bruno, J. T. Pham, and D. E. Wortman, "Mid infrared type-II interband cascade lasers," *Quantum Electronics, IEEE Journal of,* vol. 38, pp. 559-568, 2002.

[41] J. R. Meyer, I. Vurgaftman, R. Q. Yang, and L. R. Ram-Mohan, "Type-II and type-I interband cascade lasers," *Electronics Letters,* vol. 32, pp. 45-46, 1996.

[42] P.S Zory, quantum well lasers. New York: Academic Press, 1993

[43] L.A. Coldren and S.W. Corzine, Diode Lasers and Photonic Integrated Circuits. New York: John Wiley & Sons, 1995

[44] A. Chryssis, " Design and fabrication of high-performance interband cascade tunable external cavity lasers," Ph.D. dissertation, University of Maryland, 2010

[45] P.M. Smowton and P. Blood, "The differential efficiency of quantum-well lasers", IEEE J. Selected Topics in Quantum Electr. Vol. 3, pp. 491, 1997

[46] T. Borca-Tasciuc, D. Achimov, W.L. Liu, and G. Chen, H.-W. Ren, C.-H. Liu,

and S.S. Pei, Micros.Thermophys. Eng. 5, 225, 2001

[47] Y. Hu, “Multilayer dielectric coatings for optoelectic devices,” Ph.D. dissertation, University of Maryland, College Park, 2000

[48] F. K. Reinhart, I. Hayashi, and M. B. Panish, “Mode refecltivity and waveguide properties of double-heterostructure injection lasers,” *J. of Appl. Phys.,* vol. 42, pp. 4466, 1971

[49] W. Hellmich and P. P. Deimel, “Optical AR-coating for optical waveguide devices,” *J. Lightwave Tech.,* vol. 10, pp. 469, 1992

[50] R. Prakasam, S. Fox, B. P. Gopalan, S. Kareenahalli, P. J. S. Heim, and M. Dagenais, “Practical approache to design and fabrication of antireflection coatings for semiconductor optical amplifiers,” *IEEE Phot. Tech. Lett*., vol. 8, pp. 509, 1996

[51] W.W. Bewley, J.R. Lindle, C.L. Canedy, M. Kim, C.S. Kim, D.C. Larrabee, I. Vurgaftman, and J.R. Meyer, “Gain, loss, and internal efficiency in interband cascade laser emitting at λ=3.6~4.1um,” *J. Appl. Phys*. 103, 013114, 2008.

[52] C.L. Canedy, W.W. Bewley, J.R. Lindle, J.A. Nolde, D.C. Larrabee, C.S. Kim, M. Kim, I. Vurgaftman, and J.R. Meyer, “Interband cascade laser with wavelength spanning 2.9um to 5.2um,” *J. Electronic Materials*, 37, 1780, 2008.

[53] A. Soibel, K. Mansour, Y. Qiu, C.J. Hill, and R. Q. Yang, “Optical gain, loss, and transparency current in high performance mid-infrared interband cascade laser,” *J. Appl. Phys*. 101, 093104, 2007.

[54] A. Chandola, R. Pino, and P.S. Dutta, “Below bandgap optical absorption in tellurium-doped GaSb,” *Semiconductor Science and Technology*, 20, 886, 2005.

[55] J. L Bradshaw, N. P. Breznay, J. D. Bruno, J. M. Gomes, J. T. Pham, F. J. Towner, D.E. Wortman, R. L. Tober, C. J. Monroy, K. A. Olver, “Recent progress in the development of type II interband cascade lasers,” *Physica E*, 20, 479, 2004

[56] L. Xingsheng, M. H. Hu, N. Hong Ky, C. G. Caneau, M. H. Rasmussen, R. W. Davis, Jr., and Z. Chung-En, "Comparison between epi-down and epi-up bonded high-power single-mode 980-nm semiconductor lasers," *Advanced Packaging, IEEE Transactions on,* vol. 27, pp. 640-646, 2004.

[57] A. Tsekoun, R. Go, M. Pushkarsky, M. Razeghi, and C. K. N. Patel, "Improved Performance of Quantum Cascade Lasers through a Scalable, Manufacturable Epitaxial-Side-Down Mounting Process," *Proceedings of the National Academy of Sciences of the United States of America,* vol. 103, pp. 4831-4835, 2006.

[58] W. Pittroff, G. Erbert, G. Beister, F. Bugge, A. Klein, A. Knauer, J. Maege, P.

Ressel, J. Sebastian, R. Staske, and G. Traenkle, "Mounting of high power laser diodes on boron nitride heat sinks using an optimized Au/Sn metallurgy," *Advanced Packaging, IEEE Transactions on,* vol. 24, pp. 434-441, 2001.

[59] L. Xingsheng, S. Kechang, R. W. Davis, L. C. Hughes, M. H. Hu, and Z. Chung En, "A metallization scheme for junction-down bonding of high-power semiconductor lasers," *Advanced Packaging, IEEE Transactions on,* vol. 29, pp. 533-541, 2006.

[60] W. W. Bewley, C. L. Canedy, C. S. Kim, M. Kim, J. R. Lindle, J. Abell, I. Vurgaftman, J. R. Meyer, "High single-mode powers from interband cascade lasers", IEEE photonics society, 2010 23rd annual meeting, Denver, CO, 2010

[61] [Online] Available: http://www.usgs.gov

[62] [Online] Available: http://www.wikipedia.org

[63] Martin A. Green, Solar Cells: Operation Principles, Technology and System Application. New Jersey: Prentice-Hall, Inc, 1982

[64] M. Anani, C. Mathieu, M. Khadraoui, Z. Chama, S. Lebid, and Y. Amar, "High grade efficiency III-nitrides semiconductor solar cell," *Microelectronics Journal,* vol. 40, pp. 427-434, 2009.

[65] C. J. Neufeld, N. G. Toledo, S. C. Cruz, M. Iza, S. P. DenBaars, and U. K. Mishra,"High quantum efficiency InGaN/GaN solar cells with 2.95 eV band gap," *Applied Physics Letters,* vol. 93, pp. 143502-3, 2008.

[66] X. Chen, K. D. Matthews, D. Hao, W. J. Schaff, and L. F. Eastman, "Growth, fabrication, and characterization of InGaN solar cells," *physica status solidi (a),* vol. 205, pp. 1103-1105, 2008.

[67] O. Jani, I. Ferguson, C. Honsberg, and S. Kurtz, "Design and characterization of GaN/InGaN solar cells," *Applied Physics Letters,* vol. 91, pp. 132117-3, 2007.

[68] H. Neff, O. K. Semchinova, A. M. N. Lima, A. Filimonov, and G. Holzhueter, "Photovoltaic properties and technological aspects of In1-xGaxN/Si, Ge ($0<x<0.6$) heterojunction solar cells," *Solar Energy Materials and Solar Cells,* vol. 90, pp. 982-997, 2006.

[69] S.-H. Park and S.-L. Chuang, "Comparison of zinc-blende and wurtzite GaN semiconductors with spontaneous polarization and piezoelectric field effects," *Journal of Applied Physics,* vol. 87, pp. 353-364, 2000.

[70] F. Bernardini, V. Fiorentini, and D. Vanderbilt, "Spontaneous polarization and piezoelectric constants of III-V nitrides," *Physical Review B,* vol. 56, p.

R10024, 1997.

[71] A. E. Romanov, T. J. Baker, S. Nakamura, J. S. Speck, and E. J. U. Group, "Strain-induced polarization in wurtzite III-nitride semipolar layers," *Journal of Applied Physics,* vol. 100, pp. 023522-10, 2006.

[72] C. D.-J. Xue Jun-Jun , Liu Bin , Xie Zi-Li , Jiang Ruo-Lian , Zhang Rong and Zheng You-Dou "Au/Pt/InGaN/GaN Heterostructure Schottky Prototype Solar Cell " *Chinese Phys. Lett. ,* vol. 29, p. 098102, 2009.

[73] R. Singh, D. Doppalapudi, T. D. Moustakas, and L. T. Romano, "Phase separation in InGaN thick films and formation of InGaN/GaN double heterostructures in the entire alloy composition," *Applied Physics Letters,* vol. 70, pp. 1089-1091, 1997.

[74] H. Hartono, P. Chen, S. J. Chua, and E. A. Fitzgerald, "Growth of InN and its effect on InGaN epilayer by metalorganic chemical vapor deposition," *Thin Solid Films,* vol. 515, pp. 4408-4411, 2007.

[75] N. A. El-Masry, E. L. Piner, S. X. Liu, and S. M. Bedair, "Phase separation in InGaN grown by metalorganic chemical vapor deposition," *Applied Physics Letters,* vol. 72, pp. 40-42, 1998.

[76] K. Kumakura, T. Makimoto, N. Kobayashi, T. Hashizume, T. Fukui, and H. Hasegawa, "Minority carrier diffusion length in GaN: Dislocation density and doping concentration dependence," *Applied Physics Letters,* vol. 86, pp. 052105 3, 2005.

[77] A. Syrkin, V. Ivantsov, O. Kovalenkov, A. Usikov, V. Dmitriev, Z. Liliental Weber, M. L. Reed, E. D. Readinger, H. Shen, and M. Wraback, "First all-HVPE grown InGaN/InGaN MQW LED structures for 460-510 nm," *physica status solidi (c),* vol. 5, pp. 2244-2246, 2008.

[78] M. L. Reed, E. D. Readinger, H. Shen, M. Wraback, A. Syrkin, A. Usikov, O. V. Kovalenkov, and V. A. Dmitriev, "n-InGaN/p-GaN single heterostructure light emitting diode with p-side down," *Applied Physics Letters,* vol. 93, pp. 133505-3, 2008.

[79] M. L. Reed, E. D. Readinger, C. G. Moe, H. Shen, M. Wraback, A. Syrkin, A. Usikov, O. V. Kovalenkov, and V. A. Dmitriev, "Benefits of negative polarization charge in n-InGaN on p-GaN single heterostructure light emitting diode with p side down," *physica status solidi (c),* vol. 6, pp. 585-588, 2009.

[80] Z. H. Feng, B. Liu, F. P. Yuan, J. Y. Yin, D. Liang, X. B. Li, Z. Feng, K. W. Yang, and S. J. Cai, "Influence of Fe-doping on GaN grown on sapphire substrates by MOCVD," *Journal of Crystal Growth,* vol. 309, pp. 8-11, 2007.

[81] S. Heikman, S. Keller, S. P. DenBaars, and U. K. Mishra, "Growth of Fe doped semi-insulating GaN by metalorganic chemical vapor deposition," *Applied Physics Letters,* vol. 81, pp. 439-441, 2002.

[82] Simulator of Light Emitters based on Nitride Semiconductor (SiLENSe), Physics Summary, STR Group, 2008